Forschungszentrum Karlsruhe
in der Helmholtz-Gemeinschaft
Wissenschaftliche Berichte
FZKA 7160

Core Design Analysis of the Supercritical Water Fast Reactor

M. Mori

Institut für Kern- und Energietechnik
Programm Nukleare Sicherheitsforschung

Oktober 2005

Forschungszentrum Karlsruhe

in der Helmholtz-Gemeinschaft

Wissenschaftliche Berichte

FZKA 7160

Core Design Analysis
of the
Supercritical Water Fast Reactor

Magnus Mori

Institut für Kern- und Energietechnik
Programm Nukleare Sicherheitsforschung

Von der Fakultät für Maschinenbau der Universität Stuttgart
genehmigte Dissertation

Forschungszentrum Karlsruhe GmbH, Karlsruhe

2005

Impressum der Print-Ausgabe:

Als Manuskript gedruckt

Forschungszentrum Karlsruhe GmbH
Postfach 3640, 76021 Karlsruhe

Mitglied der Hermann von Helmholtz-Gemeinschaft
Deutscher Forschungszentren (HGF)

ISSN 0947-8620

urn:nbn:de:0005-071600

CORE DESIGN ANALYSIS
OF THE
SUPERCRITICAL WATER FAST REACTOR

Von der Fakultät für Maschinenbau der Universität Stuttgart

zur Erlangung der Würde eines

Doktor-Ingenieurs (Dr. -Ing.) genehmigte Abhandlung

Vorgelegt von

Magnus Mori

aus Legnago (VR), Italien

Hauptberichter:	Prof. G. Lohnert, Ph.D.
Mitberichter:	Prof. Dr. T. Schulenberg
Tag der mündlichen Prüfung	20. Januar 2005

Institut für Kernenergetik und Energiesysteme der Universität Stuttgart

2005

Abstract

Light Water Reactor technology is nowadays the most successful commercial application of fission reactors for the production of electricity. However, in the next years, nuclear industry will have to face new and demanding challenges. The need for sustainable and cheap sources of energy, the need for public acceptance, the need for even higher safety standards, the need to minimize waste production are only a few examples. It is for these very reasons that a few next generation nuclear reactor concepts were selected for extensive research and development. Super critical water cooled reactors are one of them.

The use of a supercritical coolant would in fact allow for higher thermal efficiencies and a more compact plant design. As a matter of fact, steam generators, or steam separators and driers would not be needed thus, significantly reducing construction costs. Moreover, because of the high heat capacity of supercritical water, comparatively less coolant would be needed to refrigerate the reactor. Consequently, a water-cooled reactor with a fast neutron spectrum could potentially be designed: the SuperCritical water Fast Reactor.

This system presents unique features combining well-known fast and light water reactor characteristics in one design (e.g. the tendency to a positive void reactivity coefficient together with Loss Of Coolant Accidents, as design basis). The core is in fact loaded with highly enriched Mixed OXide fuel (average plutonium content of ~23%), and presents a peculiar and significant geometrical and material heterogeneity (use of radial and axial blankets, solid moderator layers, several enrichment zones). The safety analysis of this very complex core layout, the development of suitable tools of investigation, and the optimization of the void reactivity effect through core design, is the main objective of this work.

Kernauslegung eines mit überkritischem Wasser gekühlten schnellen Reaktors

Zusammenfassung

Bei der Leichtwasserreaktortechnologie handelt es sich um die zur Zeit erfolgreichste kommerzielle Anwendung von Spaltreaktoren zur Erzeugung von Elektrizität. In den kommenden Jahren steht die Nuklearindustrie jedoch vor neuen großen Herausforderungen. Der Bedarf an nachhaltigen und preisgünstigen Energiequellen, die öffentliche Akzeptanz, immer höhere Sicherheitsstandards und die Minimierung der Abfallproduktion sind nur ein paar Beispiele. Vor diesem Hintergrund wurden ein paar Reaktorkonzepte der nächsten Generation ausgewählt und umfangreicher Forschung und Entwicklung unterzogen. Ein solches Konzept bezieht sich auf superkritische wassergekühlte Reaktoren.

Die Verwendung eines superkritischen Kühlmittels würde tatsächlich höhere thermische Wirkungsgrade und eine kompaktere Anlagenauslegung ermöglichen. Dampferzeuger bzw. Dampfseparatoren und –trockner wären nicht mehr erforderlich, wodurch die Baukosten beträchtlich reduziert würden. Darüber hinaus wäre aufgrund der hohen Wärmekapazität von superkritischem Wasser eine vergleichsweise geringe Kühlmittelmenge zur Kühlung des Reaktors erforderlich. Somit könnte auch ein wassergekühlter Reaktor mit einem schnellen Neutronenspektrum konzipiert werden: der Schnelle Superkritische Wasserreaktor.

Dieses System besitzt einzigartige Merkmale und vereint die bekannten Eigenschaften von schnellen Reaktoren und Leichtwasserreaktoren in sich (z. B. positiver Voidkoeffizient und Kühlmittelverluststörfälle als Auslegungsgrundlage). Der Kern besteht aus hoch angereichertem Mischoxidbrennstoff (durchschnittlicher Plutoniumgehalt ~ 23 %) und ist sowohl von der Geometrie als auch vom Material her sehr heterogen (radiale und axiale Blankets, Feststoffmoderatorschichten, mehrere Anreicherungszonen). Eine Sicherheitsanalyse dieser sehr komplexen Kernanordnung, die Entwicklung geeigneter Analysewerkzeuge sowie die Optimierung des Voidkoeffizienten mittels Kernauslegung sind Gegenstand der vorliegenden Arbeit.

Table of Contents

Nomenclature

symbol	description	dimension
A	Area	[m^2]
A	Mesh cell area in the i coordinate direction	[m^2]
B	Mesh cell area in the j coordinate direction	[m^2]
χ	Fission spectrum fraction	-
$\chi(r,z)$	Linear power distribution	[J m^{-1} s^{-1}]
c_p	Specific heat, constant pressure	[J kg^{-1} K^{-1}]
d	Diameter	[m]
d	Trajectory track length	[m]
δ	Gap clearance	[m]
D_e	Hydraulic or wetted diameter	[m]
ε	Surface emissivity	[J m^{-2} K^{-4} s^{-1}]
ε	Error	
E	Energy	[J, eV]
f	Moody friction factor	-
f	Atomic fraction	-
ϕ	Dissipation function	[N m^{-2} s^{-1}]
ϕ	Energy and direction integrated neutron flux	[m^{-2} s^{-1}]
G	Mass flux	[kg m^{-2}s^{-1}]
h	Enthalpy	[J kg^{-1}]
h_{HT}	Wall heat-transfer coefficient	[J m^{-2} K^{-1} s^{-1}]
$\vec{i}, \vec{j}, \vec{k}$	Direction vectors	-
J	Neutron current density	[m^{-2} s^{-1} sr^{-1} eV^{-1}]
k	Thermal conductivity	[J m^{-1} K^{-1} s^{-1}]
k	Neutron multiplication constant	-
L	Channel length	[m]
μ	Dynamic viscosity	[kg m^{-1} s^{-1}]
μ	Mean value	
μ, η, ξ	Direction cosines	-

symbol	description	dimension
m	Mass	[kg]
$\dot{m}$	Mass flow rate	[kg s^{-1}]
N	Nominal source size	-
μ_0	Average scattering cosine	-
v	Specific volume	[m^{3} kg^{-1}]
N	Atomic number density	[atoms kg^{-3}]
p	Pressure	[Pa]
$p(x)$	Probability distribution	-
$\vec{q}'', q''$	Heat flux, surface heat flux	[J m^{-2} s^{-1}]
q'''	Volumetric heat generation rate	[J m^{-3} s^{-1}]
ρ	Density	[kg m^{-3}]
ρ	Reactivity	[pcm], [\$]
r	Radius	[m]
Σ	Macroscopic cross section	[m^{-1}]
σ	Standard deviation	-
σ	Microscopic cross section	[barn = 10^{-28} m^{2}]
S, Q	Differential neutron source density	[m^{-3} s^{-1} sr^{-1} eV^{-1}]
t	Time	[s]
T	Temperature	[K]
u	Internal energy	[J kg^{-1}]
υ	Number of neutrons isotropically emitted for each neutron absorbed in a fission reaction for a given energy	-
$\vec{v}$	Velocity	[m s^{-1}]
V	Mesh cell volume	[m^{3}]
w	Weight function	-
$\vec{\Omega}$	Angular direction	[sr]
x,y,z	Spatial position	[m]
Ψ	Neutron flux distribution in the phase space	[m^{-2} s^{-1} sr^{-1} eV^{-1}]
ψ	Energy integrated neutron flux	[m^{-2} s^{-1} sr^{-1}]
Z	Compressibility factor	-

Subscripts and Superscripts

symbol	description
a	Absorption, atomic
ave	Average
b	Bulk
c	Critical, clad, capture, collision
eff	Effective
f	Fuel
g	Gap, energy group index
i	Inner
im	Implicit
I,j,k	Coordinate directions
k	Nuclide index
m	Mean, multiplicity
nc	Nominal conditions
o	Outer
r	Relative
s	Scattering
sat	Saturation
tl	Track length
v	Cavity, void
$void$	Voided conditions
w	Wall

Dimensionless numbers

symbol	description	dimension
Nu	Nusselt number $\equiv hD_e/k$	-
P_r	Reduced pressure $\equiv P/P_c$	-
Pr	Prandtl number $\equiv C_p\mu/k$	-
Re	Reynolds number $\equiv GD_e/\mu$	-
T_r	Reduced temperature $\equiv T/T_c$	-
v_r	Reduced specific volume $\equiv v/v_c$	-

Acronyms

ADS	Automatic Depressurization System
	Accelerator Driven System
AHM	Advanced Heterogeneous Model
B&W	Babcock & Wilcox
BG	Breeding Gain
BOC	Beginning Of Cycle
BOP	Balance Of Plant
BWR	Boiling Water Reactor
CANDU	CANadian Deuterium-natural Uranium reactor
CFD	Core Damage Frequency
CHF	Critical Heat Flux
CPU	Central Processing Unit
CR	Conversion Ratio
CRDS	Control Rod Drive System
ECCS	Emergency Core Cooling System
EFF	European Fusion File
ENDF	Evaluated Nuclear Data File
EOC	End Of Cycle
EOS	Equation Of State
FPSR	Fissile Plutonium Surviving Ratio
FZK	Forschungszentrum Karlsruhe
GE	General Electric
HPCI	High Pressure Coolant Injection
JAERI	Japanese Atomic Energy Research Institute
JAPC	Japan Atomic Power Company

JEF	Joint Evaluated File
JEFF	Joint Evaluated Fission and Fusion general purpose File
JENDL	Japanese Evaluated Nuclear Data Library
JNDC	Japanese Nuclear Data Committee
LMFBR	Liquid Metal Fast Breeder Reactor
LMFR	Liquid Metal Fast Reactor
LOCA	Loss Of Coolant Accident
LOSP	Loss of OffSite Power
LPCI	Low Pressure Coolant Injection
LWR	Light Water Reactor
MA	Minor Actinide
MB	Mega Byte
MCNP	Monte-Carlo N Particle code
MINX	Multigroup Interpretation of Nuclear X-sections
MOX	Mixed OXide
MSL	Main SteamLine
MXN	Magnus Xue-Nong
NEA	Nuclear Energy Agency
NJOY	Nuclear Data Processing System (see MINX)
NNDC	National Nuclear Data Center
NPP	Nuclear Power Plant
PWR	Pressurized Water Reactor
PZR	PressuriZeR
RHR	Residual Heat Removal
ROSP	Recovery of OffSite Power
RPS	Reactor Protection System

RPV	Reactor Pressure Vessel
RSICC	Radiation Safety Information Computational Center
SCFR	SuperCritical water Fast Reactor
SCWFR	SuperCritical Water Fast Reactor
SCWR	SuperCritical Water Reactor
SFFP	Supercritical Fossil-Fired Plant
SG	Steam Generators
SI	Standard International
SIMMER	S_n Implicit Multifield Multicomponent Eulerian Recriticality code system

INTRODUCTION

More than 400 nuclear power plants currently operate throughout the world, supplying about 16% of the world's electricity. It is well known that unlike fossil fuel plants, nuclear plants do not release carbon dioxide, sulfur, or nitrogen oxides into the environment. The world's increasing demand for energy, and the growing concerns for the environment, will favor energy sources with minimal environmental impact and competitive economics. Nuclear power plants can and should play a role in the development of energy supply in the future and need to meet the new goals and challenges, which the electricity energy market poses. The goals, as stated in the Generation IV Roadmap [Lake (2002) /1/], are defined in the broad areas of sustainability, safety and reliability, economics, and proliferation resistance and physical protection. Sustainability goals focus on fuel utilization and waste management. Safety and reliability goals focus on safe and reliable operation and investment protection, essentially eliminating the need for emergency response, therefore improving public acceptance. Economic goals focus on competitive life cycle and energy production costs and financial risk. Proliferation resistance and physical protection focus on safeguarding nuclear material and nuclear facilities.

In this context six reactor concepts were selected by the Generation IV International Forum, among them supercritical water-cooled reactors. A supercritical behavior for a fluid exists when temperatures and pressures reach or exceed the critical point of that substance (~22 MPa and 647 K for water). Above the critical point, neither liquid or gas phases exist; instead, a poorly defined phase occurs, known as a supercritical fluid. This implies that high enthalpy coolant can be generated improving the thermal performance of the reactor [Oka (1998) /2/]. Supercritical fluids have the gas-like characteristic of low viscosity, and the liquid-like characteristic of high density; furthermore, since they do not exhibit a change of phase, when used as coolants, they can reach higher temperatures without incurring into a boiling crisis.

1.1 Motivation

Supercritical water-cooled reactors are therefore being developed to improve water reactor technology through simplification, improvement of thermal efficiency, and reduction of capital costs (see e.g. the work of Oka /3/). There are various design proposals (see for example the general review by Oka /4/), which differ according to the neutron spectrum: fast or thermal (a design of the fast option was suggested by Jevremovic (1995) /5/, while a reference design for the thermal option can be Oka (2000) /6/).

Another design variant is the coolant path, which can be ascending through the core in a single tube, or follow ascending and descending flow directions in a double tube to improve neutron moderation (see the conceptual design studied by Dobashi (1998) /7/ and Oka (2001) /8/).

Other design alternatives vary depending on the different steam cycles, which can be direct once through [Oka (1995) /9/], or indirect [Jevremovic (1993) /10/]. Further configuration variants depend on the actual plant layout, adapting either the current CANDU design (see for instance Duffey (2003) /11/), or the current LWR design (see Kang (2003) /12/). Nonetheless, all these designs present similar features, the most important and innovative one is the use of supercritical water at circa 25 MPa.

Today, the thermal neutron spectrum variant is being investigated intensively and developments are being made by collaborations between Japan and Europe within the 5th Framework Program of the European Commission [Heusener (2000) /13/] and also with institutions in the United States in the context of the Generation-IV

Program. This concept, however, has for the most part been pursued and developed by the Nuclear Engineering Research Laboratory of the University of Tokyo since the early 1990s, and has mainly focused on the supercritical-water cooled fast reactor variant.

The fast neutron spectrum variant might have a few advantages compared to the thermal option, not only from the design point of view, but also because of the flexibility and the sustainability of the fuel cycle. This reactor can in fact potentially breed at least as much fissile fuel as it depletes, providing energy for thousands of years.

This reactor therefore, was a logical extension of the worldwide efforts, which have thrived in the development of the steam-cooled breeder reactors. Although most of the countries involved in fast reactor development decided on the liquid metal cooled fast spectrum design, the supercritical water-cooled fast reactor is still an attractive variant of fast reactor systems [Oka (2000) /14/]. Among the several reactor configurations mentioned, this thesis focuses on the concept denominated SCFR (SuperCritical water Fast Reactor), the characteristics of which were defined in a contractual agreement between Japan Atomic Power Company and the Forschungszentrum Karlsruhe. Some of the original specific features of this reactor can be appreciated examining Figure 1.1, which gives an overview of the SCFR containment: a once-through direct cycle reactor, where all feed water flows through the core to the turbine at supercritical pressure (25 MPa).

The Reactor Pressure Vessel and the reactor vaults resemble the layout of a Pressurized Water Reactor, as can be better appreciated in Figure 1.2. The containment and the safety systems are similar to the ones of a Boiling Water Reactor, while the overall Balance Of Plant is comparable to Supercritical Fossil-Fired Plants.

With respect to a PWR the main differences are the absence of Steam Generators and of the pressurizer, while, with respect to a BWR, the main differences are the absence of steam separators and driers, the absence of coolant recirculation loops and associated pumps, control systems etc., and the Control Rod Drive System located above the RPV, instead of below.

These features imply several advantages in comparison with current Light Water Reactor plant layouts, essentially related with the compactness of the reactor building and components, which signifies not only a shorter construction time, and therefore a shorter ‘immobility’ of the invested capital, but also less costs for construction materials.

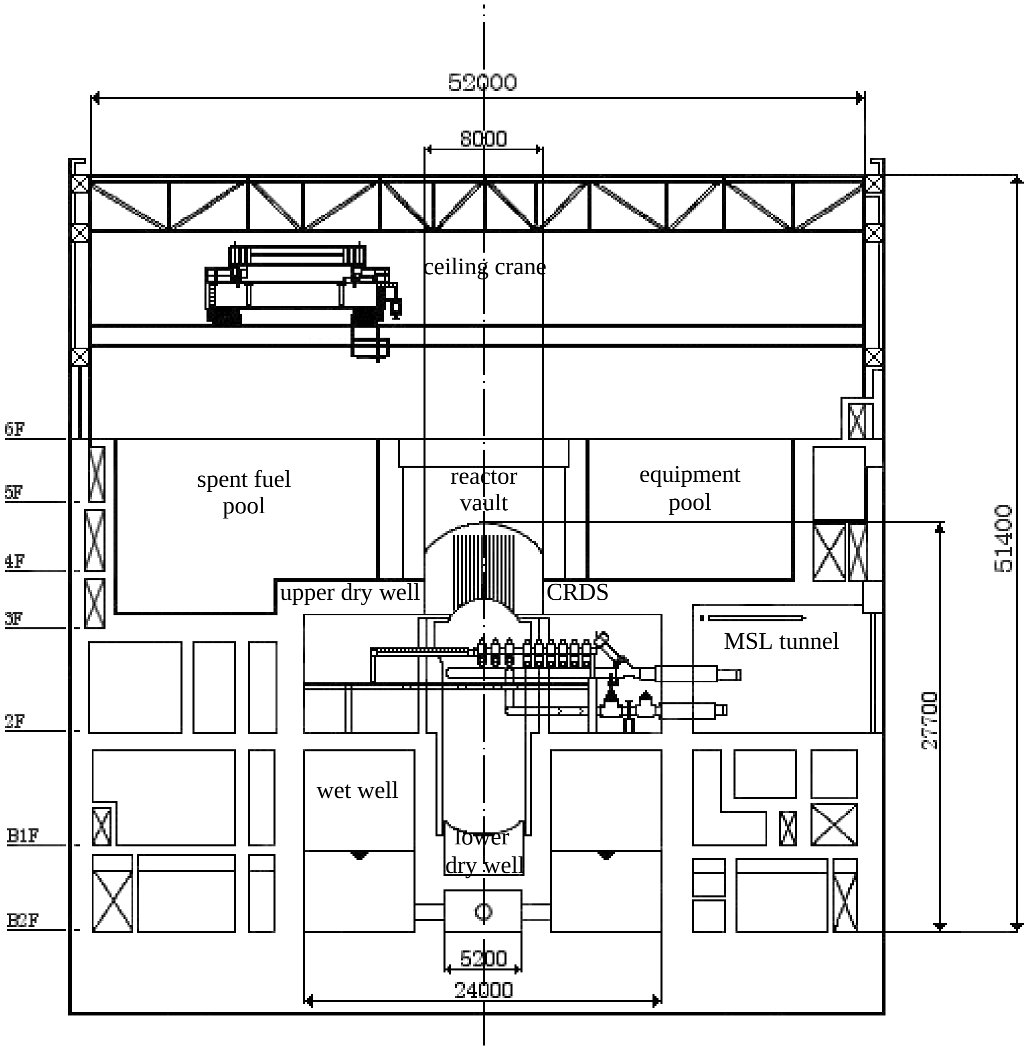

Figure 1.1: Overview of the SCFR primary systems.

The SCFR can then be considered a valid and promising future generation Nuclear Power Plant, which combines the advanced SFFP technology and the state of the art LWR technology with the desirable feature of an epithermal/fast neutron spectrum, since a higher η would allow the employment of this reactor as a transmuter.

Moreover, given the present situation of nuclear related research activities in Germany, and to some extent in the rest of Europe, the potential of the SCFR as a Minor Actinide burner makes it an appealing concept also by virtue of the inherent overall attention to the fuel cycle and treatment of the waste [Gabaraev (2003) /15/]. The presence of radial and axial blankets in fact, would easily allow the location of MA targets in areas of the core with an ideal neutron spectrum distribution and an efficient recycling of plutonium.

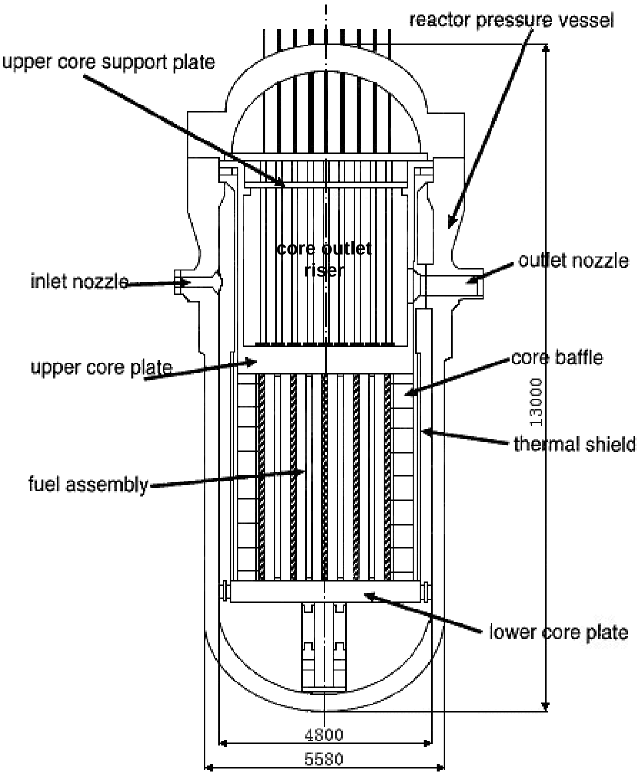

Figure 1.2: RPV of the SCFR.

Actinides are the elements that follow actinium in the periodic chart i.e. the elements with atomic numbers 90 through 103 (Z=90-103). In a nuclear reactor the minor actinides of interest, which result from nuclear reactions in the fuel, include e.g.: neptunium, americium, and curium. These elements have a high and long lived radiotoxicity and represent therefore a concern for the public; curium in particular poses specific hazards in the chemical preparation of spent nuclear fuel for transmutation, because of its high neutron emissivity [Culbreth (2002) /16/]. As a matter of fact, one of the specific advantages of the SCFR is the potential to avoid the build up of curium in the fuel inventory, which is a typical drawback of burning MAs in LWRs (see for instance the work of Vasile (2000) /17/, and Gerasimov (2003) /18/ on the transmutation potential in critical reactors). In order to achieve this level of reactor performance a conversion ratio larger than 1 is desirable if not required [Ishiwatari (2001) /19/], since it could eventually allow the introduction of dedicated targets [Iwasaki (2001) /20/] that could efficiently exploit this distinctive feature of the SCFR; namely, the fast spectrum and the well thermalized spectrum regions existing in the seed/blanket parts of the core, hence attaining the potential for an optimal conversion of MAs[1].

The achievement of a fast spectrum in a water reactor, which seems a contradiction in terms at first sight, since water is a very good moderator and would therefore slow down the neutrons, is possible because of the characteristics of supercritical water.

---

[1] In order to efficiently transmute Minor Actinides two opposing ideal conditions should be met: a high neutron flux, typical of fast reactors, and a thermal neutron spectrum to exploit the relative high absorption cross section of these elements in the thermal energy range. In the SCFR, moderated MA targets can therefore be designed to optimize the capture and fission yield in different areas of the reactor, according to the local fast, or thermal neutron spectra.

The idea of using a supercritical fluid for reactor cooling is actually more than 40 years old. General Electric [Aase (1963) /21/], Westinghouse [Keyfitz (1964) /22/] and Babcock & Wilcox performed the first studies in the United States during the 1950s and the 1960s, but they stopped at a preliminary stage giving way to PWRs, until, as mentioned, it was revived in Japan in the early 1990s. Nowadays, supercritical water technology is well developed and there are several SFFPs, especially coal fired, that use this type of coolant, operating worldwide [DOE (1999) /23/]. All these plants have a higher thermal efficiency (>43%) than the common water-cooled ones, the reason for this can be better understood when examining the properties of supercritical water.

1.2 Present State of the Technology

The values of the critical parameters for water are [Wagner (1998) /24/]:

$$T_c = 647.096 \text{ K},$$

$$p_c = 22.064 \text{ MPa},$$

$$\rho_c = 322 \text{ kg m}^{-3}$$

As mentioned, water at a supercritical pressure does not exhibit a change of phase when raising its temperature, however it is possible to define a pseudo-liquid/pseudo-vapor transition: that is a point in the phase diagram where the properties of the fluid change significantly, as in a change of phase. Figure 1.3 shows the pressure-enthalpy diagram for water and illustrates well how at the critical point the transition between the pseudo phases implicates a “sudden” change in the properties of the fluid, such as enthalpy and pressure; but other good examples would be density and heat capacity. Examining more closely the density behavior around the critical point, for instance, one would find that at 22.1 MPa increasing temperature from 637 K to 657 K (~+3%) causes a density change from 546 kg m^{-3} to 151 kg m^{-3} (~–72%) and an enthalpy change from 1759 kJ kg^{-1} to 2562 kJ kg^{-1} (~+31%).

Another characteristic of supercritical fluids is that the higher the pressure the milder the transition from the compressed “liquid” to the supercritical “gas” phase. The SCFR has an operating pressure of 25 MPa, therefore ~3 MPa above the critical pressure. The coolant inlet temperature is of ~553 K and at the outlet of ~796 K, achieving a cycle efficiency of 44.3%.

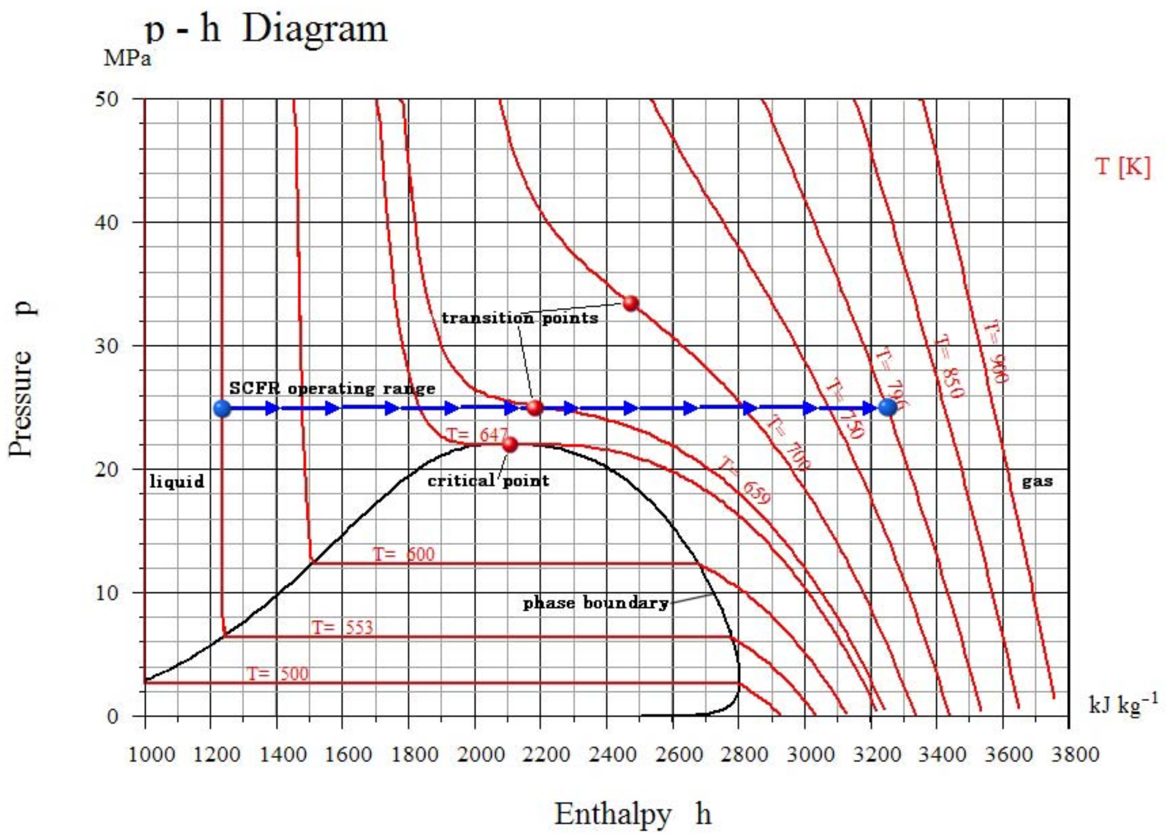

Figure 1.3: Pressure-enthalpy diagram for water

The transition temperature at 25 MPa is ~659 K and the inlet/outlet density ratio is ~9. These operating conditions imply that the properties of water change significantly within the working range of the reactor and differ even more from the known subcritical water characteristics. Hence, there exists currently a strong need to develop, or verify, the existing formulations for the Equations Of State, Heat Transfer Coefficients, pressure drop, and Critical Heat Flux correlations (see for instance the experimental work by Kurganov (1993) /25/, or the work on heat transfer deterioration at supercritical pressure by Shiralkar (1969) /26/ and Koshizuka (1995) /27/, and the comprehensive survey on heat transfer in the supercritical range by Pioro (2003) /28/).

It is then due to the relatively low density and high heat capacity of the supercritical fluid (see Figure 1.4) that a fast spectrum reactor could be designed, since less coolant is needed to cool the core and therefore the neutron moderation can be kept low. For the same reason another requirement for the achievement of a fast spectrum is a tight lattice configuration (small pitch over diameter ratio), which is one of the specific characteristics of the SCFR that, together with the highly enriched fuel composition (~23%) and possibly with a relatively large content fraction of minor actinides, brings questions regarding the safety behavior of the reactor under transient conditions.

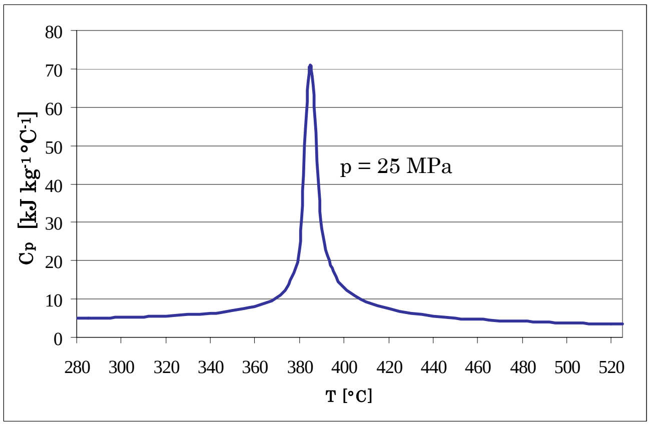

Figure 1.4: Heat capacity diagram for water

In fact, the SCFR's safety characteristics lie between a light water reactor and a fast reactor system: from the fast reactor design it "inherited" e.g. the tendency to positive coolant void reactivity, from the LWR design it inherited the pressurized primary system and therefore the problem of a potentially rapid loss of coolant under pipe break conditions. In other words, because of the prevalence of fast fissions, a loss of supercritical water, which in the case of the SCFR acts at the same time as coolant and moderator slowing down the neutrons, hardens the spectrum; therefore, a loss of coolant is a loss of a neutron absorber, hence the growth of the neutron population and therefore the positive reactivity coefficient. In LWRs the moderating function of water is usually predominant, and a loss of coolant decreases the reactivity of the system. These reactors are also called undermoderated.

Several safety analyses were consequently performed in the past years to evaluate the behavior of this reactor under the most common accident and transient conditions. Some of these studies focus on the identification of the relevant sequences i.e. which accident fault tree path would lead to the worst consequences [Lee (1999) /29/].

Others regard the general plant safety e.g. analyzing the reactor response to a Loss Of Coolant Accident (see for instance Oka (1997) /30/ for an overview of involved the safety systems).

Other investigations outline the safety criteria e.g. maximum allowed clad temperature during specific transients (see for instance Okano (1997) /31/, and again [Okano (1998) /32/], [Kitoh (1999) /33/], [Okano (1996) /34/], and [Kitoh (1998) /35/] for the results relative to control rod, flow and pressure induced transients), and reactor transient behavior [Kitoh (2001) /36/].

Other efforts were put into the development of new tools of analysis (like the LOCA analysis code described in Lee (1998) /37/), but the publications of interest for this thesis are the ones, which mainly relate to core design both from a pure thermal-hydraulic point of view of establishing safety criteria, such as the maximum operating cladding temperature [Mukohara (1999) /38/], or from a more comprehensive point of view of outlining conceptual design characteristics, such as a radial heterogeneous core structure [Jevremovic (1994) /39/], or the arrangement of the core internals [Tanaka (1996) /40/].

As mentioned, the SCFR has a tendency to have a positive void reactivity coefficient; such a behavior would seriously hinder the future development of this reactor, since a negative void is a fundamental requirement for the inherent safety of water-cooled reactors. LOCAs are in fact design basis accidents for pressurized systems. In order to overcome this problem, and to meet the safety requirements, special solid moderator strata were introduced within the core in order to avoid an excessive hardening of the spectrum and to increase the number of captures [Jevremovic (1993) /41/ and Oka (1996) /42/]. This finally led to the development of a radially heterogeneous core design, divided in seeds and blankets, both radially and axially, and the above mentioned zirconium hydride layers. The adoption of a heterogeneous core configuration should then result in an overall negative coolant void coefficient of reactivity. On the other hand, because of the specific characteristics of the SCFR, and of the chosen complex core arrangement, void effect calculations are inevitably accompanied by uncertainties, as discussed in detail in [Mori (2003) /43/].

It is precisely because of these early findings that more detailed studies were then started to assess the basic feasibility of the mentioned SCFR core design. New models and new tools of analysis were then developed and implemented utilizing various codes. For the assessment of the neutronics characteristics different code systems were used: deterministic based on transport and diffusion theory (TWODANT /44/, RHEIN /45/) and stochastic Monte-Carlo (MCNP /46/), together with dedicated cross section libraries processing (NJOY /47/). For the assessment of the fluid-dynamics characteristics a dedicated code was written (MXN[2]) and tested against an extended version of SIMMER-III /48/, which includes supercritical water equations of state.

SIMMER-III is developed by Japan Nuclear Cycle Development Institute in collaboration with Forschungszentrum Karlsruhe, Commissariat à l'Energie

---

[2] MXN is the name of the simple fluid-dynamics code that was developed for steady-state analyses.

Atomique (CEA) and Institut de Radioprotection et de Sûreté Nucléaire. SIMMER-III is a two-dimensional, three-velocity-fields, multi-phase, multi-component, Eulerian fluid dynamics code coupled with a structure model (fuel pins etc.) and space-, time- and energy-dependent neutron dynamic model. It uses an elaborate scheme of equations of state functions for fuel, steel, coolant (light and heavy liquid metals, water and gas), absorber and simulation materials, such as special alloys used in experiments [Tobita (2000) /49/]. In neutronics, the transient neutron flux distribution is calculated with the improved quasi-static method [Otto (1986) /50/], while for the space dependent part, a TWODANT-based flux shape calculation scheme is implemented [Buckel (1999) /51/]. It is precisely because of its inherent capabilities to perform coupled fluid-dynamics/neutronics calculations that this system code was chosen to perform the initial analysis of the SCFR. Successively a more refined tool was implemented for the neutronics modeling: MCNP coupled with the mentioned dedicated fluid-dynamics code.

MCNP (Monte-Carlo N-Particle) is a general-purpose, continuous energy, generalized-geometry, time-dependent, coupled neutron/photon/electron Monte-Carlo transport code, which also endorses the capability to calculate k-effective eigenvalues for fissile systems as a standard feature. In brief, MCNP is based on a statistical sampling processes founded on the selection of random numbers—analogous to throwing dice in a gambling casino, hence the name “Monte-Carlo”, and is particularly useful for complex problems that cannot be modeled by computer codes that use deterministic methods. The input file consists of very detailed information about the problem such as: geometry specification, description of the materials, selection of cross-sections, location and characteristics of sources, type of answers, and variance reduction techniques to increase efficiency.

1.3 Aim of this Work

Even though, as mentioned before, SCWRs have been studied for several years now, most of the published work focuses on conceptual design and specific aspects of the reactor, such as transient and general neutronics analyses. Furthermore, the main thrust of the research work is being put on the thermal spectrum option, to some extent neglecting a detailed study of the core design both from the fluid dynamics and neutronics point of view.

The SCFR is a strongly coupled system; the absence of a well-distributed moderator independent of the coolant implies a strong interaction between fluid dynamics and neutronics, therefore the need for coupled calculations. Furthermore, the heterogeneity of the core introduces very high local neutron fluxes and therefore very high local power density and corresponding strong gradients of these quantities. The coolability and the hydraulic stability of this reactor in combination with specific safety requirements, such as a negative void reactivity coefficient, demand a careful and accurate core and fuel design.

Given the flexibility of the MCNP geometrical model and the flexibility of the implementation of new equations of state in SIMMER [Morita (1998) /52/] it was decided to combine the two systems to perform steady state calculations, taking into account previously validated neutronics feedbacks [Mori (2003) /53/]. The application of a coupled system would take into account correctly the coolant density axial profiles (as mentioned earlier the water density inlet/outlet ratio is about 9), and introduce a detailed spatial distribution of the physical properties (e.g.: fuel and coolant temperatures), with the consequent benefit on the accuracy of the estimation of the reactor safety parameters and particularly of the void reactivity coefficient [Mori (2003) /54/].

On the other hand, the implementation of a fully coupled SIMMER/MCNP system would require a prohibitively long computational time, since SIMMER-III, a transient code, would need to reach a new pseudo steady state at every time step of the coupled procedure, and as MCNP is a stochastic code, it will need to track an enormous amount of particles to achieve a sufficiently adequate statistical accuracy. For this reason, a steady state pure fluid-dynamics fast-running code was developed (MXN), which could use the power distribution calculated by MCNP as an input and subsequently easily calculate fuel and coolant temperatures and densities to be reintroduced in MCNP. The SIMMER/MCNP coupled system was therefore only used to evaluate the initial conditions and accelerate the convergence of the solution.

Using these tools, core design variants and improvements are carefully investigated and eventually introduced in order to achieve a higher reactor safety standard, a better fluid-dynamics design, and in particular to guarantee a negative void reactivity.

CHAPTER 2

MATHEMATICAL AND PHYSICAL MODELS

In order to investigate the different aspects that characterize the SCFR, the development of new mathematical and physical models was not essential. What was essential instead was to follow a new methodology and to implement a new framework for the combination of the known models.

As mentioned before, different "codes" were applied to study the fluid dynamics and the neutronics aspects of the Supercritical water Fast Reactor: SIMMER-III, RHEIN, MCNP and MXN. SIMMER includes the neutronics package DANTSYS and in the course of this work TWODANT was used for the preliminary neutronics investigations together with RHEIN, which is a steady state diffusion code. The basic models adopted in the codes will be described in the following paragraphs introducing, when necessary, the description of the specific features of the codes themselves.

2.1 System description, geometry, and integration domain

The analyses that will be performed in the course of this work will concentrate on the core of the reactor and therefore the details related to the primary loop and its thermodynamics cycle will be neglected. The area of interest of the analysis is roughly represented in Figure 1.2, which shows the so-called “internals” of the SCFR.

The main operating parameters and the geometrical details of the core structure, including subassembly and pin dimensions, are summarized in Table 2.1, while a more detailed depiction of the core configuration is given in Figure 2.1, which shows a mid plane axial section, and outlines one of the specific characteristics of this system: its highly heterogeneous structure.

Reactor Characteristics	Value
Thermal/electric power [MW]	3832/1698
Coolant inlet/outlet temperature [K]	553/796
Thermal efficiency [%]	44.3
Operating pressure [MPa]	25
Effective core height/diameter [m]	3.76/3.50
Fuel	MOX
Lower/upper axial blanket length [m]	0.2/0.2
Fuel/blanket assemblies number	270/163
Maximum linear power [W/cm]	382
Average power density including blanket [MW/m^3]	105
Fuel rod outer diameter/pitch [mm]	10.2/11.5
Blanket water channel inner diameter/pitch [m]	4.00/10.1
Cladding/thickness [mm]	Inconel/0.54
Blanket cladding/thickness [mm]	Inconel/0.26
Pu fissile enrichment [%] inside/middle/outside	13.96/12.58/13.46
Pu oxide fissile inventory [t]	11.6
Average burn up [GWd/t]	43.4
Coolant void reactivity coefficient [10^{-5}dk/k/%void]	-6.49
Operating cycle [day]/batch	390/3
Conversion ratio	1.034

Table 2.1: SCFR main characteristics

There are four different regions that have a different specific composition and role in the design of this reactor.

1. The “seed” regions (red). These are the driver regions, where most of the fissions occur. They are loaded with plutonium-enriched uranium oxide fuel (MOX), with an average plutonium enrichment of 23%. The detailed radial

arrangement of the composition of these areas is illustrated in Figure 2.2, which shows a radial section of the core (reflectors are not included).

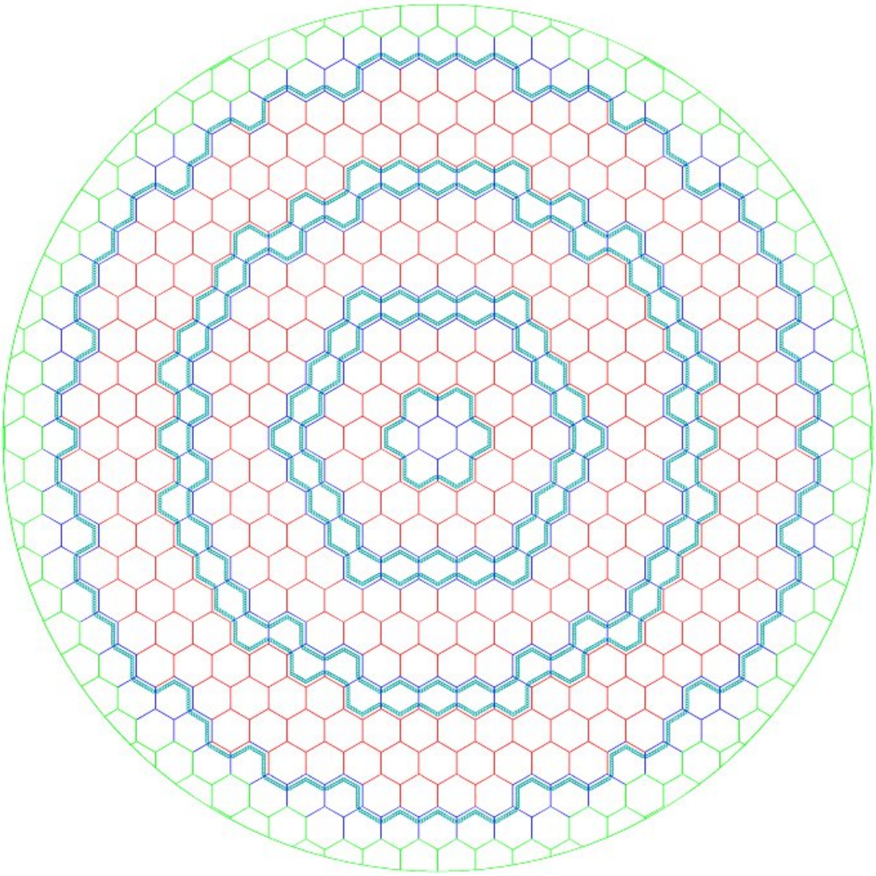

Figure 2.1: Axial section of the SCFR core

2. The "blanket" regions (blue). These are the regions, which are loaded with depleted fuel (^{235}U ~0.5%) and can potentially host the minor actinides' targets [Iwasaki (2001) /20/][3]. They are located at the top and at the bottom of the inner core (axial blankets) and among the seed areas (radial blankets). Most of the neutron captures occur here and they are fundamental for the achievement of a negative void reactivity coefficient.

3. The "hydride" regions (dark blue, thin elements within the blanket regions). These are the regions where the solid moderator (zirconium hydride, $ZrH_{1.7}$) is located. They are placed within the blankets at about 1 cm from the seed areas, to optimize their performance. They slow down the neutrons coming from the seeds, in particular in voided conditions, when there is no coolant to

---

[3] This option is not investigated in this work; the blanket is therefore made of UO_2 only, (99.5% of ^{238}U).

moderate them. Together with the blankets they are fundamental for the achievement of a negative coolant void reactivity. In fact, they increase the overall neutron absorption (in the blankets and in the seeds) and they decrease the neutron production in the blankets preventing, or decreasing the number of fast fissions in ^{238}U [Jevremovic (1993) /55/].

4. The "reflector" regions (green). These regions surround the core providing a better neutron economy in the reactor partly reflecting the neutrons that would otherwise escape. They are constituted by supercritical water in its fluid form (lower and radial reflector), or gas form (upper reflector).

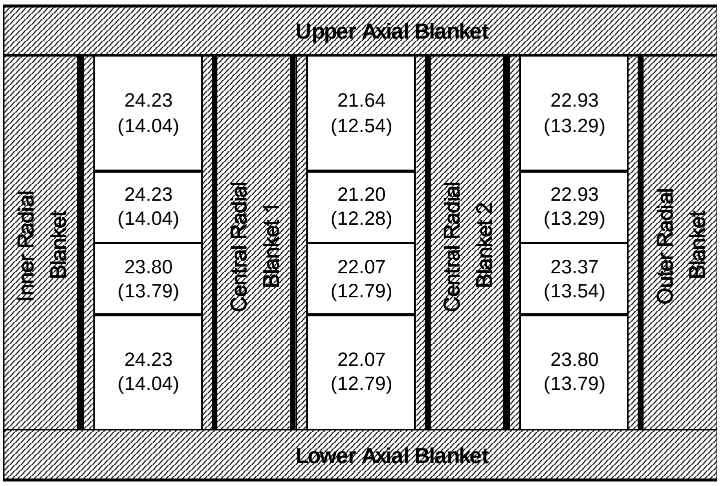

Figure 2.2: Core radial section and Pu enrichment distribution (weight % of ^{239}Pu and ^{241}Pu)

These four regions and coolant flow paths need to be described, together with the details of the specific components, according to the models adopted by the codes that are used for the calculations. In order to render accurately into the code language both the heterogeneity of the geometry and of the material composition, the adoption of several approximations is necessary.

Moreover, the significantly different design of the seed (see Figure 2.3) and of the blanket subassemblies needs to be taken into account; besides, the arrangement of the zirconium hydride layers changes from subassembly to subassembly, further complicating the modeling of the system (see Figure 2.4, where the solid light blue areas represent the zirconium hydride layers).

With reference to Figure 2.4, which collects all the different possible solid moderator arrangements in this core, it is important to underline the peculiar layout of the blanket fuel pins; the pin is hollow, therefore the coolant flows inside the pin itself.

The heat transfer characteristics of this configuration differ from the ones of the seed and should eventually be modeled specifically. On the other hand, the power produced in the blanket is negligible and therefore this approximation will not affect the results appreciably. However, this is yet another specific feature of the SCFR that needs to be correctly modeled, especially for its effects on the neutronics characteristics of the reactor.

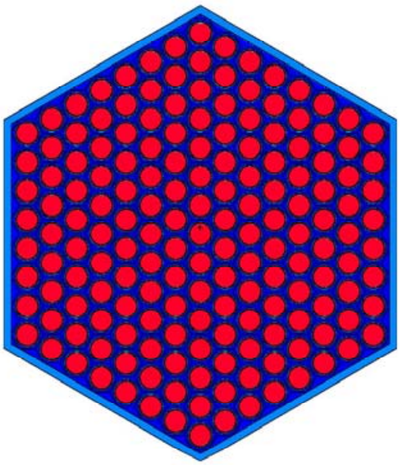

Figure 2.3: Geometrical detail of the seed subassembly

The separation of the core geometry into macro regions, the arrangement of the cells within these regions, and the development of an equivalent geometry to be used for the application of the models is called nodalization and it is usually unique for every code. The development of the different nodalizations will be described in detail in Chapter 3; suffice to know at this stage of the work that only a Monte-Carlo method would be able to describe and resolve the illustrated reactor with a level of detail equivalent to a single pin effect, and therefore accurate enough to evaluate the illustrated local effects, which play an important role in this system.

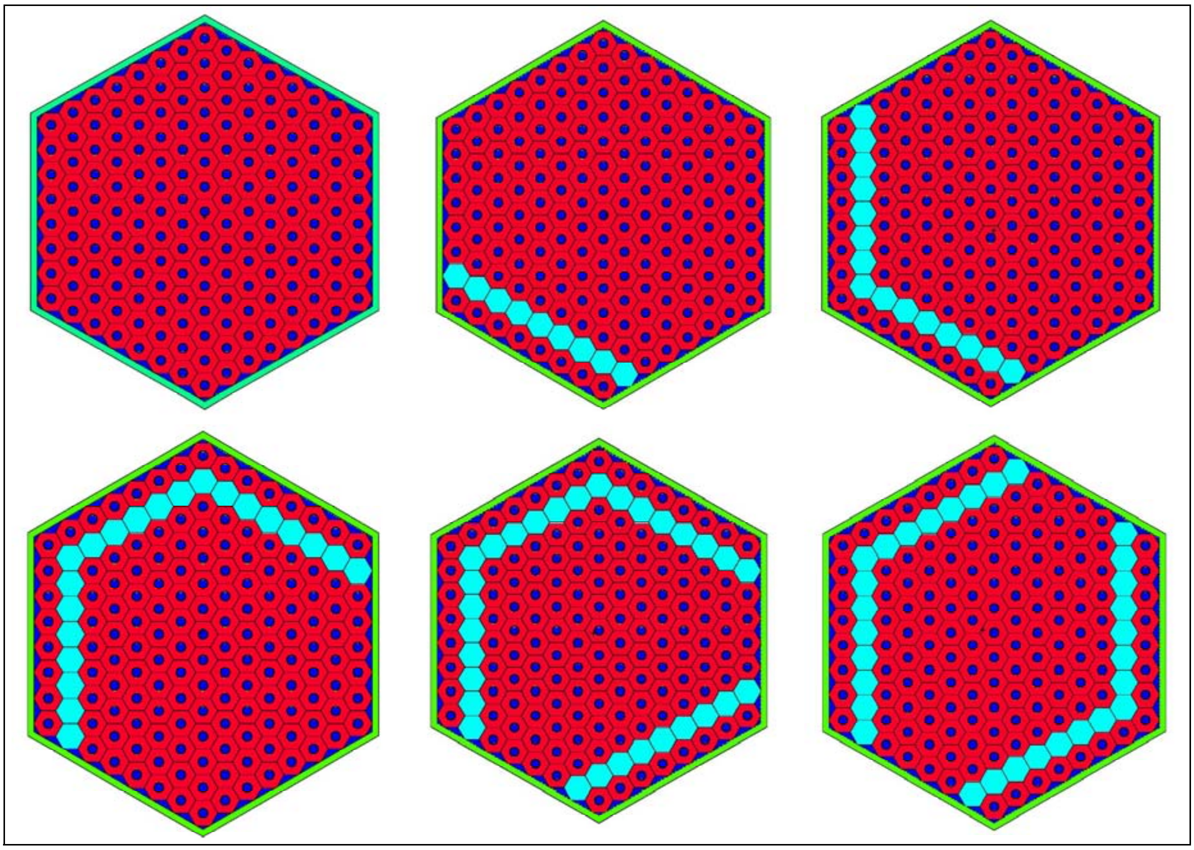

Figure 2.4: Geometrical details of the blanket subassemblies

2.2 Description of the models

One neutronics and one fluid-dynamics model form the basis of this numerical work, although in the case of neutronics two radically different methods will be used to solve the transport equation namely the S_n method and the Monte-Carlo method. It goes beyond the scope of this work to treat in detail the theory of neutronics transport or of single-phase flows, therefore only the basic balance equations solved in the codes will be described here leaving a more detailed treatment of the subject to dedicated text books, see for instance [Bell & Glasstone (1979) /56/], [Todreas (1993) /57/], and [Todreas (1990) /58/], and the considerations about the solution methods to Chapter 3.

Fluid-Dynamics Model

The following paragraphs describe the set of equations that have been implemented in a simple code developed to generate steady state fuel pin and core thermal hydraulics data (MXN). The input parameters are the total power and its profile, both axial and radial, and the coolant inlet temperature. The output of the code is a point wise map of temperatures for the fuel, the fuel cladding and the coolant. The adoption of this simple tool allows to determine the nominal steady state conditions for the SCFR and therefore estimate more accurately the k-effective for the given core design, hence improving the accuracy of the void reactivity coefficient calculation.

The basic assumptions regard the geometry, which is equivalent to multiple, heated channels that are connected only at the plena. It will then be assumed that only a one dimensional flow occur in the system and for simplicity only steady-state is considered for the applied form of the equations, although the general form will be usually given.

Conservation of mass

The Eulerian form of the mass conservation equation for single-phase flow (supercritical water does not exhibit a change of phase and we are only concerned with steady state calculations beyond the supercritical point) is the well-known expression (2.1) (see Nomenclature for the definition of all used symbols).

$$\frac{\partial \rho}{\partial t} + \nabla \cdot (\rho \vec{v}) = 0 \tag{2.1}$$

Which, given the fact that only steady state analyses and one dimensional axial flows are being considered, then becomes:

$$\frac{\partial}{\partial z}G = 0 \quad \Rightarrow \quad GA = \dot{m} = \text{constant} \tag{2.2}$$

Conservation of momentum

The momentum equation expresses mathematically the fact that the rate of change of momentum in the control volume equals the momentum flow rate into the control volume minus the momentum flow rate out of the control volume plus the net external force on the control volume. In general, the forces that must be accounted for include: gravitational, electric, magnetic and surface forces (pressure, internal frictional effects and shear forces). Thus, the general form of the momentum conservation equation in the z direction (incompressible fluid and constant viscosity) becomes:

$$\rho \frac{\partial v_z}{\partial t} + \rho \nabla \cdot v_z \vec{v} = -\frac{\partial p}{\partial z} + \mu \nabla^2 v_z + \rho f_z \tag{2.3}$$

Which, being gravity the only body force acting on the fluid, and given the initial assumptions, is reduced for a one-dimensional axial flow to:

$$\frac{\partial}{\partial z}\left(\frac{G^2}{\rho}\right) = -\frac{\partial p}{\partial z} - \rho g \cos\theta - \frac{f G |G|}{2 D_e \rho} \tag{2.4}$$

Conservation of energy

The energy equation expresses the fact that the rate of change of total internal energy in an infinitesimal volume must be equal to the rate at which internal energy is brought into the volume by the mass inflow, minus that removed by the mass outflow, plus the heat transported diffusively or generated, minus the work performed by the medium in the volume and the work needed to put the flow through the volume. There are different forms for the conservation of energy equation, which are characterized by the different form of energy used for the balance e.g.: internal energy, enthalpy, and kinetic energy. A common way to write the conservation of energy equation is:

$$\rho c_p \frac{DT}{Dt} = \rho c_p \left(\frac{\partial T}{\partial t} + \vec{v} \cdot \nabla T\right) = -\nabla \cdot q'' + q''' \tag{2.5}$$

Which, because of the specific properties of supercritical water (e.g.: $c_p \to \infty$ at the supercritical point), might be extremely difficult to solve numerically incurring in singularities or abrupt physical property changes of the coolant. For this reason another form of the conservation of energy equation was used:

$$\rho\frac{Dh}{Dt}=\frac{\partial}{\partial t}\left(\rho h\right)+\nabla\cdot\left(\rho h\vec{v}\right)=-\nabla\cdot\vec{q}''+q'''+\frac{Dp}{Dt}+\phi \tag{2.6}$$

Where ϕ is the dissipation function, which is going to be neglected. Therefore, adopting the same assumptions that were introduced for the other conservation equations, the expression describing the conservation of energy becomes:

$$\dot{m}\frac{\partial}{\partial z}h=\chi\left(r,z\right) \tag{2.7}$$

Where $\chi\left(r,z\right)$ is the linear power distribution in the core, and (2.7) is the equation that is solved in the code, assuming that $\chi\left(r,z\right)$ can be separated in the *r* and *z* direction $\chi\left(r,z\right)=\chi_m\chi_r\left(r\right)\chi_z\left(z\right)$, where $\chi_r\left(r\right)$ and $\chi_z\left(z\right)$ are normalized distribution functions, and χ_m is the amplitude.

Equation (2.7) can be then solved separately for each channel and therefore for upflow conditions and for channel *n*:

$$h_n\left(z\right)=h_n\left(0\right)+\frac{1}{\dot{m}_n}\int_0^z\chi\left(r_n,z\right)dz \tag{2.8}$$

And therefore, being the pressure of the system a known parameter, it is possible to calculate the density and temperature distribution in the channels of the SCFR core, directly applying the tabular function for the equation of state of water (see for instance Wark (1995) /59/ for a detailed theoretical treatment of the equation of state functions, or Wagner (1998) /24/ for the industrial formulation of the properties of water and steam).

The equation of state of water

The evaluation of the properties such as enthalpy for a substance requires the knowledge of the *pvT* behavior under the given conditions. The equilibrium relations between the intensive properties of a substance and their pressure *(p)*, specific volume *(v)*, and temperature *(T)* are known as equations of state and have the functional form:

$$f\left(p,v,T\right)=0 \tag{2.9}$$

For a general treatment of the problem we will refer to non-dimensional quantities for the three mentioned variables normalizing them by their respective values at the critical point:

$$p_r = \frac{p}{p_c}; \quad v_r = \frac{v}{v_c}; \quad T_r = \frac{T}{T_c}; \tag{2.10}$$

If the pressure approaches zero in value, all gases behave as ideal gases and therefore the renowned ideal gas equation of state:

$$pv = RT \tag{2.11}$$

The simplest method mathematically to render (2.11) correctly, so that it predicts real gas behavior, is to introduce a compressibility factor Z, which corresponds to the ratio between the real specific volume and the ideal one [Wark (1995) /59/]. Equation (2.11) then becomes:

$$pv = ZRT \tag{2.12}$$

The concept of the compressibility factor is an important one, because it introduces a single dimensionless parameter to predict the behavior of a substance. Therefore equations of state can be written in the form:

$$Z = f\left(T_r, p_r\right) \tag{2.13}$$

Which is the formulation of van der Waals' theorem of corresponding states, which states that any pure gas at the same reduced temperature (T_r) should have the same compressibility factor, and is generally applicable to any substance even in a liquid phase.

There exist several expressions for equation (2.13); typically, the simplest ones capable of predicting both vapor and liquid behavior are cubic polynomial equations in the specific volume. Good examples are the van der Waals equation, or the Redlich-Kwong equation, which represents an improvement of van der Waals', or the Redlich-Kwong-Soave (equation (2.14)), which increases the accuracy of the correlation near and below the critical temperature by the introduction of an additional third fitting parameter: the acentric factor ω (equation (2.18)).

$$p = \frac{RT}{v-b} - \frac{a\alpha}{v\left(v+b\right)} \tag{2.14}$$

$$a = \frac{0.42748 R^2 T_c^2}{p_c} \qquad b = \frac{0.08664 R T_c}{p_c} \tag{2.15}$$

$$\alpha = \left[1 + S\left(1 - T_r^{1/2}\right)\right]^2 \tag{2.16}$$

$$S = 0.48508 + 1.5517\omega - 0.15613\omega^2 \text{ (Graboski \& Daubert)} \tag{2.17}$$

$$\omega \equiv -1.0 - \log\left(p_r^{sat}\right) T_{r=0.7} \tag{2.18}$$

In order to give closure to the fluid-dynamics steady state formulation that we are dealing with, one more equation defining one of the variables, the enthalpy, is needed. The definition of enthalpy is given by the well-known equation (2.19), from which equation (2.20) derives.

$$h = u + pv \quad \Rightarrow \quad dh = du + pdv + vdp \tag{2.19}$$

$$dh = c_p dT + \left[v - T\left(\frac{\partial v}{\partial T}\right)_p\right] dp \tag{2.20}$$

Where c_p is the isobaric heat capacity defined as

$$c_p = \left(\frac{\partial h}{\partial T}\right)_p \tag{2.21}$$

We then have a set of 5 equations: (2.2),(2.4), (2.7), (2.14), and (2.20); with six unknowns: ρ, T, p, h, $\dot{m}$, and v. One boundary condition is therefore needed, either the coolant inlet/outlet temperature difference ΔT, the pressure loss Δp, or the coolant flow rate $\dot{m}$. In this case ΔT is a design requirement set in order to guarantee the achievement of a desired plant efficiency higher than 42%. Therefore, ΔT will be used as boundary condition for the solution of the illustrated set of equations. Finally the main variables of interest for the definition of our problem, in particular for the linked neutronics calculations, are calculated: coolant density and temperature distributions. Yet for the correct determination of the neutronics calculation another fundamental variable needs to be evaluated: the fuel temperature.

Determination of the fuel pin temperature

There are four stages of heat transfer to be taken into account for the determination of the average fuel temperature: conduction within the fuel, conduction across the gap, conduction across the clad, and convection to the coolant. Since we are treating this problem in a reverse manner, the fuel temperature is calculated starting from the coolant temperature distribution, we will start examining the heat transfer from the cladding to the coolant. The heat flux from the cladding to the coolant is given by:

$$Q = \frac{\chi(r,z)}{\pi d_{pin}} = h_{HT}\left(T_{co} - T_b\right) \tag{2.22}$$

Where h_{HT} is the heat transfer coefficient, T_{co} is the outer cladding temperature and T_b is the coolant bulk temperature. A specific validated correlation for the determination of the heat transfer coefficient for supercritical water flowing in a rod bundle is currently not available for the typical operating conditions of the SCFR [Pioro (2003) /27/]. Nevertheless, several authors (see for instance Tanaka (1996) /40/, Antoni (2003) /60/, Kataoka (2003) /61/, Sánchez (2003) /62/) for first analyses adopted the well-known Dittus-Boelter correlation (2.23), taking advantage of the fact that quite a few thermal-hydraulics system codes use it. A better correlation, although still approximate, is the Bishop[4] correlation [Bishop (1964) /63/] (2.24), which should prove sufficiently adequate for our purposes [Cheng (2001) /64/] and shows to be rather conservative, overcoming the overestimation of the heat transfer coefficient of Dittus-Boelter's formulation [Siefken (2003) /65/]:

$$\mathrm{Nu} = 0.023 \cdot \mathrm{Re}^{0.8}\,\mathrm{Pr}^{0.4} \tag{2.23}$$

The Bishop correlation then is:

$$\mathrm{Nu} = 0.0069 \cdot \mathrm{Re}^{0.90}\,\overline{\mathrm{Pr}}^{0.66} \cdot \left(\frac{\rho_w}{\rho_b}\right)^{0.43} \cdot \left(1 + \frac{2.4D_e}{L}\right) \tag{2.24}$$

$$\overline{\mathrm{Pr}} = \left(\overline{C}_p \frac{\mu}{k}\right) \text{ and } \overline{C}_p = \frac{h_w - h_b}{T_w - T_b} \tag{2.25}$$

$$\text{where } \mathrm{Nu} = \frac{hD_e}{k}, \text{ and } \mathrm{Re} = \frac{GD_e}{\mu}. \tag{2.26}$$

Where D_e is the effective hydraulic diameter of the fuel channel we are considering for the analysis, k is the coolant thermal conductivity, μ is the dynamic viscosity, L is the length of the channel, and for simplicity reasons C_p is given by the integral over the operating temperature range of the curve shown in Figure 1.4.

---

[4] As it will be discussed later the approximations introduced in MXN are such that the ratio between the wall and bulk coolant density will be taken equal to one, and an average constant C_p will be used.

Applying then the illustrated correlations, it is possible to calculate T_{co} and consequently the cladding inner temperature, T_{ci}, applying equation (2.27). Where k_c is the thermal conductivity of the clad, R_{ci} and R_{co} are the clad internal and external radii respectively.

$$T_{ci} - T_{co} = \frac{\chi(r,z)}{2\pi k_c} \ln \frac{R_{ci}}{R_{co}} \tag{2.27}$$

One last equation is then needed to calculate the fuel surface temperature and subsequently its average:

$$\chi(r,z) = h_g 2\pi R_{fo} \left(T_{fo} - T_{ci}\right) \tag{2.28}$$

Where h_g is the gap conductance, T_{fo} is the fuel surface temperature, and R_{fo} is the fuel outer radius. For the open gap case, that is normally the initial condition, the gap conductance is estimated by:

$$h_g = \frac{k_{gas}}{\delta_{eff}} + \frac{\sigma}{\frac{1}{\varepsilon_f} + \frac{1}{\varepsilon_c} - 1} \frac{T_{fo}^4 - T_{ci}^4}{T_{fo} - T_{ci}} \tag{2.29}$$

Where k_{gas} is the thermal conductivity of the gas, δ_{eff} is the effective gap clearance, σ is the Stephan-Boltzmann constant (5.67×10^{-12} Wcm^{-2}K^{-4}), and ε_f, ε_c are the surface emissivities of the fuel and cladding, respectively. Equation (2.29) can be roughly approximated by:

$$h_g = \frac{k_{gas}}{\delta_g + \delta_f + \delta_c} \tag{2.30}$$

Where δ_g = nominal gap clearance (2.15×10^{-4} m), δ_f takes into account the surface roughness on the fuel ($\sim 10^{-5}$ m), and δ_c = the roughness effect on the clad ($\sim 10^{-7}$ m). Equation (2.30) is sufficiently accurate for our purposes and rids us of unwanted implicit dependence of h_g on temperature[5].

Calculation of the fuel temperature

In order to calculate the fuel temperature, a few assumptions are necessary. The most important of which is that the heat source in the fuel is considered uniform in

---

[5] It may be worthwhile to mention that h_g does not depend only on the mentioned parameters. As a matter of fact h_g may change significantly during reactor operation and as a consequence of long-term irradiation, since the involved parameters may vary considerably as a function of time.

the radial direction; that is the neutron flux is flat and there is no neutronics spatial self-shielding within the pin. This may become a poor approximation for some LWR designs with thick pins in a well-thermalized neutron spectrum. In fact, an overestimation of the fuel central temperature might occur, because of the spatial resonance-self-shielding effect. However, these approximations are negligible for a SCFR, due to the small pin diameter and the fast spectrum.

Therefore, the model of fuel heat conduction does not differ from a cylindrical rod with an internal heat source. A second important assumption is to neglect the axial heat transfer hence, considering a one-dimensional radial heat balance on the cylindrical element *dr*, (2.31) can be written (per unit length and assuming steady state):

$$-2\pi rk\frac{dT}{dr}+q'''\cdot 2\pi r dr=-2\pi\left[rk\frac{dT}{dr}+\frac{d}{dr}\left(rk\frac{dT}{dr}\right)dr\right] \tag{2.31}$$

Where T is the fuel temperature, k the thermal conductivity, q''' the uniform volumetric heat source ($\mathrm{Wm^{-3}}$). Simplifying the above equation the steady state heat conduction expression (2.32) is obtained.

$$\frac{1}{r}\frac{d}{dr}\left(rk\frac{dT}{dr}\right)+q'''=0 \tag{2.32}$$

Note that the thermal conductivity depends strongly on temperature and therefore it becomes in general a function of r. The integration of (2.32) yields:

$$rk\frac{dT}{dr}+q'''\frac{r^2}{2}+C_1=0 \tag{2.33}$$

For an annular fuel pellet with an internal cavity radius (R_v), no heat flux exists at R_v. For a solid pellet, which corresponds to the SCFR case, $R_v = 0$, no heat flux exists at $r=0$. Hence the general heat flux condition that can be applied is:

$$q''\big|_{r=R_v}=-k\frac{dT}{dr}\bigg|_{r=R_v}=0 \text{ and therefore } C_1=-\frac{q'''R_v^2}{2} \tag{2.34}$$

Equation (2.33) can be integrated between r and R_v to yield, after rearrangement:

$$-\int_{T_{\max}}^{T}kdT=\frac{q'''}{4}\left(r^2-R_v^2\right)+C_1\ln\left(\frac{r}{R_v}\right) \tag{2.35}$$

and therefore for a solid fuel pellet ($R_v = 0$ and $C_1 = 0$), equation (2.35) becomes:

$$-\int_{T_{\max}}^{T} k dT = \frac{q''' r^2}{4} \tag{2.36}$$

which, taking a linear heat rate:

$$q' = \pi R_{fo}^2 q''' \tag{2.37}$$

gives:

$$-\int_{T_{\max}}^{T_{fo}} k dT = \frac{q'}{4\pi} \tag{2.38}$$

and finally, for a constant conductivity:

$$T_{ave} - T_{fo} = \frac{1}{2}\left(T_{\max} - T_{fo}\right) = \frac{q'}{8\pi k} \tag{2.39}$$

It is interesting to note that the temperature difference across a solid fuel pellet is determined by q' and is independent of the pellet radius R_{fo}. Thus a limit on q' is directly implied by a design requirement on the maximum fuel temperature.

If the dependence of thermal conductivity on T is taken into account, it is possible to use an analytic interpolation and then integrate equation (2.38). A typical expression for a MOX fuel (80% uranium, 20% plutonium) at 95% theoretical density and for oxygen to metal ratio of two is [Waltar (1981) /66/]:

$$k = \left(0.042 + 2.71\times10^{-4} T\right)^{-1} + 6.9\times10^{-11} T^3 \tag{2.40}$$

Where k is expressed in $\mathrm{Wm^{-1}\,K^{-1}}$ and T is in Kelvin.

Equations (2.30) and (2.40) are sufficiently accurate for our studies, since the average plutonium enrichment of the SCFR fuel is ~23%, its theoretical density corresponds to the one of the given formula, but above all the analyses performed do not need at this stage to take into account burn-up effects, which would affect inevitably both gap conductance and the integral of fuel conductivity.

At a first approximation, by considering the series of thermal resistances posed by the fuel, the gap, the cladding, and the coolant, it is possible to relate in a single expression the temperature drop $\left(T_{ave} - \overline{T}_m\right)$ to the linear heat rate (where R_g is the mean gap radius):

$$T_{ave} - \bar{T}_m = q' \left[\frac{1}{8\pi \bar{k}_f} + \frac{1}{2\pi R_g h_g} + \frac{1}{2\pi k_c} \ln\left(\frac{R_{co}}{R_{ci}} \right) + \frac{1}{2\pi R_{co} h} \right] \tag{2.41}$$

Neutronics Model

The transport equation

The equation which describes the time development of the neutron population in the phase space is called the "Boltzmann's transport equation". Following the approach of Weinberg and Wigner (1958) /67/ it will be derived as was first done by Boltzmann by writing a balance equation considering the causes for the increase and decrease of the number of particles (in this study neutrons) at $\vec{r}$ (within $d\vec{r}$) with energy E and direction $\vec{\Omega}$ (within $dE\, d\vec{\Omega}$).

First of all, one must define the angular flux $\Psi\left(\vec{r}, E, \vec{\Omega}, t\right) d\vec{r}\, dE\, d\vec{\Omega}$, the fundamental variable of transport theory, which corresponds to the number of neutrons in the volume element $d\vec{r}$ around $\vec{r}$, in the energy element dE around E, and whose directions of motion lie in the solid angle $d\vec{\Omega}$ around $\vec{\Omega}$, multiplied by the speed of these neutrons, that is by $v = \sqrt{2E/M}$, where M is the neutron mass. The distribution in the six-dimensional phase space, Ψ, contains more information than a simple distribution in ordinary, three-dimensional, space and for a large number of neutrons it obeys the Boltzmann equation, which is an exact expression of the neutron balance.

The position $\vec{r}$ and energy direction $\left(E, \vec{\Omega}\right)$ of the neutrons change for two reasons. The coordinates $\vec{r}$ change as a result of the uniform straightforward motion of the neutrons; the energy and direction of motion change because the neutrons suffer collisions. The first type of change leaves $\left(E, \vec{\Omega}\right)$ unaltered; the second type of change leaves $\vec{r}$ unchanged.

The flow in the phase space connected with the first change affects only $\vec{r}$; it creates a current $\vec{\Omega}\Psi\left(\vec{r}, E, \vec{\Omega}, t\right)$. As a result of this current, the density $v^{-1}\Psi$ changes by $-\mathrm{div}_r\left(\vec{\Omega}, \Psi\right)$ or:

$$\frac{1}{v}\left(\frac{\partial\Psi}{\partial t}\right)_1 = -\Omega_x\frac{\partial\Psi}{\partial x} - \Omega_y\frac{\partial\Psi}{\partial y} - \Omega_z\frac{\partial\Psi}{\partial z} = -\vec{\Omega}\cdot\mathrm{grad}_{\mathrm{r}}\Psi \tag{2.42}$$

The components of $\vec{\Omega}$ and of $\vec{r}$ are independent variables, so that, when with respect to the variables of one set, those of the other set must be regarded as constants. For the same reasons the symbols "div" and "grad" must be given an index $\vec{r}$ or $\vec{\Omega}$ to specify the set ($\vec{r}$ or $\vec{\Omega}$) with respect to which the differentiations of the operator "div" or "grad" are to be undertaken.

The second type of change affects only $\left(E,\vec{\Omega}\right)$ and it is associated with collisions of neutron with the surrounding medium[6]. These depend on the cross-sections. The macroscopic cross-sections for changing the energy and direction $E',\vec{\Omega}'$ into an energy and direction range $dE,d\vec{\Omega}$ at $E,\vec{\Omega}$ will be denoted by $\Sigma\left(\vec{r},E'\rightarrow E,\vec{\Omega}'\rightarrow\vec{\Omega}\right)dEd\vec{\Omega}$. The variable $\vec{r}$ is necessary because, in an inhomogeneous medium, the cross-section may depend on the position. The macroscopic absorption cross-section will be denoted by $\Sigma_a\left(\vec{r},E\right)$. The change of density due to collisions is, then:

$$\begin{gathered}\frac{1}{v}\left(\frac{\partial\Psi\left(\vec{r},E,\vec{\Omega}\right)}{\partial t}\right)_2 = \int dE'd\vec{\Omega}'\Psi\left(\vec{r},E',\vec{\Omega}'\right)\Sigma_s\left(\vec{r},E'\rightarrow E,\vec{\Omega}'\rightarrow\vec{\Omega}\right)\\ -\int dE'd\vec{\Omega}'\Psi\left(\vec{r},E,\vec{\Omega}\right)\Sigma_s\left(\vec{r},E\rightarrow E',\vec{\Omega}\rightarrow\vec{\Omega}'\right)-\Psi\left(\vec{r},E',\vec{\Omega}\right)\Sigma_a\left(\vec{r},E\right)\end{gathered} \tag{2.43}$$

The first term on the right side corresponds to collisions in which the energy direction $\left(E',\vec{\Omega}'\right)$ is changed into $\left(E,\vec{\Omega}\right)$; the second one, to those in which $\left(E',\vec{\Omega}'\right)$ is changed into any $\left(E,\vec{\Omega}\right)$. The first two terms, therefore, correspond to scattering collisions. The last term accounts for the absorption.

The second term could also be written as $\Psi\left(\vec{r},E,\vec{\Omega}\right)\cdot\Sigma_s\left(\vec{r},E,\vec{\Omega}\right)$ because:

$$\Sigma_s\left(\vec{r},E,\vec{\Omega}\right) = \int dE'd\vec{\Omega}'\Sigma_s\left(\vec{r},E'\rightarrow E,\vec{\Omega}\rightarrow\vec{\Omega}'\right) \tag{2.44}$$

---

[6] Neutron-neutron interactions can be neglected because they are fairly rare.

gives the cross-section for any type of scattering. In (2.44), $\Sigma_s\left(\vec{r},E,\vec{\Omega}\right)$ may depend on the direction of the incident neutron; this would correspond to transport in an anisotropic medium like a crystal. Usually, the medium is isotropic, and the total scattering cross section is a function only of $\vec{r}$ and *E,* which is the assumption on which the rest of this model description will be based. In the classical treatise of the problem another important assumption is that the neutrons are in thermal equilibrium with the medium in which they diffuse (this implies that there is no capture), which would allow us to write the so-called equation of detailed balance:

$$\Psi\left(\vec{r},E,\vec{\Omega}\right)\cdot\Sigma_s\left(\vec{r},E\rightarrow E',\vec{\Omega}\rightarrow\vec{\Omega}'\right)=\Psi\left(\vec{r},E',\vec{\Omega}'\right)\cdot\Sigma_s\left(\vec{r},E'\rightarrow E,\vec{\Omega}'\rightarrow\vec{\Omega}\right) \tag{2.45}$$

In our case this assumption cannot be made, since we are dealing with an epithermal/fast neutron spectrum and therefore equation (2.45) is not generally valid. However it is possible to write an expression for the total change on the population density in phase space: the sum of the changes due to the two types of causes that were examined, that is the sum of equation (2.42) and equation (2.43):

$$\begin{aligned}\frac{1}{v}\frac{\partial\Psi\left(E,\vec{\Omega}\right)}{\partial t}&=-\vec{\Omega}\cdot grad_r\Psi\left(E,\vec{\Omega}\right)-\Psi\left(E,\vec{\Omega}\right)\left[\Sigma_s\left(E\right)+\Sigma_a\left(E\right)\right]\\&\quad+S\left(E,\vec{\Omega}\right)+\int dE'd\vec{\Omega}'\Psi\left(E',\vec{\Omega}'\right)\Sigma_s\left(E'\rightarrow E,\vec{\Omega}'\rightarrow\vec{\Omega}\right)\end{aligned} \tag{2.46}$$

The last term, $S\left(E,\vec{\Omega}\right)$, accounts for possible sources of neutrons.

Usually the source term is split into an internal and an external part. The internal part takes into account the so-called prompt and delayed fission neutrons whereas the external part could arise e.g.: from spontaneous fissions, or radioactive decay processes, spallation reactions as employed in concepts for Accelerator Driven Systems (ADS) or from particle reactions, such as the (α,n) radon-beryllium source using the α-particles emitted by radon and the ^{9}Be(α,n)^{12}C reactions, or the strontium-beryllium source based on the (γ,n) reaction ^{9}Be(γ,n)^{8}Be, or the ^{2}H(d,n)^{3}He, or ^{3}H(d,n)^{4}He sources using deuterium or tritium, the heavy isotopes of hydrogen.

In equation (2.46) the variables $\vec{r}$ and *t* were omitted, since they are the same in all quantities Ψ, Σ_s, Σ_a, and *S*. Actually it is usually assumed that Σ_s, Σ_a, and *S* are independent of *t*, as it can be very often assumed that even Ψ will be independent of *t*. Equation (2.46), which is the first form of Boltzmann's equation, can be used to evaluate the stationary distribution of Ψ, when the left side of the equation is zero, and can then be rewritten in the form:

$$\begin{aligned}
&\nabla\cdot\vec{\Omega}\Psi\left(\vec{r},E,\vec{\Omega}\right)+\Sigma_t\left(\vec{r},E\right)\Psi\left(\vec{r},E,\vec{\Omega}\right)\\
&\quad=\iint dE'd\vec{\Omega}\Sigma_s\left(\vec{r},E'\rightarrow E,\vec{\Omega}\cdot\vec{\Omega}'\right)\Psi\left(\vec{r},E',\vec{\Omega}'\right)\\
&\quad\quad+\frac{1}{k_{eff}}\iint dE'd\vec{\Omega}\chi\left(\vec{r},E'\rightarrow E\right)\nu\Sigma_f\left(\vec{r},E'\right)\Psi\left(\vec{r},E',\vec{\Omega}'\right)\\
&\quad\quad+Q\left(\vec{r},E,\vec{\Omega}\right)
\end{aligned}\tag{2.47}$$

Which is the time-independent form solved in TWODANT (see Chapter 3), and Σ_t is the total macroscopic cross section: $\Sigma_t=\left(\Sigma_a+\Sigma_s\right)$, Q is the rate at which particles are produced in the same element of phase space from sources that are independent of the flux Ψ, Σ_f is the fission cross section, ν is the number of particles emitted isotropically $(1/4\pi)$ per fission, and the fraction of these particles appearing in energy dE about E from fissions in dE' induced by neutrons about E' is $\chi\left(\vec{r},E'\rightarrow E\right)$. If Q is not zero in equation (2.47), then k_{eff} is set to 1; if Q is zero, then the problem is an eigenvalue problem and $1/k_{eff}$ is the eigenvalue. The integral:

$$\frac{1}{k_{eff}}\iint dE'd\vec{\Omega}'\chi\left(\vec{r},E'\rightarrow E\right)\nu\Sigma_f\left(\vec{r},E'\right)\Psi\left(\vec{r},E',\vec{\Omega}'\right)\tag{2.48}$$

accounts then for the fission sources[7], which are part of S in equation (2.46). The treatment of the discretization of this equation as employed in the solver modules will be explained in Chapter 3.

MONTE-CARLO

In the treatment of deterministic computational methods the computing errors are systematic. Aside from uncertainties in the cross section data, they arise not only from the discretization of the time-space-angle-energy phase space for numerical computations, but also from the fact that present state of the art does not, with rare exceptions, permit the full three-dimensional configurations in deterministic transport computations. Hence, the errors introduced by representing three-dimensional models by simplified one- or two-dimensional models are of paramount importance, and much of the effort in deterministic method development is directed

---

[7] The contribution of (n,2n) and (n,3n) processes is not described explicitly here, although they have to be taken into account when establishing a complete neutron balance.

toward the related problems of computer memory, time, and accuracy encountered in extending deterministic methods to treat large multidimensional problems. With complex internal structures, or irregular shaped internal or external surfaces of the material distribution, like in the SCFR, the use of a deterministic code might then introduce relevant systematic errors.

In contrast, Monte-Carlo, which is not a model itself, but rather a method to solve equations e.g. Equation (2.47), is capable of treating very complex three-dimensional configurations, and specifically to evaluate the shown integrals and hence obtain, for instance, the particle distribution in energy, space and direction, for any given geometry. The name of method derives from the statistical sampling technique, which reminds of games of chance, where randomness would statistically become resolved in predictable probabilities, therefore Monte-Carlo.

The Monte-Carlo method is a probabilistic method, which gives an estimate of the quantity of interest (reaction rates, scalar fluxes, etc.) calculating an average value for a finite number of histories or trajectories. The histories are randomly started and traced according to the elementary laws of physics, which determine the movement of neutrons and/or other particles. To accelerate to convergence of the estimation process it's possible to modify the physical laws and introduce a bias.

A good and simple way to introduce this method is to consider the calculation of an integral of the following type (for a comprehensive treatment of the method see Lewis (1984) /68/):

$$I = \int_D f(x)\, p(x)\, dx \tag{2.49}$$

where $p(x) \geq 0$ is normalized to 1, $N_p = \int_D p(x)\, dx = 1$. In order to apply the statistical method the x variable is chosen as an event in the space of events $D = \{x\}$, with a probability density $p(x)$; hence $f(x)$ is a function of the random variable, and the integral I is in fact the average value f of the function $f(x)$ in the domain *D*. It is then possible to use the probability density to build a sample of the set N, $\{x_1, x_2, ..., x_N\}$, and evaluate the estimation:

$$I \approx f_N = \frac{1}{N} \sum_{i=1}^{N} f(x_i) \tag{2.50}$$

The precision of this estimation, or the size of the sample necessary to obtain a certain precision, depends on the square root of the number of samples [Johnson (1992) /69/]:

$$\sigma_{f_N}^2 = \frac{\sigma_f^2}{N} \tag{2.51}$$

where σ_f is the standard deviation of the estimation and therefore the precision of the calculation depends on $1/\sqrt{N}$ for the same set.

Some of the constraints that were posed on $p(x)$ can be removed. Effectively, if $p(x)$ isn't positive everywhere, the integrated domain can be divided into sub-domains where p does not change sign within the integrated domain and to calculate the integral as the sum of integrals using Monte-Carlo. Furthermore, if p is not normalized to one, it is sufficient to consider the integral $1/N_p$, where N_p is the integral of p in the domain. The Monte-Carlo method can then be applied to calculate any kind of integral.

The advantage of this method is that the speed of convergence, $1/\sqrt{N}$, does not change with integration domain dimension. This aspect might not be so interesting in a one-dimensional case, but in considering multidimensional domains this method becomes rapidly competitive with the traditional (deterministic) methods. It is worth repeating that the speed of convergence of the trapezoid method in a one-dimensional case is $1/N^2$ and for a second order quadratic formula is $1/N^4$, but it decreases very rapidly with the number of dimensions in the domain to be integrated.

The correct application of this method requires the extraction of random numbers x_i starting from a known law of probability distribution $p(x)$, The sampling then depends on the form of $p(x)$ and on the appropriate sampling technique. Another problem is the dependence of the precision of a set N on the variance σ_f^2 for the studied population. As mentioned earlier, if the variance is too large, the sampling becomes too large and therefore impractical; it is then better to sample on a different population, which has the same mean value, but a much smaller variance. This technique is called biasing and is one of the fundamental techniques used to accelerate the convergence of a Monte-Carlo calculation.

In order to understand the method better, an example will be provided. The integral to be calculated is the following:

$$I = \int_{a}^{a+1} \frac{1}{2\sqrt{x}} dx \tag{2.52}$$

The exact value of the integral (2.52) is $\sqrt{a+1} - \sqrt{a}$. Taking as the law of probability distribution the function *p(x)=1* the estimation of the integral will be given by:

$$I \approx \frac{1}{N} \sum_{i=1}^{N} \frac{1}{2\sqrt{x_i}} \tag{2.53}$$

Where x_i are chosen from a uniform distribution in the interval (a, a+1), which is equivalent to $x_i = a + \xi_i$ with ξ_i sampled evenly within the interval (0, 1).

The statistical precision of the estimation depends on the variance:

$$\sigma_f^2 = \int_{a}^{a+1} \frac{dx}{4x} - I^2 = \frac{1}{4} \ln \frac{a+1}{a} - I^2 \tag{2.54}$$

For a<<1 the variance becomes very large, which would require a very large sampling in order to have an accurate evaluation of the integral. Moreover for a = 0 the variance is infinite and the Monte-Carlo method cannot be applied directly. In these cases biasing becomes an essential technique.

Biasing

In order to improve the efficiency of the sampling, that is, to reduce the variance, the states, particles, which contribute the most to the result, should be favored: that which exert a change in the probability law. Furthermore, since the aim is to calculate an integral, the function to be integrated should also be modified, in such a way as to keep the result unvaried. In simpler terms we are looking for $\tilde{f}$, $\tilde{p}$, and $\tilde{D}$ such that

$$I = \int_{D} f(x)\, p(x)\, dx = \int_{\tilde{D}} \tilde{f}(y)\, \tilde{p}(y)\, dy \tag{2.55}$$

and with the conditions

$$\sigma_{\tilde{f}}^2 = \int_{\tilde{D}} \left(\tilde{f}(y) - I \right)^2 \tilde{p}(y)\, dy < \sigma_f^2 = \int_{D} \left(f(x) - I \right)^2 p(x)\, dx \tag{2.56}$$

$$\tilde{p} \geq 0 \text{ within } \tilde{D} \text{ and } \int_{\tilde{D}} \tilde{p}(y)\,dy = 1 \tag{2.57}$$

Since the domain $\tilde{D}$ could have different dimensions than D, the general problem expressed by equation (2.55) could induce a great number of essentially different solutions. In order to avoid this, the solutions that will be considered will be limited to the case where the integration domains are identical, $\tilde{D} = D$ and, therefore,

$$f(x)\,p(x) = \tilde{f}(y)\,\tilde{p}(y) \tag{2.58}$$

This simplifying hypothesis implies:

$$I = \int_D w(x)\,f(x)\,\tilde{p}(x)\,dx \tag{2.59}$$

where w is the weight:

$$w(x) = \frac{p(x)}{\tilde{p}(x)} = \frac{\tilde{f}(x)}{f(x)} \tag{2.60}$$

The sampling will then be performed by applying the probability law $\tilde{p}(x)$ extracting a series of values $\{x_i, i = 1 \ldots N\}$, and accumulating for each value x_i with a weight $w(x_i)$:

$$I \approx \tilde{f}_N = \frac{1}{N}\sum_{i=1}^{N} w(x_i)\,f(x_i) \tag{2.61}$$

Expression (2.61) hence replaces equation (2.50). The sampling then occurs using a different probability law $\tilde{p}(x)$ and accumulating the set taking into account the weight w. It is remarkable that the events, which increase their probabilities, have a weight less than one, these events then happen more frequently, but give a smaller contribution to the set.

There is always a perfect solution to the biasing problem, which reduces the variance to zero; this solution is called sampling by importance. Imposing the conditions:

$$f^*(x) = I, \quad p^*(x) = \frac{f(x)\,p(x)}{I} \quad \rightarrow \quad w(x) = \frac{I}{f(x)} \tag{2.62}$$

it is possible, if f does not change sign (but it is always possible by dividing the domain D in subdomains where f does not change sign as previously explained), to easily verify that the variance becomes zero $\sigma^2_{f^*} = 0$, and consequently, with a simple estimation find the exact value of the integral, provided that the associated importance is known exactly.

It is clear that the sampling by importance is a utopia since in order to build the corresponding biased probability distribution, would require knowing the result one is attempting to estimate. The main interest in this kind of biasing is that is gives suggestions on how to achieve a good biasing. For instance if the value I_{approx} is available (calculated with a non biased sampling), it is possible to use the relations (2.62) to define a biasing. Moreover the expression for $p^*(x)$ needed for sampling by importance demonstrates that to improve the sampling one should increase the probability of the events x with $f(x)$ greater than the average value, $f(x) > I$, and decrease the probability of x with $f(x)$ smaller than the average value, $f(x) < I$:

$$p^*(x) = \frac{f(x)}{I} p(x), \quad w(x) = \frac{I}{f(x)} \quad \rightarrow \quad \begin{cases} f > I \rightarrow p^* > p \rightarrow w < 1 \\ f < I \rightarrow p^* < p \rightarrow w > 1 \end{cases} \tag{2.63}$$

The practical rule is therefore to increase the probability of the events, which contribute the most to the result, and, to decrease the probability of those, which contribute less. In any case one should keep in mind that the application of this "golden rule" can sometimes give the opposite result, to what one would expect and even increase the variance. In Monte-Carlo mastering bias techniques is very difficult and depends heavily on the specific problem and on the experience of the user. A good biasing is almost always the result of an exhaustive preliminary study of the problem.

Sampling by importance as shown in expression (2.62) suggests that the ideal probability distribution $p^*(x)$ is proportional to the product $f(x)p(x)$. From this consideration a second "golden rule" of biasing can be drawn, that is to approximate the product with an easily integrable function and which defines an easily sampled probability density function. A good example is the following integral:

$$I = \int_0^1 \cos\left(\frac{\pi x}{2}\right) dx \tag{2.64}$$

which has the exact value of $I = 2/\pi$. Using then the probability density function $p(x) = 1$ the variance is equal to $\sigma_{f^*}^2 = 0.0947$. Expanding the cosine just around x=0 (where it's more important) it is possible to write:

$$f(x)\,p(x) = \cos\left(\frac{\pi x}{2}\right) \approx 1 - \frac{\pi^2 x^2}{8} \tag{2.65}$$

One could then use as a probability density function $\tilde{p}(x) \approx 1 - \alpha x^2$ with α approaching $\pi^2/8$. Taking $\alpha = 1$ and normalizing $\tilde{p}(x)$ we find $\tilde{p}(x) = (3/2)(1 - x^2)$, which gives a variance of $\sigma_{\tilde{f}}^2 = 0.00099$, and thereby reducing the sampling set and variance by a factor of 100 times smaller than without biasing.

CHAPTER 3

NUMERICAL METHODS

Because of the variety of codes and techniques that were used in the analyses, a comprehensive treatment of the numerical solution schemes would go beyond the scope of this work, therefore, for a detailed description of the SIMMER-III code package, and the MCNP (or MCNP-X) the reader is referred to the available open literature (e.g.: Kondo (1992) /48/, Tobita (2000) /49/, Morita (1998) /52/, Urbatsch (1995) /70/, Brown (2004) /71/), and to the manuals (e.g.: Alcouffe (1995) /44/, Briesmeister (2000) /46/, Bohl (1990) /72/, MCNPX (2002) /73/). Nonetheless the general Monte-Carlo technique and the discrete ordinates method used in TWODANT will be illustrated in order to better understand the differences between a Monte-Carlo and a deterministic method.

For what concerns the fluid dynamics, no numerical solution schemes were adopted, since MXN is mostly based on direct analytical solutions. The only exception regards the calculation of the fuel conductivity, since it is based on a standard Newton-Raphson method [Abramowitz (1972) /74/], which will be therefore briefly explained.

A few paragraphs will then be spent to describe the coupling procedure that was implemented among the different utilized codes.

3.1 Neutronics

Monte-Carlo methods are very different from deterministic transport methods. Deterministic methods, the most common of which, after diffusion theory, is the discrete ordinates method, solve the transport equation for the average particle behavior. By contrast, MCNP (the Monte-Carlo code applied in this work) does not solve an explicit equation, but rather simulates individual particles recording some aspects (tallies) of their average behavior. The average behavior of particles in the physical system is then inferred (using the central limit theorem) from the average behavior of the simulated particles. Not only Monte-Carlo and deterministic methods are very different ways of solving a problem, even what constitutes a solution is different. Deterministic methods typically give fairly complete information (for example, flux) throughout the phase space of the problem. MCNP can supply information only about the specific tallies requested by the user.

Deterministic methods produce a unique numerical value (usually within specified convergence criteria of numerical iteration processes), but without any information on the accuracy or reliability of the result with respect to e.g. the chosen discretization of the 6-dimensional space. On the other hand, MCNP results are usually provided with an associated statistical uncertainty, so that an estimate of the reliability is possible (with a correlated confidence level). However, both deterministic and Monte-Carlo results rely on the accuracy of the nuclear data describing the neutron interaction with the materials of the reactor composition.

When Monte-Carlo and discrete ordinates methods are compared, it is often said that MCNP solves the integral transport equation, whereas discrete ordinates solves the integro-differential transport equation. Two things are misleading about this statement. Firstly, the integral and integro-differential transport equations are two different forms of the same equation; if one is solved, the other is solved also. Secondly, Monte-Carlo “solves” a transport problem by simulating particle histories rather than by solving an equation. No transport equation need ever be written to solve a transport problem applying the Monte-Carlo method. Nonetheless, an equation that describes the probability density of particles in phase space can be derived; this equation turns out to be the same as the integral transport equation.

Without deriving the integral transport equation, it is instructive to investigate why the discrete ordinates method is associated with the integro-differential equation and Monte-Carlo with the integral equation. The discrete ordinates method visualizes the phase space to be divided into many small boxes, and the particles move from one box to another. In the limit as the boxes get progressively smaller, particles moving from box to box take a differential amount of time to move a differential distance in space. In the limit this approaches the integro-differential transport equation, which has derivatives in space and time. By contrast, Monte-Carlo simulates particles between events (for example, collisions) that are separated in space and time. Neither differential space, nor time are inherent parameters of Monte-Carlo transport. The integral equation does not have time or space derivatives.

MCNP is well suited to solving complicated three-dimensional, time-dependent problems. Because the Monte-Carlo method does not use phase space boxes, there are no averaging approximations required in space, energy, and time. This is especially important in allowing detailed representation of all aspects of physical data.

The Monte-Carlo method

The Monte-Carlo method can be used to simulate a statistical process (such as the interaction of nuclear particles with materials) and is particularly useful for complex problems that cannot be modeled by computer codes that use deterministic methods. The individual probabilistic events that comprise a process are simulated sequentially. The probability distributions governing these events are statistically sampled to describe the total phenomenon, and the statistical sampling process is based on the selection of random numbers. In general, the number of trials necessary to adequately describe the phenomena is usually quite large. In particle transport, the Monte-Carlo technique is pre-eminently realistic (a theoretical experiment). It consists of actually following each of many particles from a source throughout its life to its end in some terminal category (absorption, escape, etc.). Probability distributions are randomly sampled using transport data to determine the outcome at each step of its life.

Figure 3.1 represents the random history of a neutron incident on a slab of material that can undergo fission. Numbers between 0 and 1 are selected randomly to determine what (if any) and where interaction takes place, based on the rules (physics) and probabilities (transport data) governing the processes and materials involved. In this particular example, a neutron collision occurs at event 1. The neutron is scattered in the direction shown, which is selected randomly from the physical scattering distribution. A photon is also produced and can be temporarily stored, or banked, for later analysis. At event 2, fission occurs, resulting in the termination of the incoming neutron and the birth of two outgoing neutrons and one photon. One neutron and the photon are banked for later analysis. The first fission neutron is captured at event 3 and terminated. The banked neutron is now retrieved and, by random sampling, leaks out of the slab at event 4. The fission-produced photon has a collision at event 5 and leaks out at event 6. The remaining photon generated at event 1 is now followed with a capture at event 7. Note that MCNP retrieves banked particles such that the last particle stored in the bank is the first particle taken out. This neutron history is now complete. As more and more such histories are followed, the neutron and photon distributions and the associated events become better known. The quantities of interest (whatever the user requests) are tallied, along with estimates of the statistical precision (uncertainty) of the results.

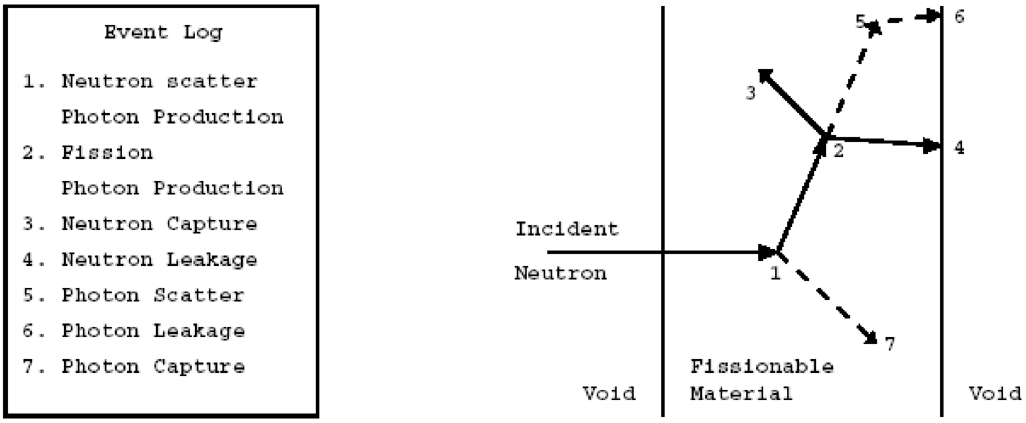

Figure 3.1: The Monte-Carlo method /46/

Calculation of k-effective

Chapter 2 and the previous paragraphs gave an overview on how a Monte-Carlo code works; now, it is of interest to explain with some more detail the procedure used in MCNP4C to calculate k-effective.

Nuclear criticality, the ability to sustain a chain reaction by fission neutrons, is characterized by k-effective, the eigenvalue to the neutron transport equation. In reactor theory, k-effective is thought of as the ratio between the number of neutrons in successive generations, with the fission process regarded as the birth event that separates generations of neutrons. For critical systems, $k_{eff} = 1$ and the chain reaction will just sustain itself. For subcritical systems, $k_{eff} < 1$ and the chain reaction will not sustain itself. For supercritical systems, $k_{eff} > 1$ and the number of fissions in the chain reaction will increase with time. Therefore in order to determine the dynamic behavior of the SCFR an accurate estimation of the reactivity coefficients is of extreme importance[8].

Since we are dealing with a pressurized water-cooled system, the void reactivity coefficient was extensively studied in this work. In order to estimate the void reactivity worth ρ_v, k-effective in reactor nominal conditions and in voided conditions need to be calculated:

$$\rho_v = \frac{k_{nc} - k_{void}}{k_{nc} \cdot k_{void}} \tag{3.1}$$

Calculating k-effective consists of estimating the mean number of fission neutrons produced in one generation per fission neutron started. A generation is the life of a neutron from the origin in fission to the end by escape, parasitic capture, or absorption leading to fission. In MCNP, the computational equivalent of a fission generation is a k-effective cycle; i.e. a cycle is a computed estimate of an actual fission generation. Processes such as (n,2n) and (n,3n) are considered internal to a cycle and do not act as termination. Because fission neutrons are terminated in each cycle to provide the fission source for the next cycle, a single history can be viewed as continuing from cycle to cycle. The effect of the delayed neutrons is included using the total number of neutron generated per fission and their relative spectrum.

It is imperative to emphasize that the result from a criticality calculation is a confidence interval for k-effective that is formed using the final estimated k-effective and the estimated standard deviation.

A properly formed confidence interval from a valid calculation should include the true answer. There will always be some probability that the true answer lies outside of a confidence interval.

The definition of k-effective is:

$$k_{eff} = \frac{\text{fission neutrons in generation } i+1}{\text{fission neutrons in generation } i} \tag{3.2}$$

Which is equal to:

---

[8] Reactivity coefficients give the amount of reactivity change for a given variation in one of the physical parameters of the reactor (i.e.: status of fuel depletion, temperature, pressure, build-up of neutron poisons), where the amount of reactivity (ρ) in a reactor core determines what the neutron population is, and consequently the reactor power (see also Equation (3.1)).

$$k_{eff} = \frac{\rho_a \int_V \int_0^\infty \int_E \int_\Omega \nu \sigma_f \Phi dV\,dt\,dE\,d\Omega}{\int_V \int_0^\infty \int_E \int_\Omega \nabla \cdot J\,dV\,dt\,dE\,d\Omega + \rho_a \int_V \int_0^\infty \int_E \int_\Omega \left(\sigma_c + \sigma_f + \sigma_m\right) \Phi dV\,dt\,dE\,d\Omega} \tag{3.3}$$

where the phase-space variables are *t*, *E*, and *Ω* for time, energy, direction, and implicitly *r* for position with incremental volume *dV* around *r*. The denominator is the loss rate, which is the sum of leakage, capture (n,0n), fission, and multiplicity (n,xn) terms. The above definition of k-effective comes directly from the time-integrated Boltzmann transport equation (without external sources), where elastic processes can be omitted, since the number of neutrons remains constant when a neutron undergoes such a process.

In order to determine, using a Monte-Carlo technique, the values of the shown integrals, a set of estimators needs to be used, specifically a collision estimator, an absorption estimator and a track length estimator.

An estimator is a specific function of the random samples, of a random variable, that statistically represents a true unknown mean. If *x* is a random variable with an associated distribution and an unknown mean, then the function $X(x_1, x_2, x_3, \ldots, x_n)$ is an estimator of the unknown mean. The set $\{x_1, x_2, x_3, \ldots, x_n\}$ consists of *n* independent random samples selected from the probability density distribution of *x*. A good estimator should be unbiased, consistent, and efficient. An estimator is unbiased if its expected value equals the true mean, μ, i.e.:

$$E\left(X\right) = \mu \tag{3.4}$$

for all X. An estimator is consistent if it approaches, in a statistical sense, the true mean, as *n* gets larger. An efficient estimator is the one, among a group of unbiased estimators, that produces the minimum variance for a given sample size *n*. Mathematical expression for each of the three estimators of k-effective are given here. The superscripts '*c*', '*a*' and '*tl*' will be used for the collision, absorption and track length estimators respectively.

Collision Estimator:

The collision estimate for k-effective for any active cycle is:

$$k_{eff}^{c} = \frac{1}{N} \sum_i w_i \left[\frac{\sum_k f_k \bar{\nu}_k \sigma_{f_k}}{\sum_k f_k \sigma_{T_k}} \right] \tag{3.5}$$

Where i is summed over all collisions in a cycle where fission is possible;

k is summed over all nuclides of the material involved in the i^{th} collision;

σ_{T_k} is the total microscopic cross section;

σ_{f_k} is the microscopic fission cross section;

$\bar{\nu}_k$ is the average number of prompt or total neutrons produced per fission by the collision nuclide at the incident energy;

f_k is the atomic fraction for nuclide k;

N is the nominal source size for a cycle; and

w_i is the weight of particle entering collision.

Because w_i represents the number of neutrons entering the i^{th} collision:

$$w_i\left[\frac{\sum_k f_k\bar{\nu}_k\sigma_{f_k}}{\sum_k f_k\sigma_{T_k}}\right] \tag{3.6}$$

is the expected number of neutrons to be produced from all fission processes in the collision. Thus k_{eff}^{c} is the mean number of fission neutrons produced per cycle. The collision estimator tends to be best, sometimes only marginally so, in very large systems, such as a reactor core.

Absorption Estimator:

The absorption estimator for k-effective for any active cycle is made when a neutron interacts with a fissionable nuclide. The estimator differs for analog and implicit capture. For analog capture:

$$\left(k_{eff}^{a}\right)_{an} = \frac{1}{N}\sum_i w_i\bar{\nu}_k \frac{\sigma_{f_k}}{\sigma_{c_k}+\sigma_{f_k}} \tag{3.7}$$

where i is summed over each analog capture event in the k^{th} nuclide. Note that in analog capture, the weight is the same both before and after the collision. Because analog capture includes fission in criticality calculations, the frequency of analog capture at each collision with nuclide k is $\left(\sigma_{c_k}+\sigma_{f_k}\right)/\sigma_{T_k}$. The analog absorption k-effective estimate is very similar to the collision estimator of k-effective except that only the k^{th} absorbing nuclide, as sampled in the collision, is used rather than averaging over all nuclides.

For implicit capture, the following is accumulated:

$$\left(k_{eff}^{a}\right)_{im}=\frac{1}{N}\sum_{i} w_i' \,\bar{\nu}_k \frac{\sigma_{f_k}}{\sigma_{c_k}+\sigma_{f_k}} \tag{3.8}$$

where i is summed over all collisions in which fission is possible and $w_i'=w_i\left(\sigma_{c_k}+\sigma_{f_k}\right)/\sigma_{T_k}$ is the weight absorbed in the implicit capture. The difference between the implicit absorption estimator k_{eff}^{a} and the collision estimator k_{eff}^{c} is that only the nuclide involved in the collision is used for the absorption k-effective estimate rather than an average of all nuclides in the material for the collision k-effective estimator.

The absorption estimator with analog capture is likely to produce the smallest statistical uncertainty of the three for systems where the ratio $\bar{\nu}_k\sigma_{f_k}/\left(\sigma_{c_k}+\sigma_{f_k}\right)$ is nearly constant. Such would be the case for a thermal system with a dominant fissile nuclide such that the 1/velocity cross section variation would tend to cancel.

The absorption estimate differs from the collision estimate in that the collision estimate is based upon the expected value at each collision, whereas the absorption estimate is based upon the events actually sampled at a collision. Thus all collisions will contribute to the collision estimate k_{eff}^{c} of and by the probability of fission in the material. Contributions to the absorption estimator will only occur if an actual fission event occurs for the sampled nuclide in the case of analog capture. For implicit capture, the contribution to the absorption estimate will only be made for the nuclide sampled.

Track Length Estimators

The track length estimator of k-effective is accumulated every time the neutron traverses a distance d in a fissionable material cell:

$$k_{eff}^{tl}=\frac{1}{N}\sum_{i} w_i N d \sum_{k} f_k \bar{\nu}_k \sigma_{f_k} \tag{3.9}$$

where i is summed over all neutron trajectories,

N is the atomic density in the cell, and

d is the trajectory track length from the last event.

Because $Nd\sum_k f_k \bar{\nu}_k \sigma_{f_k}$ is the expected number of fission neutrons produced along trajectory *d*, k_{eff}^{tl} is a third estimate of the mean number of fission neutrons produced in a cycle per nominal fission source neutron.

The track length estimator tends to display the lowest variance for optically thin fuel cells (e.g. plates) and fast systems where large cross–section variations because of resonances may cause high variances in the other two estimators.

In criticality calculations at the end of each cycle (or fission generations) an estimate of k-effective is produced by each of these three estimators. The final k-effective estimator of each type is the average over many cycles of the k-effective estimates. A combination of the three estimators is the best k-effective estimate available [Urbatsch (1995) /70/]. It should be once again emphasized that for Monte-Carlo criticality calculations, the final result is not a point estimate of k-effective, but rather a confidence interval.

Multigroup, discrete ordinates method

Equation (2.47) describes the time-independent inhomogeneous first order form of the Boltzmann transport equation. In order to solve this equation energy, angular, and spatial variable discretization is to be performed, unless as discussed earlier a Monte-Carlo method is used.

The first approximation that will be described is the multigroup approximation; that is in the energy variable, the energy domain is partitioned into *G* intervals of width $\Delta E_g = E_{g-1/2} - E_{g+1/2}$. By convention, the highest energy is at $E_{1/2}$ and hence the index *g* increases as energy decreases (since the normal transport of particles in energy is from high to low energy as they collide with nuclei in the medium). Thus, if Equation (2.47) is integrated over each energy interval, the following discretized equation is obtained:

$$\begin{aligned}\vec{\Omega}\cdot\nabla\psi_g\left(\vec{r},\vec{\Omega}\right)+\sigma_{t,g}\left(\vec{r}\right)\psi_g\left(\vec{r},\vec{\Omega}\right)&=\frac{\chi_g\left(\vec{r}\right)}{k_{eff}}\Phi\left(\vec{r}\right)+Q_g\left(\vec{r},\vec{\Omega}\right)\\&+\sum_{g'=1}^{G}\int\sigma_{s,g'\to g}\left(\vec{r},\mu_0\right)\psi_{g'}\left(\vec{r},\vec{\Omega}'\right)d\vec{\Omega}';\quad g=1,\ldots,G\end{aligned}\tag{3.10}$$

where: $\mu_0 = \vec{\Omega}\cdot\vec{\Omega}'$,

$$\psi_g\left(\vec{r},\vec{\Omega}\right)=\int_{\Delta E_g}\Psi\left(\vec{r},\vec{\Omega},E\right)dE\ ,$$

$$\sigma_{t,g}\left(\vec{r}\right)=\left(\int_{\Delta E_g}\sigma_t\left(\vec{r},E\right)\psi\left(\vec{r},\vec{\Omega},E\right)dE\right)/\psi_g\left(\vec{r},\vec{\Omega}\right),$$

$$\sigma_{s,g'\to g}\left(\vec{r},\mu_0\right)=\left(\int_{\Delta E_g}\int_{\Delta E_{g'}}\sigma\left(\vec{r},E'\to E,\mu_0\right)\psi\left(\vec{r},\vec{\Omega},E'\right)dEdE'\right)/\psi_{g'}\left(\vec{r},\vec{\Omega}\right),$$

$$Q_g\left(\vec{r},\vec{\Omega}\right)=\int_{\Delta E_g}Q\left(\vec{r},\vec{\Omega},E\right)dE\ ,$$

$$\chi_g\left(\vec{r}\right)=\int_{\Delta E_g}\chi\left(\vec{r},E\right)dE\ ,$$

$$\Phi\left(\vec{r}\right)=\sum_{g=1}^{G}\int_{\Delta E_g}\nu\sigma_f\left(\vec{r},E\right)\phi\left(\vec{r},E\right)dE\ ,$$

$$\phi_g\left(\vec{r}\right)=\int\psi_g\left(\vec{r},\vec{\Omega}\right)d\vec{\Omega}\,.$$

Note that the definition of the multigroup cross section is a formal one since one would need to know the solution of the transport problem in order to evaluate them. In practice the multigroup cross sections are supplied from a cross-section processing code, which predefines the energy intervals and the weighting functions. Note also that much of the physics of the problem is contained in the cross-section set and hence this aspect of the solution process should not be minimized. That is a careful selection of the cross-section set should be made in order to ensure a physically accurate solution. For few groups, this accuracy is heavily dependent upon the weighting function; as the number of groups increases, this becomes less so assuming a proper treatment of the resonance region.

As it will be discussed in detail in Chapter 4, this problem is rather significant in the case of the SCFR and since MCNP is based on continuous energy cross sections, that is no group approximation is necessary, it provides a significant advantage in the accuracy of the calculation's result.

Discrete Ordinates approximation

The next discretization involves the angular variable. In the method of discrete ordinates, the angle is discretized over the unit sphere in a prescribed manner. The choice of the discretization seeks to satisfy the following conditions:

1. physical symmetries are preserved upon discretization;
2. spherical harmonics moments are well approximated in order to provide an accurate representation of the source terms;
3. derivatives with respect to the angle coordinates that come from the streaming operator are simply approximated;
4. for special purposes, e.g. a problem with an incident neutron beam, or a configuration with an outward directed neutron guide tube, more angular direction vectors are attributed to a certain angular domain of particular importance or interest.

Since in multidimensional cases not all of the above conditions can be simultaneously satisfied completely, compromises are made in defining discrete ordinates sets. Basically each discrete ordinate is depicted as an angular direction vector, $\vec{\Omega}_m$, with an associated area on the unit sphere, the so-called angular weight w_m, where $m=1, \ldots, M$, M being the number of discrete ordinates. This M is derived from the S_n order specified by the user (in normal TWODANT applications a 4th order is chosen), and depends upon the set arrangement chosen and the number of spatial dimensions. All of the discrete ordinates sets used in the solver modules satisfy certain, fundamental conditions including $\sum_{m=1}^{M} w_m = 4\pi$ for conservation. The requirements that $\sum_{m=1}^{M} w_m \vec{\Omega}_m = 0$ for symmetry, and $\sum_{m=1}^{M} w_m \mu_m^2 = \sum_{m=1}^{M} w_m \eta_m^2 = \sum_{m=1}^{M} w_m \xi_m^2 = \frac{1}{3}$ for the diffusion limit[9] are also imposed, where the components of $\vec{\Omega}_m$ are: $\vec{\Omega}_m = \mu_m \vec{i} + \eta_m \vec{j} + \xi_m \vec{k}$ [10]. To obtain the discrete ordinates balance equation, assuming for simplicity isotropic scattering, we integrate Equation (3.10) over w_m and obtain:

---

[9] The diffusion limit is equal to 1/3 since no spatial direction is preferred, and therefore the diffusion constant is averaged over the three directions *i*, *j*, and *k*.

[10] The very desirable property $w_M \geq 0$ cannot be fulfilled for high values of M for some of the various quadrature sets described in literature.

$$\begin{aligned}&\left[\vec{\Omega}\cdot\nabla\psi_g\left(\vec{r},\vec{\Omega}\right)\right]_m+\sigma_{t,g}\left(\vec{r}\right)\psi_{g,m}\left(\vec{r}\right)=\frac{\chi_g\left(\vec{r}\right)}{k_{eff}}\Phi\left(\vec{r}\right)+Q_{g,m}\left(\vec{r}\right)\\&\quad+\sum_{g'=1}^{G}\sigma_{s0,g'\rightarrow g}\left(\vec{r}\right)\phi_{g'}\left(\vec{r}\right)\end{aligned}\tag{3.11}$$

where:

$$\psi_{g,m}\left(\vec{r}\right)=\int_{w_m}\psi\left(\vec{r},\vec{\Omega}\right)d\vec{\Omega},$$

$$\phi_g\left(\vec{r}\right)=\sum_{m=1}^{M}w_m\psi_{g,m}\left(\vec{r}\right),$$

$$Q_{g,m}\left(\vec{r}\right)=\sum_{l=0}^{L}\sum_{q=-l}^{l}\left(2l+1\right)Y_l^q\left(\vec{\Omega}_m\right)Q_{g,l}^q\left(\vec{r}\right),$$

$$Q_{g,l}^q\left(\vec{r}\right)=\int Y_l^q\left(\vec{\Omega}\right)Q_g\left(\vec{r},\vec{\Omega}\right)d\vec{\Omega},$$

and $Y_l^q\left(\vec{\Omega}\right)$ are the spherical harmonic functions[11].

Note that the streaming operator (the operator which takes into account the direction component: $\vec{\Omega}\cdot\nabla\psi_g$) is only discretized symbolically. The specific form of this operator depends upon the geometric symmetry chosen and to some extent upon the spatial discretization method and the angular quadrature set. Note also that the source was expanded in spherical harmonics, the form in which TWODANT expects the angular dependence of the source to be represented if it is a volume source.

Spatial discretization

The geometries treated in TWODANT are planar X-Y, and polar R-Θ, and cylindrical R-Z, the latter being the most commonly used for reactor applications[12]. In cylindrical geometry, the angular flux is assumed symmetric about the μ-ξ (or $\phi = 0° - 180°$) plane. Thus, only one-fourth of the unit sphere needs to be considered in the angular dependence, and therefore the transport operator becomes:

---

[11] The spherical harmonics $Y_l^q\left(\vec{\Omega}\right)$ are the angular portion of the solution to Laplace's equation $\left(\nabla^2\psi=0\right)$ in spherical coordinates where azimuthal symmetry is not present [MacRobert (1967) /75/].

[12] It may be worth mentioning that there does also exist a three-dimensional version of the code called THREEDANT, currently implemented in SIMMER-IV.

$$\vec{\Omega}_m \cdot \nabla \psi_m = \frac{\mu_m}{r}\frac{\partial}{\partial r}\left(r\psi_m\right) - \frac{1}{r}\frac{\partial}{\partial \varphi}\left(\eta_m \psi_m\right) + \xi_m \frac{\partial \psi_m}{\partial z} \tag{3.12}$$

where, as indicated before ($\hat{e}_r$, and $\hat{e}_z$ being the axis vectors):

$\mu_m = \hat{e}_r \cdot \vec{\Omega}_m$,

$\xi_m = \hat{e}_z \cdot \vec{\Omega}_m$,

The spatially discretized equations for all the symmetries can be written as a balance equation in a single form. The balance equation is derived by integrating the above equations over a spatial mesh cell.

$$\begin{aligned}
&\mu_m \left(A_{i+1/2,j}\psi_{g,m,i+1/2,j} - A_{i-1/2,j}\psi_{g,m,i-1/2,j} \right) + \\
&\quad + \eta_m B_{i,j} \left(\psi_{g,m,i,j+1/2} - \psi_{g,m,i,j-1/2} \right) + \\
&\quad + \left(A_{i+1/2,j} - A_{i-1/2,j} \right) \frac{\left(\alpha_{m+1/2}\psi_{g,m+1/2,i,j} - \alpha_{m-1/2}\psi_{g,m-1/2,i,j} \right)}{w_m} + \\
&\quad + \alpha_{t,g,i,j} V_{i,j} \psi_{g,m,i,j} = S_{g,m,i,j} V_{i,j}
\end{aligned} \tag{3.13}$$

where:

$\psi_{g,m,i+1/2,j}$ is the flux on the right edge of the mesh cell,

$\psi_{g,m,i,j+1/2}$ is the flux on the top edge of the mesh cell,

$\psi_{g,m+1/2,i,j}$ is the angular direction edge flux,

$\psi_{g,m,i,j}$ is the cell center angular flux,

$A_{i+1/2,j}$ is the mesh cell area in the i coordinate direction,

$B_{i,j}$ is the mesh cell area in the j coordinate direction, and

$V_{i,j}$ is the mesh cell volume.

Equation (3.13) represents IT*JT*MM equations for 4* IT*JT*MM+(IT+JT)*MM+IT*JT unknowns for each group. The boundary conditions give an additional IT*JT+(IT+JT)*MM equations. As implemented in TWODANT, we generate the remainder of the equations by one of two approximations: diamond differencing with set-to-zero fixup or adaptive weighted diamond differencing[13]. In the diamond case, we specify a relationship between the cell centered and cell edge fluxes in the following way:

$$\begin{aligned}
\psi_{g,m,i,j} &= 0.5\left(\psi_{g,m,i+1/2,j} + \psi_{g,m,i-1/2,j}\right)\\
\psi_{g,m,i,j} &= 0.5\left(\psi_{g,m,i,j+1/2} + \psi_{g,m,i,j-1/2}\right)\\
\psi_{g,m,i,j} &= 0.5\left(\psi_{g,m+1/2,i,j} + \psi_{g,m-1/2,i,j}\right)\\
m &= 1,\ldots,MM;\; i = 1,\ldots,IT;\; j = 1,\ldots,JT
\end{aligned} \tag{3.14}$$

These equations give 3*IT*JT*MM relationships needed to solve the discretized transport equation. The solution process starts from a known boundary condition, which specifies the edge flux at that boundary and follows the particle flow; equations (3.14) are used to eliminate the unknown edge flux in terms of the known edge and cell centered fluxes. This is then substituted into equation (3.13) to derive an equation for the cell-centered flux. Equation (3.14) is then used to compute the value for the unknown edge flux from the cell centered and the known edge fluxes. However, as in the one-dimensional case, the value for the edge flux can extrapolate to a negative value and so a fixup is employed. This negative flux fixup sets the unknown edge flux to zero if it extrapolates negative, and the balance equation (3.13), is resolved under this condition to maintain particle balance.

3.2 Fluid-dynamics and coupling procedures

The Newton-Raphson method

The Newton-Raphson method is a well-known root-finding algorithm, which uses the first few terms of the Taylor series of a function *f(x)* in the vicinity of a suspected root to zero in on the root [Abramowitz (1972) /74/]. The Taylor series of *f(x)* about the point $x = x_0 + \varepsilon$ is given by

$$f\left(x_0 + \varepsilon\right) = f\left(x_0\right) + f'\left(x_0\right)\varepsilon + \frac{1}{2} f''\left(x_0\right)\varepsilon^2 + \ldots \tag{3.15}$$

Which becomes

$$f\left(x_0 + \varepsilon\right) \approx f\left(x_0\right) + f'\left(x_0\right)\varepsilon\,. \tag{3.16}$$

---

[13] This latter approximation is no longer available as calculation option in SIMMER.

keeping terms only to first order. This expression can be used to estimate the amount of offset ε_0 needed to land closer to the root starting from an initial guess x_0. Setting $f\left(x_0+\varepsilon\right)=0$ and solving (3.16)for $\varepsilon \equiv \varepsilon_0$ gives:

$$\varepsilon_0=\frac{f\left(x_0\right)}{f'\left(x_0\right)}, \tag{3.17}$$

which is the first-order adjustment to the root's position. By letting $x_1=x_0+\varepsilon_0$, calculating a new ε_1, and so on, the process can be repeated until it converges to a root using

$$\varepsilon_n=\frac{f\left(x_n\right)}{f'\left(x_n\right)}, \tag{3.18}$$

Unfortunately, this procedure can be unstable near a horizontal asymptote or a local extremum. However, with a good initial choice of the root's position, the algorithm can by applied iteratively to obtain

$$x_{n+1}=x_n-\frac{f\left(x_n\right)}{f'\left(x_n\right)}, \tag{3.19}$$

for $n = 1, 2, 3, \ldots$. An initial point x_0 that provides safe convergence of Newton's method is called an approximate zero.

As shown then this method proves to be rather straightforward and it is accurate and fast enough to solve the simple implicit expression (2.38). The error of the method $\left(\varepsilon_{n+1}\right)$ can be determined too and after the $\left(n+1\right)^{st}$ iteration is given by

$$\varepsilon_{n+1}=\varepsilon_n-\frac{f\left(x_n\right)}{f'\left(x_n\right)}, \tag{3.20}$$

But

$$\begin{aligned} f\left(x_n\right) &= f\left(x_{n-1}\right)+f'\left(x_{n-1}\right)\varepsilon_n+\frac{1}{2}f''\left(x_{n-1}\right)\varepsilon_n^2+\ldots \\ &= f'\left(x_{n-1}\right)\varepsilon_n+\frac{1}{2}f''\left(x_{n-1}\right)\varepsilon_n^2+\ldots \end{aligned} \tag{3.21}$$

$$f'\left(x_n\right)=f'\left(x_{n-1}\right)+f''\left(x_{n-1}\right)\varepsilon_n+\ldots \tag{3.22}$$

so

$$\frac{f(x_n)}{f'(x_n)} = \frac{f'(x_{n-1})\varepsilon_n + \frac{1}{2}f''(x_{n-1})\varepsilon_n^2 + \ldots}{f'(x_{n-1}) + f''(x_{n-1})\varepsilon_n + \ldots} \tag{3.23}$$

and (3.20) becomes

$$\varepsilon_{n+1} = \varepsilon_n - \left[\varepsilon_n + \frac{f''(x_{n-1})}{2f'(x_{n-1})}\varepsilon_n^2\right] = \frac{f''(x_{n-1})}{2f'(x_{n-1})}\varepsilon_n^2 \tag{3.24}$$

Therefore, when the method converges, it does so quadratically.

The Coupling Procedure

The codes and the methods that have been illustrated in Chapter 2 and in the last paragraphs were chosen to be applied in this work in order to evaluate the reactivity response of the SCFR in case of coolant voiding.

The SCFR presents a few peculiar and specific characteristics that suggest the need for detailed and dedicated tools of analysis. The first and most evident aspect is the geometrical arrangement and configuration of the subassemblies, which give the core a significant heterogeneity (see Figure 2.1: Axial section of the SCFR core). A second aspect is the different geometry of the pins in the different areas of the core. Neglecting the configuration of the control rods, which was not considered in this study except for a few preliminary investigations, there are three different pin configurations in this reactor: the fuel pin, which has a standard cylindrical geometry (Figure 3.2), the blanket pin, where the coolant flows inside a channel located at the center of the pin itself (Figure 3.3), and finally the solid moderator pin, which is a solid metallic hexagon (Figure 3.4). What all the pins have in common is the hexagonal lattice arrangement and the dimensions of the hexagonal cells.

This particular configuration of the core gives way to very localized effects, which are very difficult to analyze using a standard deterministic code. Deterministic codes like TWODANT are usually based on pre-determined cell configurations, and therefore one is bound to approximate the geometry and homogenize the different regions of the reactor losing the detail of effects that, although confined in a small area, have influence on the overall core dynamics. Examples of this will be given in Chapter 4.

Although it is true that through a multi tier progressive homogenization it would be possible to take into account these local effects even with a deterministic code, the flexibility, the capabilities and the straightforwardness of Monte-Carlo, and specifically of MCNP, seem to be a winning argument to establish a Monte-Carlo based investigation procedure of the relevant neutronics phenomena of the SCFR.

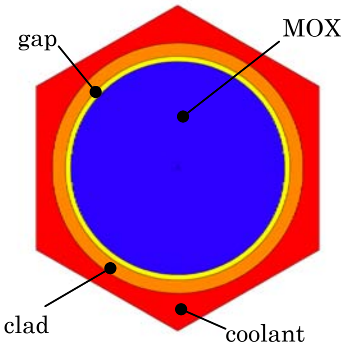

Figure 3.2: Seed fuel pin

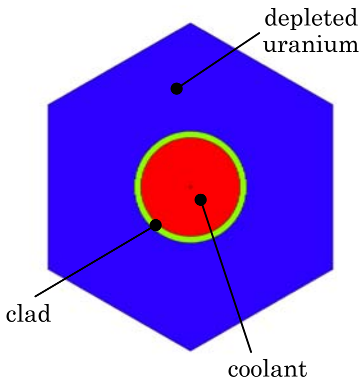

Figure 3.3: Blanket pin

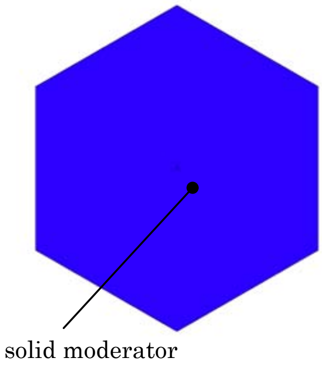

Figure 3.4: $ZrH_{1.7}$ pin

There are other aspects of this reactor that lead us not only to choose MCNP, but also to couple it with a fluid-dynamics code.

Because of the properties of supercritical water, the density gradient along the active core axis is very large (the ratio between the core inlet and outlet coolant density is of about nine). This feature, together with the tight pin arrangement (the pitch over diameter ratio is equal to 1.127[14]), implies a relevant neutron spectrum shift from almost thermal to epithermal to fast along the vertical axis. Moreover, the non-uniform subassembly radial arrangement changes the characteristic spectrum not only axially but also radially, since the depleted uranium loaded blanket areas are producing only a small amount of fission neutrons and will probably be relatively cold and cooled by a high-density fluid. Additionally, once the reactor is voided e.g. after the occurrence of a LOCA, the spectrum will be shifted to the fast region in the whole core, except in the proximity of the solid moderator pins. It is then clear that developing a group wise cross section set for a detailed representation of these phenomena taking into account spatial and energetic resonance self-shielding would be extremely difficult, unless a large number of groups were used and therefore, once again the choice of MCNP seemed the most appropriate for a correct representation of this reactor.

Finally, in order to approximate with a reasonable accuracy the fuel temperature distribution and the coolant density distribution in nominal conditions, which are

---

[14] Typical values for LWRs p/d are 1.32 for BWRs and 1.326 for PWRs /76/, /77/.

needed to determine the initial k-effective of the reactor, MCNP was coupled with MXN, the simple fluid-dynamics code described in Chapter 2.

The coupling scheme is shown in Figure 3.5.

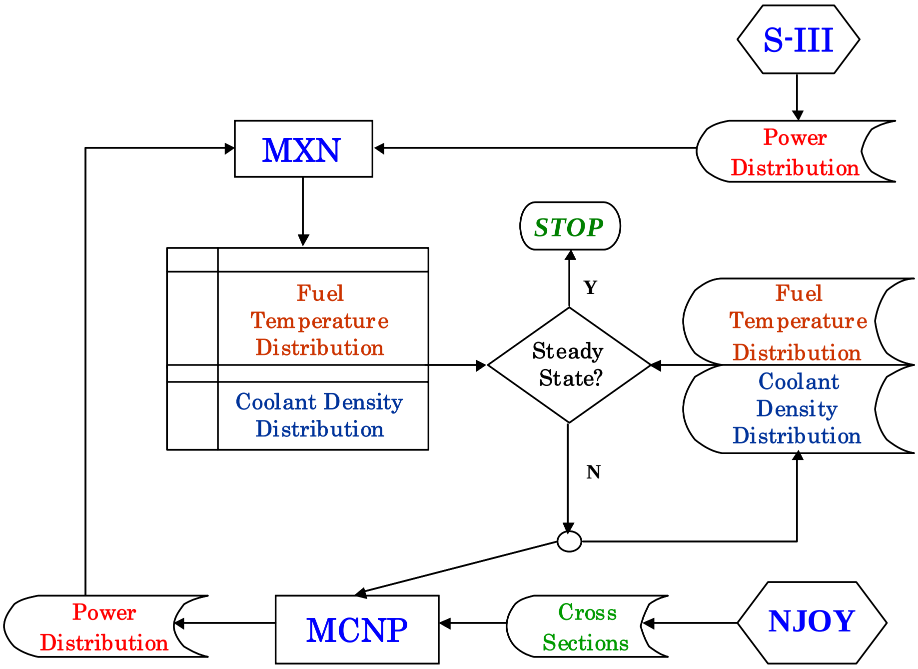

Figure 3.5: Flowchart of the coupled calculations

The iteration between MCNP and MXN (the fluid-dynamics subroutine) starts with the calculation of a first guess power distribution obtained with SIMMER-III, which includes TWODANT. This calculation is rather lengthy and its result is hindered by the drawbacks mentioned earlier (this simulation took to more than a week of calculation time on a Pentium 4® 2.4 GHz CPU PC). Therefore the power distribution is soon introduced in MXN where temperature and density distributions of the coolant are calculated and subsequently introduced in a detailed 3D Monte-Carlo model of the core, which will be described extensively in Chapter 4. MCNP then recalculates the power distribution, which is introduced in MXN. This last procedure is then iterated until convergence is reached.

Special attention is dedicated to the cross section sets. As fuel temperature changes its cross sections change and while this process is properly modeled in deterministic codes, which take into account for instance the Doppler broadening, in MCNP a new file is needed for each temperature. For this reason NJOY was applied in order to calculate temperature dependent cross section files for the nuclides involved in the calculations. This procedure, although accurate, requires the intensive use of computational resources. For instance the definition of the MOX fuel for a single temperature requires eight files and about sixty megabytes of disk space. Therefore, in order to reduce the computational effort, the temperatures of the cross sections were rounded off to the closest hundred degrees, in this way a maximum error of the temperature accounted for in MCNP is of 50 K, while the average error is of 25 K, limiting the amount of files and the computer memory allocated for a single calculation.

Another important approximation, besides the choice of the number of axial cells used to model the fuel pins, regards both the MCNP model and the fluid-dynamics geometry: that is the channel approximation. Although MCNP can provide extremely detailed information about the distribution of several neutronics parameters (e.g.: fission power, gamma heating, fluxes and currents) it was decided to calculate the power distribution coherently with the approximation level of the fluid dynamics routine. In other words, power was calculated as an integral of the power released in all the cells, which belong to the same channel e.g. the first seed region, hence losing the subchannel detail.

The channels in which the core was subdivived are shown in Figure 3.6, while Figure 3.7 shows a detail of RZ section of the MCNP core geometry between blanket 1 and seed 1, where it is possible to distinguish the zirconium hydride layer at the edge of the blanket and the non-uniform axial subdivision of the seed in 22 cells (20 for the plutonium enriched fuel and 2 for the axial blankets. The non-uniformity of the axial mesh size is a result of the choice to evenly follow the axial distribution of the fuel enrichment, which is also non-uniform.

Another approximation regards the decoupling in the fluid dynamics model of the axial and radial power distribution represented as described in Chapter 2 by the function $\chi(r,z)=\chi_m\chi_r(r)\chi_z(z)$, where $\chi_r(r)$ and $\chi_z(z)$ are normalized distribution functions, and χ_m is the amplitude. Radial heat transfer was also neglected. In addition to this, the table of the supercritical water properties has a temperature interval of 1 K, which corresponds to an average density error of ~1.5 kg/m^3, and a maximum error in the considered temperature range [453.15 ÷ 1073.15 K] of ~ 5 kg/m^3.

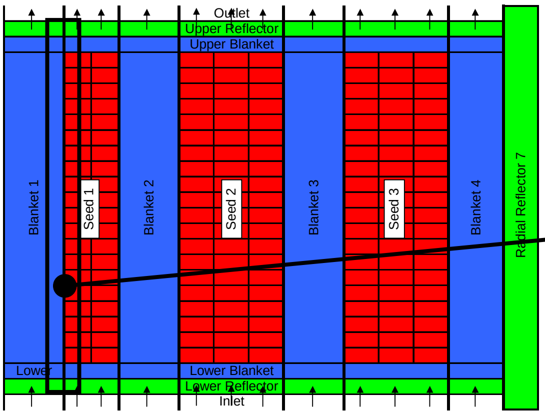

Figure 3.6: Core fluid dynamics: channels

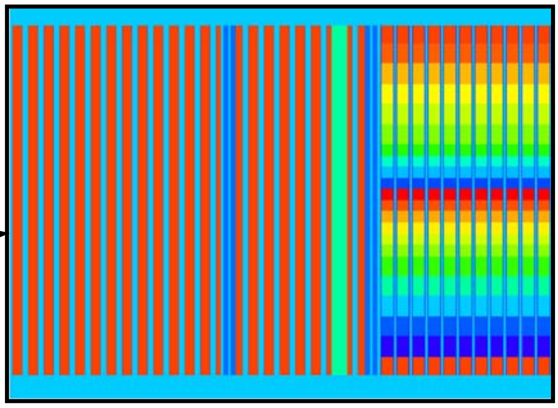

Figure 3.7: Detail of the RZ core section

3.3 Verification of the models

The models and the system codes that were used went through extensive code assessment campaigns and benchmarking against experimental results and theoretical analyses (see for instance JNC (2000) /78/, NEA (2003) /79/, and Turner (2002) /80/).

However, since both the supercritical water equation of state for SIMMER-III and the MXN code were specifically developed for this work and did not go through an extensive validation procedure, a few verification tests were performed. For reasons of simplicity, a single channel was considered for this analysis and the average axial power profile was used for the calculations of several fluid-dynamics parameters (see Figure 3.8).

The channel is divided into three subchannels and it is filled up with fuel subassemblies, which have the same physical and geometrical properties of the seed regions of the SCFR.

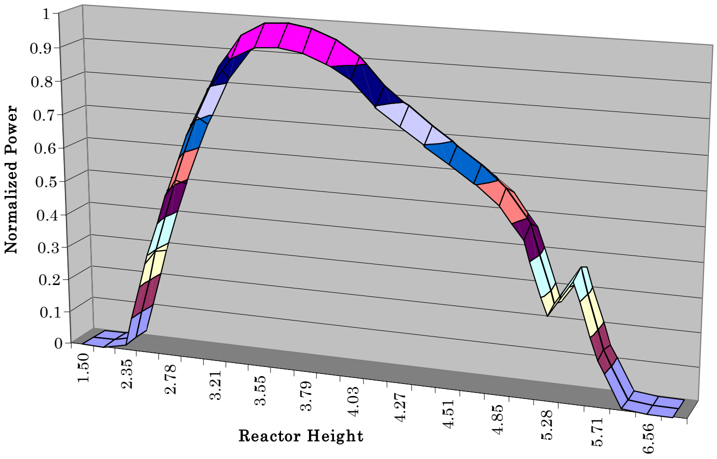

Figure 3.8: Channel power distribution

The first parameters that were studied were the average fuel temperature, which affects the characteristics of the nuclear cross sections and therefore has a very high impact on the neutronics behavior of the reactor (i.e. Doppler effect), and the cladding temperature, which is the first barrier to the leakage of fission products and its value constitutes a very important safety parameter. The results, which show the comparison of the MXN and the SIMMER calculations, are reported in Figure 3.9.

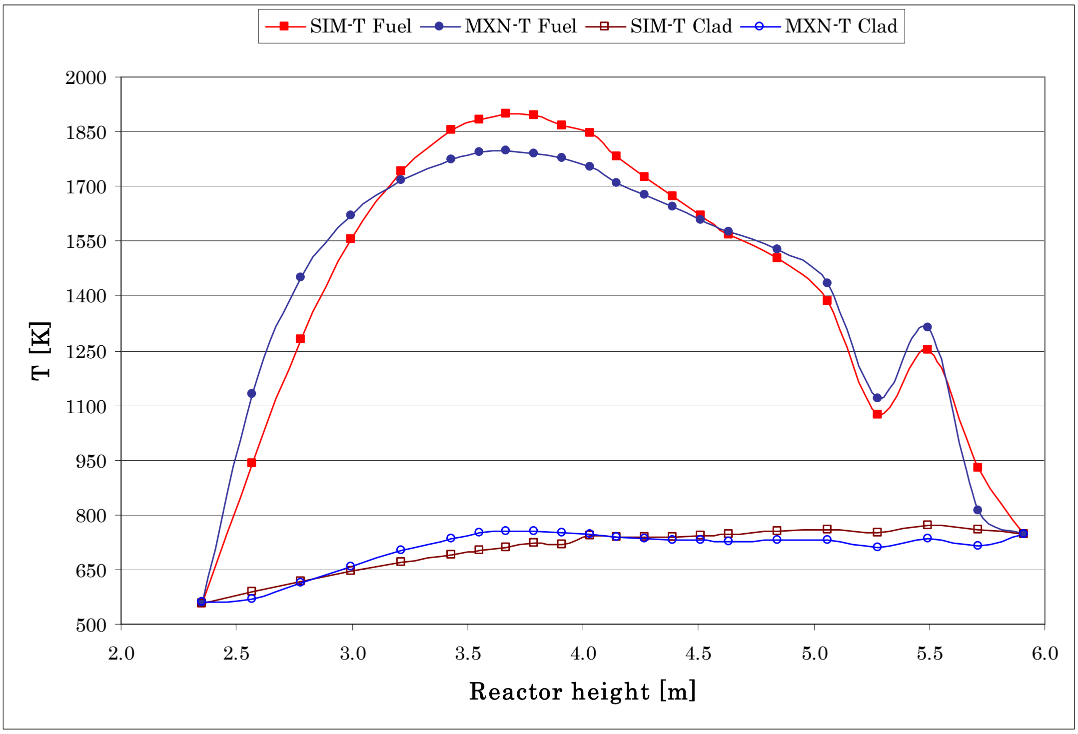

Figure 3.9: Fuel and cladding temperature distribution (single channel analysis)

The agreement among the different curves is very satisfactory, especially given the fact that although similar, the gap conductance and the fuel conductivity models are different. Figure 3.9 suggests that the fuel conductivity predicted by SIMMER-III is higher for lower temperatures than the one predicted by MXN, although in good agreement. The calculated cladding temperatures are also in good agreement, although it is interesting to point out the fact that SIMMER-III predicts a higher heat exchange in the pseudo-liquid phase and a lower one in the pseudo-vapor phase (the transition point is at about four meters as can be seen in Figure 3.10).

This phenomenon is to be attributed to the different heat transfer coefficient; as mentioned in Chapter 2.2 in MXN the Bishop correlation was used while in SIMMER-III different correlations are used for the pseudo-liquid and for the pseudo-vapor phase[15], in any case these results are coherent with the results presented in [Siefken (2003) /65/].

---

[15] $Nu=0.025(Re^{0.8}\ Pr^{0.8})$ and $Nu=0.023(Re^{0.8}\ Pr^{0.3})$ respectively.

Another reason that can concur to the behavior observed in Figure 3.9 is the profile of the coolant density that can be noticed Figure 3.10 together with the coolant temperature profile.

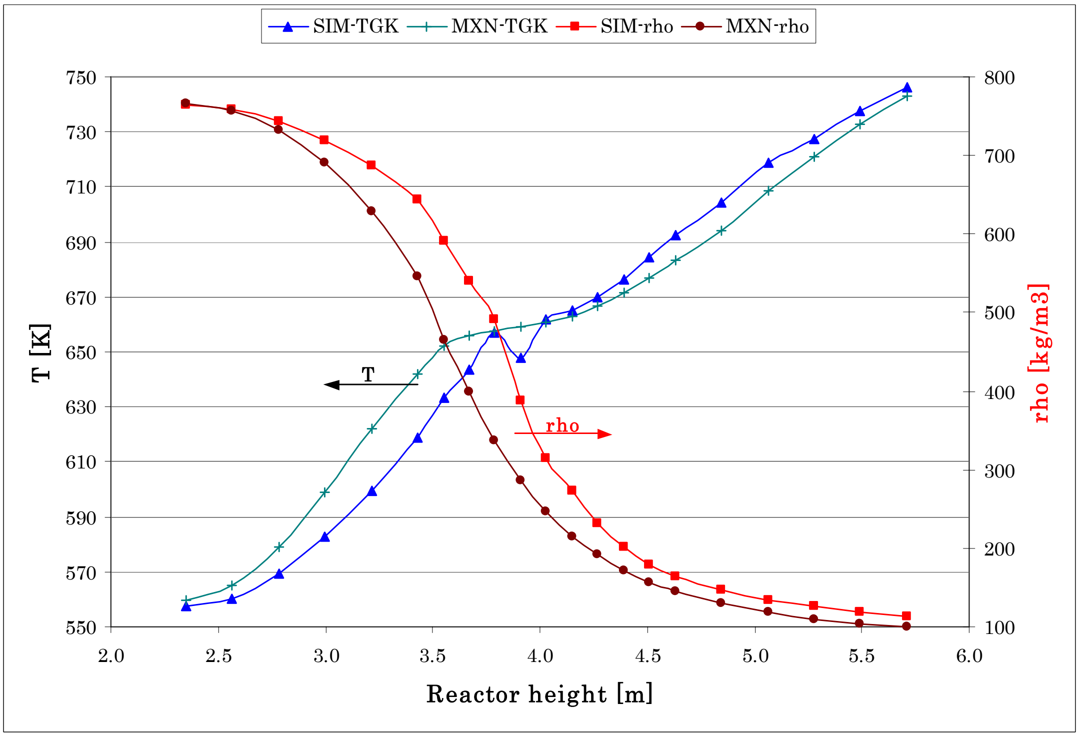

Figure 3.10: Coolant temperature and density distribution (single channel analysis)

Figure 3.10 shows that the agreement between the two codes is rather good, but the density profile does show some discrepancies. This difference is to be attributed partly to the different fluid-dynamics models that are used, partly to the different methods, and partly to the different handling of the equations of state. Nonetheless, the results are satisfactory and in general agreement, therefore proving the overall accuracy of the adopted codes in the SCFR frame of application.

CHAPTER 4

RESULTS

The design work performed in this thesis in order to estimate and improve the void reactivity coefficient for the SCFR required, as mentioned, the development of new tools of analysis. Nonetheless, the first investigations were performed with techniques and methods, which were already available and which were only successively refined. The results of these studies led to the improvement of the core design itself. However, the introduction of new solutions for the amelioration of the void worth was strictly restricted by the terms of the contractual agreement, which funded this research work. This meant for instance that the dimensions of the core and of the fuel elements and of all their components could not be freely modified. Besides these constraints, and the fulfillment of specific requirements indicated by the contractors, some modifications were introduced and/or investigated more or less extensively according to the terms of the contract, which focused on the general safety aspects of this reactor beyond the void coefficient. As a matter of fact, several additional studies were conducted regarding: the identification of accident sequences, the analysis of severe accidents, their enhancement/mitigation phenomena (including design aspects), and the evaluation of a PSA together with an investigation of the effects of the introduction of passive safety components. Still, the enhancement of the void effect represented one of the main goals of the work.

4.1 Neutronics Analyses for the SCFR

Neutron physics of the void effect

Like other fast homogeneous MOX fuelled cores, a homogeneous MOX SCFR core would have a strong positive void effect if special design features were not implemented. The main factors, which define the void effect, are: hardening of neutron spectra (due to decreased neutron moderation) and increasing of leakage from the core (due to higher core transparency). Voiding also affects the fine (resonance) neutron spectrum shape, that effectively decreases the neutron cross-section of heavy nuclides in the resonance energy region (self-shielding effect), and avoids absorption in the coolant, but these factors are usually of smaller importance.

The hardening of neutron spectra decreases the ^{238}U (and other ‘fertile’ nuclides like ^{240}Pu) relative absorption rates while increasing the corresponding threshold fission rates, therefore causing a reactivity increase. On the other hand, the ‘fissile’ nuclides (^{239}Pu and ^{235}U) relative fission and capture rate decreases, causing a total negative contribution to reactivity. This last effect is, however, of lower magnitude if the amount of ^{235}U is small, and the amount of ^{240}Pu (and heavier actinides) in the MOX fuel is significant. Consequently, the hardening of neutron spectra gives a positive contribution to the void effect for a MOX core. The overall effect can be considered as corresponding to an increase in the average η value of the fuel (average generation cross-section to average absorption cross-section ratio).

A negative contribution to reactivity instead can be given by the increasing of neutron leakage from the core. This contribution is significant, however, only if the leakage component of the neutron balance is not too small, and this is usually not the case for a large homogeneous reactor.

Therefore, in order to avoid a strong positive void effect (and coolant density coefficient), a special heterogeneous design with 3 annular rings of MOX fueled (seed) and blanket subassemblies was applied to the SCFR concept by the design team of the Nuclear Engineering Research Laboratory of the University of Tokyo. This design solution increases significantly the leakage from the seed, and reduces the void effect. Moreover, zirconium hydride layers were placed in the blanket subassemblies: ZrH is a strong solid moderator that does not disappear in case of loss of coolant.

The introduction of these thin rings (they are about 1 cm thick) strongly affects the spatial and energy distributions of the neutron flux at void conditions. Because of the moderating effect of the ZrH layers, the neutron spectra hardening upon voiding in the seed near the boundaries with the blankets is much less pronounced, compared to a design without solid moderator pins. This effect implies that the positive spectral contribution to the void effect is reduced and the local relative fission rate increases (thus, increasing the fraction of neutrons leaking from the seed into the blanket). As a result, the total void effect at the beginning of cycle is negative and equal to –1.5$[16] (at the end of cycle the value is close to zero). For a similar SCFR design with 2 seed rings [Jevremovic (1993) /41/], the computed void effect was about –3$, the seed contribution being about –4$ (the blanket contribution being positive).

Deterministic analysis of the void effect in the SCFR

The basic neutronics features for a reactor are usually defined by the neutron spectrum. Figure 4.1 shows the neutron spectrum for the SCFR, evaluated with TWODANT, compared to the spectra of other reactors. Similarly to other fast reactors the main contributions to the reactivity are related to resonance (below few keV) and fast (above few keV) neutrons, while shifts in neutron spectra (due to possible perturbations) within the thermal and epithermal energy range (below 1 eV) and related feedback effects, which play a key role in conventional LWRs, are less important for the SCFR.

On the other hand, unlike in LMFRs, an accurate modeling of neutron reactions in the low energy range is quite important for the SCFR [Languille (1995) /81/]. The reason is that the contribution of all thermal and low energy resonance neutrons to reactivity effects, in particular the void effect, is comparable to the total effect: that is the (higher in absolute value) contributions of faster neutrons may be of different sign and partially compensate each other.

As mentioned before, a particular SCFR feature is that the coolant density strongly varies with axial position in the core, therefore strong variations in neutron spectra are expected, making this reactor neither a purely thermal, nor a purely fast system.

---

[16] 1$ is about 380 pcm for this system, where 1 pcm is $10^5 \times \rho$ (see Equation (3.1)).

Nonetheless, the seed flux spectrum is steadily decreasing with energy decrease in the low energy range without exhibiting the typical 1/E part and a rise at the energy corresponding to the moderator average temperature (contrary to conventional LWRs).

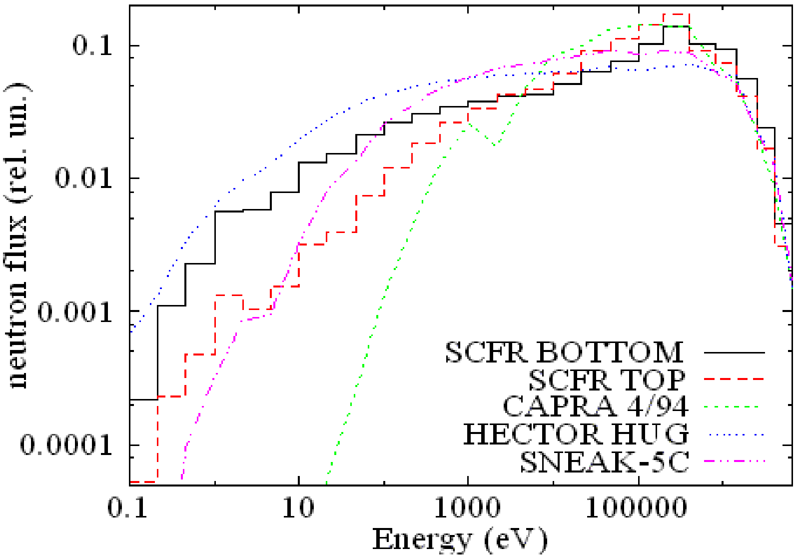

Figure 4.1: Neutron spectra in SCFR seed, LMFR (CAPRA reactor) and graphite-moderated critical assemblies

Preliminary evaluations (made for graphite-moderated experimental configurations with k-infinite close to unity and similar spectrum: HECTOR HUG and SNEAK-5C [Kiefhaber (1972) /82/], see Figure 4.1) have shown that nuclear data libraries with a small number of groups, traditionally used for fast reactor analyses at FZK (e.g. the 11-group library in SIMMER-III), may give too large errors in criticality at the SCFR nominal conditions due to inaccurate modeling of neutron slowing-down in the low energy range (basically caused by using a LMFR weighting spectrum for a coarse low energy group structure). For example for the HECTOR-HUG case, the 11 group library over-predicts k-infinite by about 20%. Therefore these libraries were excluded from further considerations related to the SCFR studies (at least in wet conditions, since these libraries may still be adequate for voided configurations).

Despite the above mentioned remarks, during the first stage of neutronics investigations conventional fast reactor analysis tools were used and a 2D RZ SCFR model was developed (see Figure 4.2).

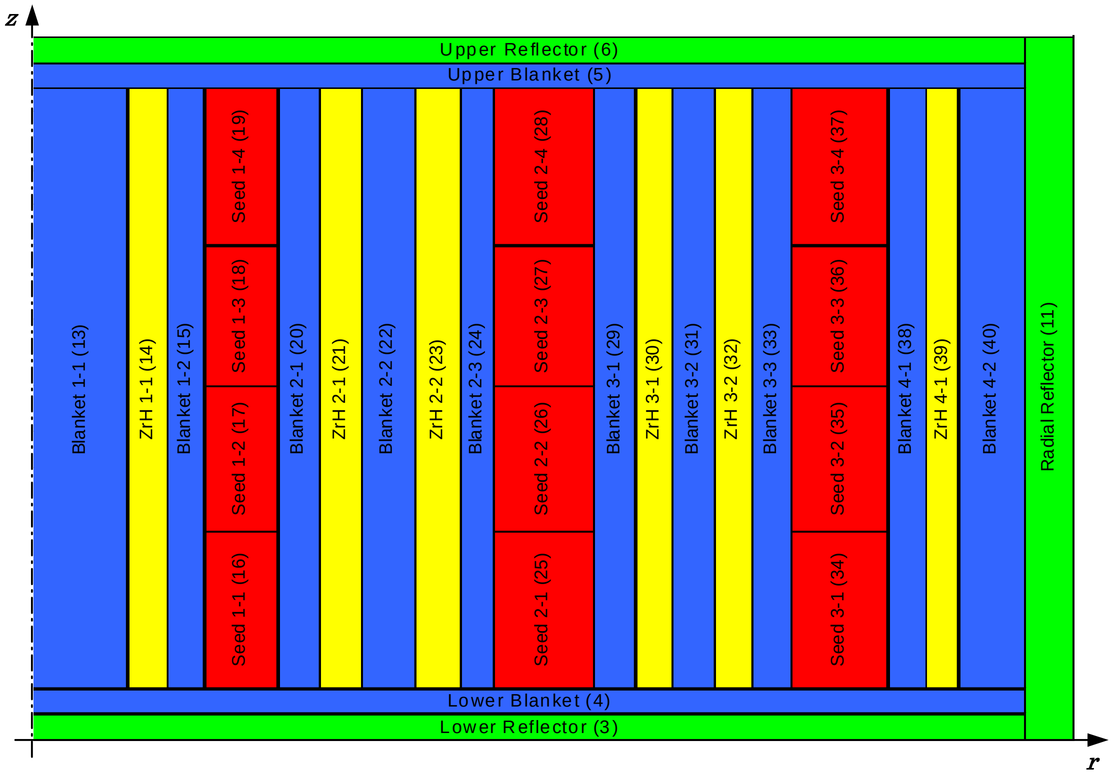

Figure 4.2: RZ SCFR model

The calculations were performed using mainly the RHEIN code system /45/ and a 26-group library (based on the ENDF/B-VI evaluated nuclear data for the main nuclides). In addition to the 26-group cross-section library, we employed a 172-group (with JEF-2.2 based data) library. It should be noted that for accurate modeling of neutron slowing-down in the resonance energy range (especially in the area of few hundred eV) both 26 and 172 group structures are not sufficiently fine: a much greater (of at least 1 order more than in the 172-group dataset) number of energy groups is needed to properly take into account the cross-section structure there (if the conventional narrow resonance approximation is employed). At higher energies (important for LMFRs) the cross-section resonance widths are narrow and e.g. a 26-group description is quite accurate for the resonance cross-sections of the heavy nuclides. At lower energies (important for LWRs) the cross-sections can be described in a proper manner with a reasonable number of groups, in the order of few tens. The inaccuracies related to the resonance energy modeling (resonance self-shielding, resonance overlapping of the same isotope and of different isotopes), which are of lower importance to LMFR and LWR, may introduce a significant uncertainty in computed k-effective values for the SCFR at nominal conditions.

A simple heterogeneous model based on the fuel pin geometry was employed in the seed. The model is based on the Bell correction technique [Waltar (1981) /66/]. It employs a cell-volume-to-fuel-surface ratio for adjusting the non-fuel isotope cross-sections while these cross-sections are used (as components of a "background" cross-section) for computing effective f-factors (to take into account self-shielding effects) for the fuel isotopes. To compute this ratio, the seed subassembly volume was divided by a product of pin fuel surface and number of pins in the subassembly. Thus, the can walls and the coolant between the seed subassemblies were taken into account, but adjacent blanket subassemblies and corresponding materials (e.g. ZrH) were ignored while performing the cell calculations. This model usually may take into account the main part of the heterogeneity effects in the conventional fast reactor fuel subassemblies. In LMFRs this effect is usually quite small. In the SCFR case, however, the heterogeneous effects are much larger due to the softer spectrum, as the self-shielding of the neutron cross-sections is more pronounced and the neutron mean free path is smaller in the resonance energy range. The blanket was considered homogeneous (application of the available simple heterogeneous model did not give a significant effect).

The void and Doppler effects in the SCFR are correlated (as in LMFRs). The Doppler effect is much greater (by roughly a factor of 2) at wet conditions (than at dry ones): a temperature rise from 300K to 900K gives about –6$ at the wet and about –2.5$ at voided states (the difference would be more pronounced for a design without ZrH due to stronger shifts in spectra). That is due to the fact that the resonance energy neutrons (the Doppler contributors) are of less importance in voided conditions. On the other hand, this means that the void effect depends strongly upon the fuel temperature.

Taking the same (nominal) coolant density distribution, the void effect is significantly lower at low temperatures than at high ones: at 300K the void effect is of about –6$ (the seed contribution being about –12$), while at 1200K it is about –1$, see Table 4.1, (the seed contribution being about –6$).

Doppler Reactivity Effect	Value
Wet	~ -6$
Dry	~ -2.5$
Void Reactivity Effect	**Value**
Cold (300K)	~ -6$
Hot (1200K)	~ -1$

Table 4.1: Void & Doppler effect (deterministic analysis)

Both seed and blanket contributions are in qualitative agreement with the before mentioned published results, but higher (in absolute value) than expected. The value relative to the blanket was probably overestimated because of the homogeneous treatment. Simple addition of seed and blanket contributions assumes that voiding happens simultaneously in the two regions, which have significantly different temperature and power densities. On the other hand, the use of the 26-group approximation most probably overestimated (in absolute value) the corresponding seed value.

The energy group contributions to the reactor voiding are shown in Figure 4.3 the contributions from the fast neutrons are dominating by amplitude. However, the lower energy neutron contributions are not negligible and may even determine the sign of the effect (if the sum of all high energy contributions is close to zero).

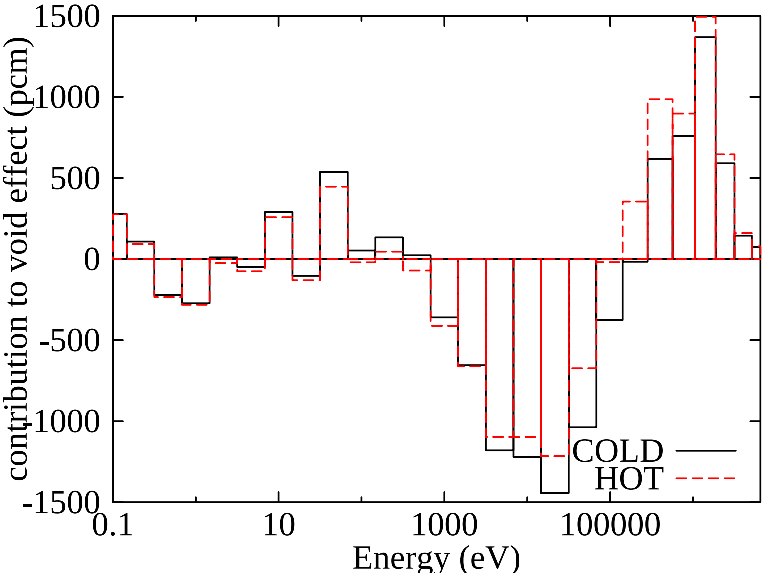

Figure 4.3: Contributions from different energy groups to the void effect at cold (fuel temperature is 300K) and hot (fuel temperature is 1200K) conditions

To investigate the void effect in more detail two stages were analyzed separately: voiding of the seed and voiding of the rest of the reactor. For the seed voiding, the main driving force is the changing of the spatial flux distribution. In Figure 4.4 one may see the variation of the power density distribution in the central core layer (the blankets are still containing water).

As a result of flux peaking near seed boundaries, the leakage component of the neutron balance (in the seed) approximately doubles after seed voiding (compared to original 12% at nominal conditions), thus giving a negative contribution to the reactivity. The neutrons leaking from the core (to the blanket) are mainly absorbed in the blanket. A part of the leaked neutrons, however, increases fission in the blanket. Therefore, the blanket contribution to the total fission rate increases by about 2%, partially compensating the negative “leakage” contribution to the reactivity. This compensation would be less significant (and therefore the void effect would be more negative) if the effective fission cross-sections in the blanket material were lower (e.g. if ^{232}Th were used instead of ^{238}U).

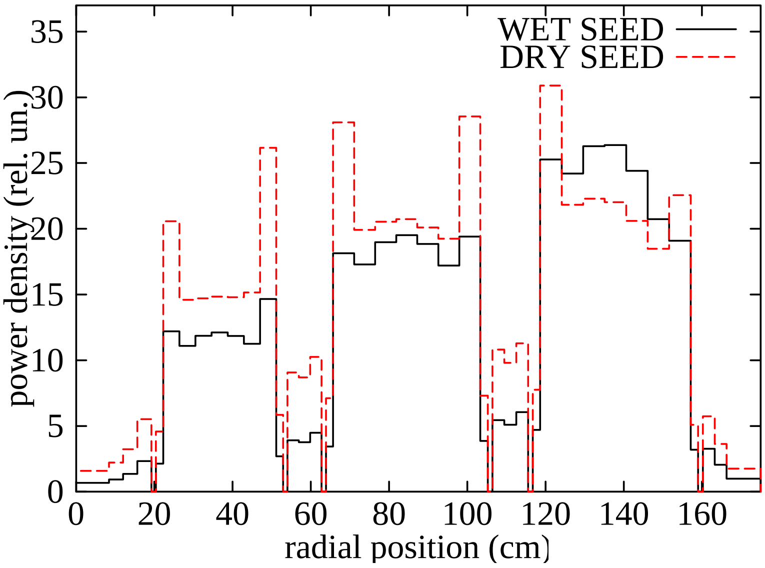

Figure 4.4: Power density distribution near the axial mid-plane

Contributions (to the void effect in the seed) vary significantly depending upon radial and axial position. The contribution of the outermost seed ring is of about 70% (of the total effect in the seed), while the contribution of the innermost seed ring is almost negligible. The lower seed half (with higher coolant density) gives a much higher contribution compared to the upper seed half. It may be worth to point out that the linear superimposition of these contributions would not give the value of the total reactor void effect; it is however of relevance to evaluate these separate effects in order to gain a better understanding of the core dynamic and identify the regions of higher neutronics importance that actually drive the phenomena in one direction or the other.

Voiding of the blankets (in addition to seed voiding) increases the reactivity, hardening the neutron spectra in the blankets and in the seed. The negative “leakage” component of the reactivity also decreases (in magnitude) compared to the “dry seed, wet blanket” state due to smaller spectra differences between the seed and the blanket.

In Figure 4.5 one may compare integral seed and blanket spectra at nominal (wet), void (dry), and after the disintegration of zirconium hydride (no hydrogen in the core) conditions[17]. At wet and dry conditions, the blanket spectra are softer because the zirconium hydride layers are situated within the blankets. Due to this phenomenon, voiding changes the seed spectra more appreciably than those in the blanket. The disintegration of zirconium hydride brings the seed and blanket spectra close to those of conventional LMFRs (see Figure 4.1).

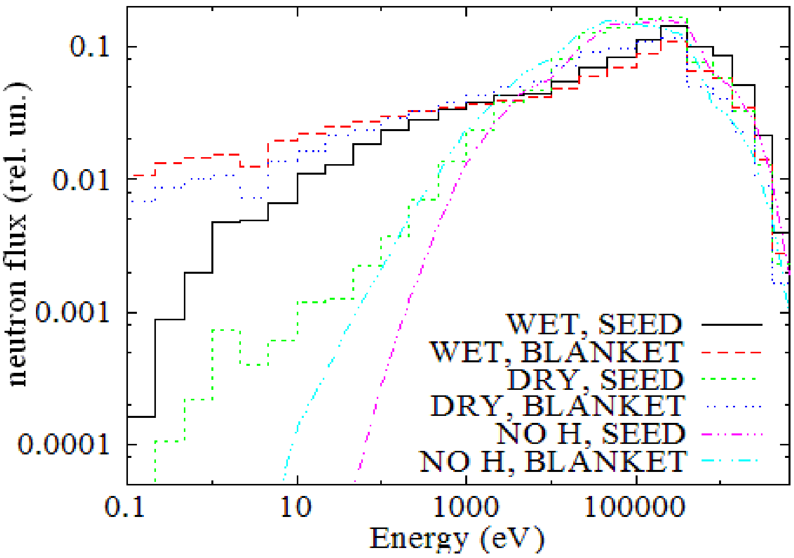

Figure 4.5: Integral seed and blanket spectra at nominal (wet), void (dry), and after disintegration of $ZrH_{1.7}$ (no hydrogen in the core) conditions

Remarks on the deterministic analyses

According to the past experience the inaccuracies related to the insufficient number of groups and approximate heterogeneity treatment, often compensate partly each other for the 26-group LMFR computations. For the SCFR case the compensation effects might be smaller. Currently, the k-effective results obtained for the wet conditions with 26-group data have an estimated uncertainty of at least 1000 pcm (about 3$). This was confirmed by comparing the results of 26-group and 172-group calculations. Since the criticality values for the voided states (with similar spectra as in the LMFR case) should be more accurate, the void effects, presented in the following and based on the 26-group calculations, have also an uncertainty of the order of 3$.

---

[17] A significant core heating, that may follow voiding, may give rise to the disintegration of the solid moderator layers. The associated loss of hydrogen causes a strong positive reactivity shift of ~+10$ (compared to the already voided reactor state) due to the very strong neutron spectrum shift.

Taking into account these uncertainties, one could estimate a void effect close to zero at nominal conditions. This does not contradict open literature results where this effect was estimated to be about –2$ (see also Table 2.1). However, more refined neutronics studies are needed to give a more accurate evaluation of the void effect and to confirm the conclusions of the published results on the definite negative sign of the void effect in SCFR.

A more accurate taking into account of the fine cross-section structure and heterogeneity effects could reduce current uncertainties in the void effect and also describe more precisely data for the local power densities, e.g. close to the ZrH layers. That could be done e.g. by using a "continuous energy" Monte-Carlo code and detailed modeling of the geometry structure in the core.

4.2 Refined neutronics analyses for the SCFR

As mentioned in the previous paragraphs, the void effect was computed in the past by using a cell model for effective multigroup cross-section generation and 2D RZ reactor model for full reactor calculations (see for instance Oka (1996) /42/). Their estimated void effect is slightly negative (~ –1$). The results relative to similar calculations, although based on different cross-section data and cell model, a different number of neutron energy groups, and a slightly different computation model, were just shown. In general, the preliminary investigations discussed in the previous paragraphs confirmed the earlier published results and came to the same conclusion with respect to the mechanisms restricting the void effect from being unacceptably high. As a result of our calculations then, the void effect was estimated as being slightly negative (–1$) or zero with an uncertainty, related to the nuclear data uncertainties and modeling approximations, of approximately 10$[18].

A computation model for a "continuous energy" Monte-Carlo code, MCNP4C, with detailed (i.e. by specifying geometry and position of the inner - fuel/fertile/moderator - part of the pins, cladding, coolant, wrapper and other elements, such as gaps, for each subassembly) representation of the SCFR geometry structure in the core has been introduced. Ideally, such a model may give an accurate value of a physical parameter, such as k-effective, provided that the nuclear data are accurate and the material and temperature distributions in the core are described correctly. Hence,

---

[18] The differences that were actually computed among the different models account for about 5$, a factor 2 was then applied to conservatively take into account cross-section and model approximations.

the MCNP computation model, the nuclear data, and the reevaluated uncertainties of the void effect will be described in more detail in the following sections.

Geometry model, nuclear data libraries, and data processing options.

As mentioned, the core of the SCFR is highly heterogeneous; thus the decision to develop a detailed MCNP model was taken, in order to describe every single pin, assuming a single average coolant density and fuel temperature throughout the core[19].

The MCNP input deck was run with different cross section data files and with different options introduced in the files themselves (delayed neutrons, probability tables, and different models for hydrogen scattering). In addition to the nuclear data supplied with MCNP and based on the previous releases of ENDF/B-VI (these data will be referenced in the following as ENDF-6.2), 3 additional data libraries were processed into the MCNP format, the libraries being ENDF/B-VI, release 7 (ENDF-6.7), JEF-2.2, and JENDL-3.2. A short description of these libraries and of the nuclear data processing options is given in Appendix A.

These mentioned data may, as it will be shown in the following, differ quite significantly. Each evaluation may have advantages and disadvantages, the differences reflecting evaluator's strategies and personal opinions in attributing priorities to different experimental results and employing different fitting techniques. Therefore, results obtained with different libraries may reflect to a certain degree the existing uncertainties in nuclear data. However, the uncertainty of the void effect can not be derived in a straightforward manner from the computations with ENDF, JEF, JENDL: in many cases the latest sophisticated experiments have got the highest level of credibility by all, including ENDF, JEF, and JENDL evaluators. Thus, the nuclear data libraries may contain similar errors that may increase (e.g. by a factor of 2) the level of uncertainties that could be estimated by considering deviations between the computed figures. The only way to lower the uncertainty then is to take into account a representative set of relevant experimental results for the considered reactor design and physical parameter.

---

[19] The average coolant density (~ 400 kg m^{-3}) was calculated taking into account the nominal core inlet and outlet coolant conditions and assuming a sinusoidal axial and a flat radial power profile. The same hypotheses were used to estimate the average fuel temperature (~ 1200 K).

In order to give an idea of the discrepancies among different cross section evaluations, fission and capture cross section for both ^{239}Pu and ^{238}U are reported in Figure 4.6, Figure 4.7, Figure 4.8, and Figure 4.9. The curves (172-group average cross-sections, averaging being done employing the Fermi/fission spectra below/above 2.5 MeV) represent the relative deviation of JEF-2.2 and JENDL-3.2 to ENDF-6.7 data. The biggest differences are, as one would expect, in the higher energy region, and are related in particular to the ^{239}Pu capture cross-section (>100%). These incongruities help to explain the results and the associated uncertainties that will be outlined in the following void reactivity coefficient calculations.

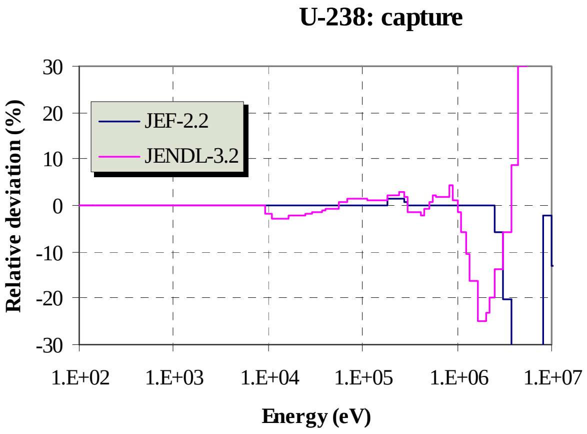
U-238: capture

Figure 4.6: ^{238}U capture relative to ENDFB6.7

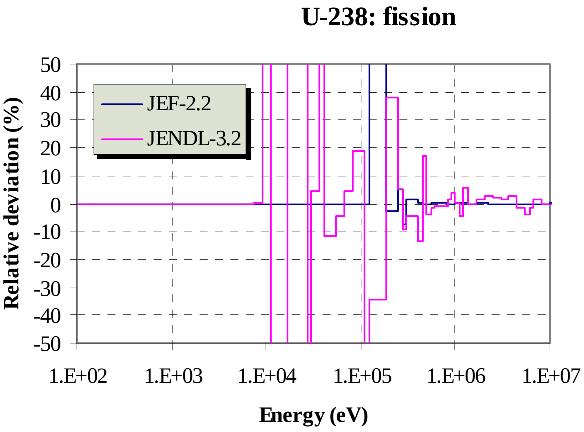
U-238: fission

Figure 4.7: ^{238}U fission relative to ENDFB6.7

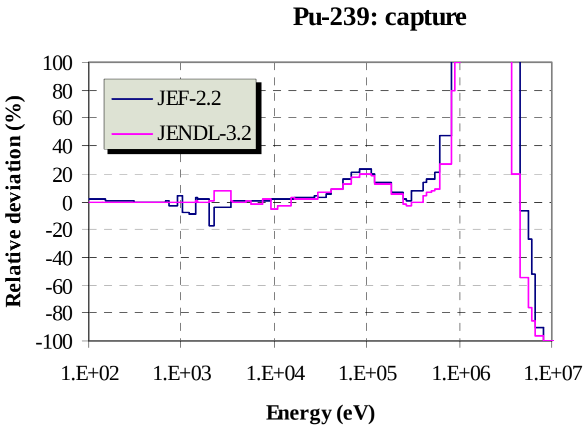
Pu-239: capture

Figure 4.8: ^{239}Pu capture relative to ENDFB6.7

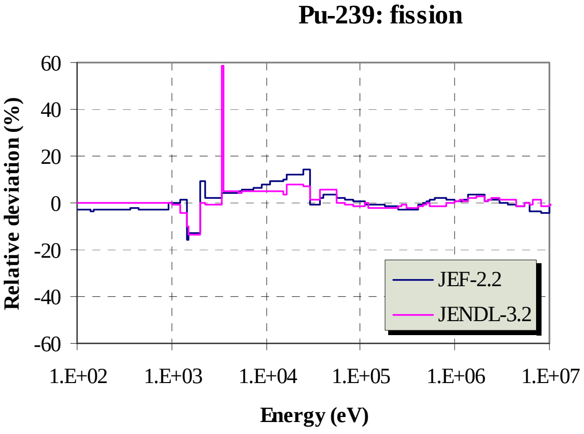
Pu-239: fission

Figure 4.9: ^{239}Pu fission relative to ENDFB6.7

The deviations in averaged cross-sections represent only a part of the uncertainties related to nuclear data. The nuclear files may contain resonance data, including the average resonance parameters that are probability distributions of resonance energies and widths [Rose (1990) /83/]. Uncertainties in treating these data (different approaches may be applied in the available deterministic and Monte-Carlo models) may bring a significant shift in computed k-effective values for compositions with fast spectra, while playing a minor role for moderated systems. That is why an accurate treatment of average resonance parameters in the unresolved resonance energy region is obligatory for void evaluations; a part of the related effects should be taken into account while considering uncertainties of void computations. Recently, a capability of employing probability tables computed from the average resonance parameters has being added to MCNP, and was applied in this work.

Another important uncertainty factor is represented by thermal scattering data (describing how the low energy neutrons may scatter with moving molecules, relatively to their temperature). A rich experience of computation does exist for the conventional LWR design and therefore the scattering data for hydrogen are validated for this application. However, employment of the hydrogen scattering models for the SCFR (based on the LWR experience)may give rise to inaccuracies in computed k-effective values at wet states, bringing similar inaccuracies to computed void effect values. That is why a part of scattering data treatment correction (i.e. the difference between results obtained by using this treatment and a free gas model) may be added to the uncertainties of the calculated void effect.

Yet another uncertainty is related to the treatment of H in ZrH (with respect to the thermal scattering). Though a certain experience with this material in reactor installations is available, the available data related to the corresponding C/E (calculations to experiment ratio) analyses seems to be insufficient to rely completely on the provided information in the nuclear libraries scattering data for ZrH for criticality and void calculations in the SCFR. Thus, similarly to the water case, a comparison between thermal scattering data and the free gas model for hydrogen is done (to get an idea about a possible uncertainty level).

Since the data and techniques applied may not be sufficiently refined (e.g. different processing methods may provide different probability tables from the same nuclear data), simplified models were adopted assuming either the use of average cross-sections (i.e. ignoring resonance self-shielding) in the unresolved energy region, or the use of prompt fission neutron spectra, or the use of free-gas scattering models either for water or for zirconium hydride. As reported earlier, the fuel temperature may affect significantly the void value. That is why a temperature effect should be again reevaluated for the refined geometry and cross-section processing model. The results are summarized in the following section.

With respect to geometry, the MCNP reference model was a full three-dimensional model, with variable (vs. position in space) plutonium enrichment and water density. 3D modeling allowed taking into account axial neutron leakage in void conditions, which was expected to increase with spectrum hardening caused by voiding.

In order to evaluate the uncertainties related to nuclear data and modeling (i.e. nuclear data processing) options, a two-dimensional model was employed, representing a mid-plane section of the SCFR as shown in Figure 2.1. For this model the average plutonium enrichment (~23%), and the average water density were employed. 2D modeling preserves the most important features related to spectra and radial profile shifts in neutron fluxes due to voiding and may provide less statistically uncertain results with the same CPU time. In addition, employment of several geometry arrangements helps checking Monte-Carlo and deterministic models/results.

ENDF/B is the reference data library for this work because it was the most recent available library and because of the larger experience in processing these data (for other applications). Thus, both 3D and 2D calculations were performed with the ENDF-6.7 library: providing reference 3D results and for further comparisons with 2D results obtained with other data and computation options.

Summary of the computed results and void effect uncertainties

For each data set, and for each one of the four data set configurations five calculations have been performed adopting the average plutonium enrichment in the fuel (~23%), and therefore neglecting the spatial enrichment distribution. A fuel temperature of 1200K, a coolant and zirconium hydride layer temperature of 800K, and a blanket composition of depleted uranium with a content of ^{235}U limited to 0.5%, were assumed and applied to all five cases:

1. Nominal conditions, nominal coolant density (averaged);
2. Seed regions half voided;
3. Seed regions completely voided;
4. Seed regions and inner blanket regions half voided;
5. Reactor completely voided.

Only k-effective for nominal conditions, for seed total void and for reactor total void are reported here; beta effective (β_{eff}) has been calculated for nominal conditions with the deterministic code RHEIN and is equal to $3.77 \cdot 10^{-3}$ for nominal conditions (therefore 1 \$ = 377 pcm). The β_{eff} value increases slightly (by ~ 2%) for the voided conditions, because of higher contribution of ^{238}U fissions with its larger delayed neutron fraction (see for instance [Glasstone & Sesonske (1994) /84/]), this change, however, is negligible compared to existing uncertainties in the void effect and will not be taken into account.

In all the following tables, all relative to the full MCNP 2D core model (crossed options are not active):

N → stands for libraries including delayed neutrons;

D → stands for libraries including probability table treatment;

P → stands for no probability table treatment of the unresolved resonance region;

$H_2 0$ → stands for thermal scattering treatment of hydrogen bound in the water molecule;

ZrH → stands for thermal scattering treatment of hydrogen bound in zirconium hydride.

Table 4.2 shows the results obtained with the ENDF/B-VI standard MCNP library. For this library, calculations at 300K have been performed too. It is worth noting how the void reactivity coefficient decreases in absolute value with temperature. Another result that should be underlined and that also holds for all the other calculations is that the seed void effect is always strongly negative, showing how the presence of more moderator in the blankets increases the number of captures in the ^{238}U (99.5%) present in these regions. In this and in the following tables the effect of using libraries that include delayed neutron data can also be observed

The spectrum of delayed neutrons is softer than the spectrum of prompt ones by roughly a factor 3 or 5 [Kiefhaber (1992) /85/]. It follows that the influence on criticality becomes noticeable if the importance of prompt fission neutrons (~100keV for the SCFR) differs significantly from the importance of the delayed ones (~20keV). For this specific design including these data affects the results by ~±200pcm, thus predicting a stronger effect than the adoption of probability tables in the unresolved resonance region.

T(H_2O)=300K, T(fuel)=300K		**~~H_2O~~ N ~~P~~ ~~D~~ ~~ZrH~~**	**T(H_2O)=300K, T(fuel)=300K**		**H_2O N ~~P~~ ~~D~~ ~~ZrH~~**
ENDF60	*Nominal k-eff*	*1.04606*	*ENDF60*	*Nominal k-eff*	*1.04356*
Seed Void	-1752 [pcm]	-4.74 [$]	Seed Void	-1668 [pcm]	-4.51 [$]
Total Void	-995 [pcm]	-2.69 [$]	Total Void	-830 [pcm]	-2.24 [$]
T(H_2O)=300K, T(fuel)=300K		**H_2O N ~~P~~ D ~~ZrH~~**	**T(H_2O)=300K, T(fuel)=300K**		**~~H_2O~~ ~~N~~ P ~~D~~ ~~ZrH~~**
ENDF60	*Nominal k-eff*	*1.04158*	*ENDF60*	*Nominal k-eff*	*1.04562*
Seed Void	-1500 [pcm]	-4.06 [$]	Seed Void	-1544 [pcm]	-4.17 [$]
Total Void	-589 [pcm]	-1.59 [$]	Total Void	-683 [pcm]	-1.84 [$]
T(H_2O)=800K, T(fuel)=1200K		**H_2O N ~~P~~ ~~D~~ ~~ZrH~~**	**T(H_2O)=800K, T(fuel)=1200K**		**H_2O ~~N~~ P ~~D~~ ZrH**
ENDF60	*Nominal k-eff*	*1.02037*	*ENDF60*	*Nominal k-eff*	*1.02190*
Seed Void	-1192 [pcm]	-3.22 [$]	Seed Void	-984 [pcm]	-2.66 [$]
Total Void	-223 [pcm]	-0.60 [$]	Total Void	+206 [pcm]	+0.56 [$]

Table 4.2: ENDF/B-6.0 void effect results

Table 4.3, Table 4.4, and Table 4.5 show the results obtained with ENDF/B-VI release 7, JENDL-3.2, and JEF-2.2, respectively. These libraries refer to the nominal temperature conditions quoted above and, as reported, three data files were developed per library: NP, D, and P. Therefore for each data file different options were introduced. What is important to note here, because of data coherency all the libraries were available for the nominal fuel temperature, is the effect of the introduction of probability tables.

The implementation of these data has an evident effect just for the JEF-2.2 library for which the void reactivity coefficient is increased by ~250pcm, in all other cases the effect is in the order of few tens of pcm. The four reported tables also allow the evaluation of how the correct modeling of hydrogen scattering in zirconium hydride affects the results, accounting for the positive moderating effect of these elements.

This effect, however, is most appreciated with data files, which include probability tables and for the ENDF/B-VI library. In the perspective of performing comparisons with deterministic codes it is interesting to note in Table 4.5 that substituting the scattering data for hydrogen bound in zirconium hydride with the scattering data for water, that is to assume that hydrogen behaves in the zirconium matrix as if it were bound in the water molecule, introduces a negative effect of ~+100pcm. Water scattering is usually the available option in deterministic codes and therefore this difference should be accounted for. This result points out that the lack of a scattering model for supercritical water might be an underestimated uncertainty for this reactor. The effect of the introduction of thermal scattering data for water can be appreciated examining again the figures reported in Table 4.2.

T(H_2O)=800K, T(fuel)=1200K		H_2O N ~~P~~ ~~D~~ ~~ZrH~~
ENDF67	*Nominal k-eff*	*1.00803*
Seed Void	-624 [pcm]	-1.69 [$]
Total Void	+784 [pcm]	+2.12 [$]

T(H_2O)=800K, T(fuel)=1200K		H_2O ~~N~~ P D ~~ZrH~~
ENDF67	*Nominal k-eff*	*1.00872*
Seed Void	-803 [pcm]	-2.17 [$]
Total Void	+578 [pcm]	+1.56 [$]

T(H_2O)=800K, T(fuel)=1200K		H_2O N ~~P~~ D ~~ZrH~~
ENDF67	*Nominal k-eff*	*1.00775*
Seed Void	-656 [pcm]	-1.87 [$]
Total Void	+547 [pcm]	+1.56 [$]

T(H_2O)=800K, T(fuel)=1200K		H_2O ~~N~~ P D ZrH
ENDF67	*Nominal k-eff*	*1.01076*
Seed Void	-604 [pcm]	-1.63 [$]
Total Void	+454 [pcm]	+1.23 [$]

Table 4.3: ENDF/B-6.7 void effect results

T(H2O)=800K, T(fuel)=1200K		H2O N ~~P~~ ~~D~~ ~~ZrH~~
JENDL32	*Nominal k-eff*	*0.99946*
Seed Void	-1121 [pcm]	-3.03 [$]
Total Void	-160 [pcm]	-0.43 [$]

T(H2O)=800K, T(fuel)=1200K		H2O ~~N~~ P D ~~ZrH~~
JENDL32	*Nominal k-eff*	*0.99921*
Seed Void	-1148 [pcm]	-3.10 [$]
Total Void	+93 [pcm]	+0.25 [$]

T(H2O)=800K, T(fuel)=1200K		H2O N ~~P~~ D ~~ZrH~~
JENDL32	*Nominal k-eff*	*0.99853*
Seed Void	-1274 [pcm]	-3.44 [$]
Total Void	+103 [pcm]	+0.28 [$]

T(H2O)=800K, T(fuel)=1200K		H2O ~~N~~ P D ZrH
JENDL32	*Nominal k-eff*	*1.00061*
Seed Void	-887 [pcm]	-2.40 [$]
Total Void	+79 [pcm]	+0.21 [$]

Table 4.4: JENDL-3.2 void effect results

T(H2O)=800K, T(fuel)=1200K		H2O N ~~P~~ ~~D~~ ~~ZrH~~
JEF22	*Nominal k-eff*	*0.99622*
Seed Void	-865 [pcm]	-2.34 [$]
Total Void	+253 [pcm]	+0.68 [$]

T(H2O)=800K, T(fuel)=1200K		H2O ~~N~~ P D ~~ZrH~~
JEF22	*Nominal k-eff*	*0.99578*
Seed Void	-863 [pcm]	-2.33 [$]
Total Void	+367 [pcm]	+0.99 [$]

ZrH uses H2O scatt. model for H		H2O ~~N~~ P D ZrH
JEF22	*Nominal k-eff*	*0.99743*
Seed Void	-539 [pcm]	-1.46 [$]
Total Void	+463 [pcm]	+1.25 [$]

238U taken from ENDFB67		H2O N ~~P~~ ~~D~~ ~~ZrH~~
JEF22	*Nominal k-eff*	*1.00174*
Seed Void	-658 [pcm]	-1.78 [$]
Total Void	+639 [pcm]	+1.73 [$]

T(H2O)=800K, T(fuel)=1200K		H2O N ~~P~~ D ~~ZrH~~
JEF22	*Nominal k-eff*	*0.99624*
Seed Void	-1032 [pcm]	-2.79 [$]
Total Void	+21 [pcm]	+0.06 [$]

T(H2O)=800K, T(fuel)=1200K		H2O ~~N~~ P D ZrH
JEF22	*Nominal k-eff*	*0.99851*
Seed Void	-934 [pcm]	-2.53 [$]
Total Void	+360 [pcm]	+0.97 [$]

239Pu taken from ENDFB67		H2O N ~~P~~ ~~D~~ ~~ZrH~~
JEF22	*Nominal k-eff*	*1.00337*
Seed Void	-1233 [pcm]	-3.33 [$]
Total Void	-232 [pcm]	-0.63 [$]

239Pu & 238U from ENDFB67		H2O N ~~P~~ ~~D~~ ~~ZrH~~
JEF22	*Nominal k-eff*	*1.00876*
Seed Void	-1059 [pcm]	-2.86 [$]
Total Void	+215 [pcm]	+0.58 [$]

Table 4.5: JEF-2.2 void effect results (all cases T(H2O)=800K, T(fuel)=1200K)

In fact the application of the available thermal S(α,β) scattering law results in a reactivity change of ~+150pcm; it can be estimated then that the overall uncertainty related to scattering treatment is of about 1$ (see also Table 4.6).

Modeling approximation	No probability tables	Prompt fission spectrum	Free gas H in ZrH	Free gas H in water
Total void	-0.03/+0.93	-0.62/+0.71	-0.04/+0.33	-1.12/-0.68

Table 4.6: Summary of the variation with different approximations in nuclear data treatment

The most interesting results are perhaps reported in Table 4.5. In order to evaluate the effect of different cross section data for different isotopes three calculations were performed substituting ^{239}Pu and ^{238}U in the JEF-2.2 library and taking the corresponding data from ENDF/B-VI.7. The outcome is surprising, the introduction of ENDFB67 ^{238}U increases the reactivity in void conditions by ca. +300pcm, while the reactivity change due to ^{239}Pu (same library) is in the order of ca. –600pcm (see also Table 4.7).

Replacement in JEFF-2.2	^{238}U from ENDFB/VI.7	^{239}Pu from ENDFB/VI.7
Total void variation ($)	+1.05	-1.31

Table 4.7: Variation of the total void effect with mixture of data from different data libraries

The implementation of both data files at once has a negligible effect (~–40pcm), but the single discrepancies are of significant magnitude since they account for more than 1$. The situation is even more dramatic if we consider the nominal conditions data for which the combined effect of the two isotopes is of 3.5$. This behavior can be well understood looking at Figure 4.6 ÷ Figure 4.9. The neutron spectra range of interest (see Figure 4.5) varies according to the regions of the reactor. The cross sections for ^{238}U are mostly relevant in the blanket regions while the cross sections for ^{239}Pu are relevant in the seeds, where the enriched fuel is located.

The ^{238}U captures are approximately 2% lower for the ENDFB/VI.7 library, hence the higher reactivity for this case, while the ^{239}Pu captures are higher, from 2 to ~20%, in the energy range 100 ÷ 10000eV. In the faster energy range the captures of ^{239}Pu decrease, but in the same range fission yield decreases by a greater extent, hence the reduction in reactivity compared to the normal JEF-2.2 library for this case.

3D model

A comparison of the void effect estimated using deterministic models and methods to the supposedly accurate MCNP model would show that the deterministic results are closer to the values available in open literature. This can partly be explained by the compensating effects that are present in a deterministic code (i.e. the Bell correction technique adjusts geometry approximations), which are absent in MCNP. Therefore in order to get reasonable results a more detailed model needs to be developed.

The results reported in the previous tables are all relative to a 2D model of the core (infinite height), which, although extremely convenient to analyze in detail the uncertainties inherent with this kind of study, proves rather inaccurate to describe in absolute values the behavior of the system. As a matter of fact, the introduction of a 3D model changes the estimated void effect very significantly.

The full 3D detailed (pin by pin) model reference results are shown in Table 4.8 (the same calculation conditions explained in footnote 19, pg. 81, are used here). They can be considered as intermediate values between the earlier published results (see for instance /10/ and /42/) (seed void of ca. –4$, total void of ca. –1$) and our preliminary results (seed void of ca. –5$, total void of zero or ca. –1$), therefore proving the importance of an accurate geometrical model in MCNP to predict accurate results, and the relevance of axial streaming under voided conditions for the SCFR.

A good summary of the variations of the criticality and reactivity effects for the 3D model is given in Table 4.9. One may immediately note that the criticality level at nominal conditions may increase or decrease by about 1% depending upon the data. This indicates that different evaluated data are still far from a unique standard (due to incompletenesses and deviations of the available experimental results). Thus, for any distinguished reactor design a set of relevant experiments (if they are available) should be modeled to reduced evident uncertainties. It is worth noting that the seed void effect is always strongly negative, showing how the presence of more moderator in the blankets increases the number of captures in the ^{238}U (99.5%) present in these regions. Switching from ENDF-6.7 to other data libraries makes the total void from ~0.25$ to ~1$ more negative.

Nuclear data	ENDFB/VI.7
k-effective	0.99936
Seed void ($)	-4.26
Total void ($)	-0.47

Table 4.8: Criticality and void effects in the full 3D MCNP model

Data library that replaces ENDFB/VI.7	ENDFB/VI.2	JEF-2.2	JENDL-3.2
k-eff variation	0.01114	-0.01225	-0.01015
Seed void variation ($)	-1.03	-0.90	-0.77
Total void variation ($)	-0.67	-0.26	-1.02

Table 4.9: Variation of criticality and void effect with different nuclear data libraries

The mentioned deviations in the computed parameters, due to different data, result from contributions from individual nuclides.

A certain combination of nuclide data collected from different data libraries may give rise to a much stronger change of the void effect compared to the values shown in Table 4.9. Thus, the uncertainties related to the nuclear data can be estimated as being several times higher that the maximum deviation in Table 4.9.

Effect of temperature

The influence of the fuel temperature on the void effect is shown in Table 4.10 and it confirms the results that were obtained before: there is a strong dependence of the void effect on fuel temperature. If the temperature of the reactor fuel were 300 degrees higher than estimated, the void effect would be larger in absolute value by about 1 $.

Model variation	fuel temperature increased from 1200K to 2100K
Total void ($)	+2.34

Table 4.10: Variation of the total void effect with change of fuel temperature

This marked dependence implies that our assumption of using the same average temperature for the whole core, although convenient from a computational and modeling point of view, might be too rough and should therefore be taken into account in the computation of the uncertainties. It will be shown later on that taking into account the radial and axial fuel temperature distribution does have a strong influence on the void effect, even though the average fuel temperature might be the same, the distribution, and particularly the axial distribution considerably affects the behavior of the system (see Chapter 4.4).

Summary of uncertainties

The uncertainties outlined here are considerable, the void reactivity coefficient was estimated to be approximately equal to ~0±2.5$. This value does not include uncertainties related to approximations in the reactor model: instead of continuous axial variation of water density, a step-wise approximation for 4 axial zones was employed, the fuel/seed temperature was assumed to be constant, i.e. position independent.

The just discussed evaluations (which take into account the effect of fuel temperature, deviations between 2D and 3D models etc.) show that these approximations may shift the uncertainty in the void effect to a 3.5$, 4$. However, considering that the average uncertainty associated with these MCNP calculations is of about 75pcm (~0.25$), and that the uncertainties related to the cross section estimations, evaluations, and measurements can be as high as 100%, it is possible to conclude that the uncertainty range is of around ±5$. This value does not include effects related to possible trace amounts of minor actinides in the fuel and possible minor deviations in the plutonium vector.

Unless more refined data and models were applied and made available, in order to guarantee a negative void reactivity coefficient for the SCFR the calculated value for this parameter must be at least –5$. Such a value would take into account the current uncertainties associated with the different cross section sets, the model and the code approximations, and guarantee with adequate confidence its negativity.

Since, as observed, the presence of more moderator in the target blankets increases the number of captures significantly, a more heterogeneous core that could introduce more zirconium hydride, and therefore more solid moderator, is expected to improve the void reactivity. Another method would be to increase the leakage area, but because of the typical compactness of this reactor and the high operating pressure, this is not foreseen as an applicable solution.

Influence of absorbers on safety parameters

The design of the control rods and their arrangement goes beyond the scope of this work; furthermore, no literature was found giving details about possible configurations. Nonetheless, a new MCNP model was developed in order to investigate the effect of control rods assuming a cluster arrangement.

The chosen configuration accounts for approximately one control rod for every six fuel pins and one control rod cluster assembly every sixth fuel assembly. In order to keep a homogeneous distribution, this ratio has not been exactly respected as can be seen in Figure 4.10 and Figure 4.11 (the control rods are inserted from above).

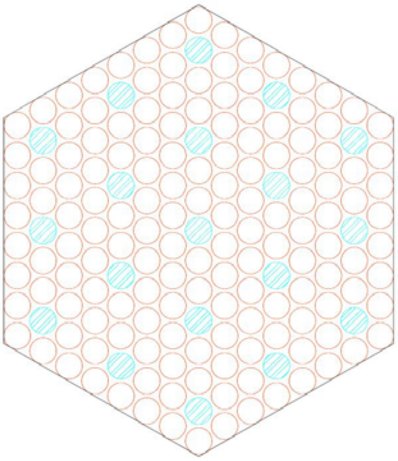

Figure 4.10: Control rod assembly

The control rods have been assumed to be composed of boron carbide sinterized powder (see /86/ and /87/ for a summary of the properties of boron carbide powders) with an average enrichment of Boron 10 of 90% /88/.

In Figure 4.10 the control rods are represented by the light blue pins, while in Figure 4.11 the control rod cluster assemblies are the ones represented by a black X.

Six calculations have been performed with different arrangements:

1. Control rods extracted, nominal conditions.

2. Control rods extracted, total void conditions.
3. 1/3 of the rod inserted, nominal conditions.
4. 1/3 of the rod inserted, total void conditions.
5. Full insertion, nominal conditions.
6. Full insertion, total void conditions.

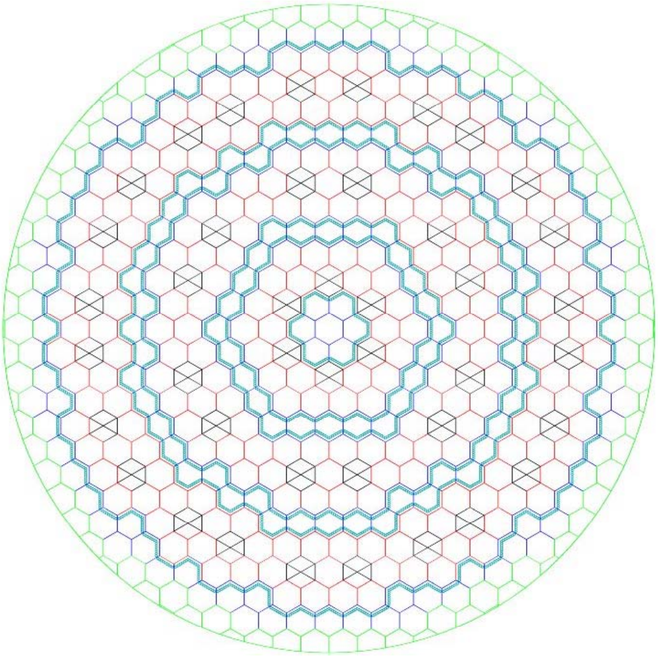

Figure 4.11: Control rod clusters distribution

The results are shown in Table 4.11, together with the differences with the standard model. The scram worth in nominal and total void conditions is of ~ –21$, which is about twice the worth usually considered appropriate for a light water reactor for safe shutdown conditions, which would eventually allow for a smaller enrichment of the boron carbide powder (provided the void effect is definitely negative).

Configuration	Rods are withdrawn	Rods are inserted: 1/3	Rods are fully inserted
k-eff	1.00096	0.99677	0.92795
Total void ($)	0.03	-1.53	+0.17

Table 4.11: Reactivity effects for the model with control rods

On the other hand the effect on k-effective of the empty fuel channels, which are left full of coolant when the control rods are withdrawn, is of minor importance (less than +0.5$ with all the rods completely extracted). This result is probably related to the higher water content in the seed in the wet state that increases both the initial k-effective and the void values. More detailed studies are, nonetheless, needed to investigate the optimal configuration/enrichment of the system in order to guarantee the wished criticality level of the reactor.

4.3 Optimization of safety parameters for the SCFR

As mentioned in the introduction, one of the desirable features of the SCFR could be the potential to be employed either for plutonium breeding or for incineration of the plutonium itself, together with minor actinides. In the present context of nuclear research, this aspect represents a most valuable incentive for the further development of this reactor, moreover, due to the relatively fast spectrum, there could be a potential to avoid the build up of curium, which is a typical drawback of MAs burning in LWRs.

On the other hand, the introduction of minor actinides and plutonium in a core has a negative influence on the safety parameters (as reported for instance by Maschek (2001) /89/). A well-known effect is e.g. the deterioration of the void effect particularly in presence of ^{241}Am, which undergoes fission in a fast spectrum and therefore introduces unwanted positive reactivity once the reactor is voided. The still uncertain sign of the void effect for the SCFR therefore gives rise to questions on its general safety; hence, further refinements of the void effect calculations are needed.

What our studies have outlined so far is that the SCFR presents new features that require a careful analysis of its neutronics safety parameters. The analyses described in Chapter 4.2 were based to a great extent on a computational model for a "continuous energy" Monte-Carlo code. A detailed representation of the SCFR core (i.e. specifying geometry and position of the inner - fuel/fertile/moderator - part of the pins, cladding, coolant, wrapper and other elements, such as fuel pin gaps, for each sub-assembly) was then implemented. Ideally, such a model may give an accurate value of a physical parameter, such as k-effective, provided that the nuclear data are accurate and the material and temperature distributions in the core are described correctly.

The results showed that, besides the detail of the adopted MCNP model, further investigations are needed, and that because of the uncertainties inherent to the computational model, to the cross section data libraries, and to the available calculation/modeling options, a conservative void coefficient of –5$ must be obtained in order to guarantee a negative void that takes into account all the estimated uncertainties.

Description of the new advanced MCNP model

The core of the SCFR is highly heterogeneous; hence the decision to use an MCNP model, which potentially allows the unique description of every single pin. The model that was used so far proved to give satisfactory results; however, the calculations relative to different configurations, e.g. control rods, outlined the importance of streaming effects for this relatively compact, fast, core, suggesting the need of a more detailed model.

Having this in mind, a more accurate model was developed. The main goal of this new model is to take into account the spacing among the sub-assemblies, a correct three-dimensional description of the upper, lower and radial reflector, and of the axial blankets, and to allow for more flexibility to define the physical properties of different areas of the reactor. Although the model adopted so far was based on a single pin discretization, the pins were not described one by one, but rather reproduced several times holding their original properties, and assigning a different position making use of the "universe" definition feature of the code[20].

Six different "universes" containing the six different geometries for the blanket assemblies, as represented in Figure 2.4, were used, another 3 different "universes" were used for the description of the 3 seed areas, which include the 12 different enrichment regions.

Another characteristic of relevance that was observed investigating the effect of the introduction of control rods was the high axial decoupling of the SCFR core. The insertion of 1/3 of the designed control rods from above did not affect the multiplicative constant of the core as expected (k-effective decreased from 1.00096 to 0.99677, corresponding to –419 pcm, while a full insertion introduces –7301 pcm). This pointed out the necessity of taking into account not only the correct geometrical description but also the correct density and temperature profiles of the materials used in the core, and in particular of the coolant.

Therefore, it was decided to increase the number of "universes" included in the calculations, allowing then the improvement of the detail of the description of the problem. In the new model, not only different universes were created to describe the different geometries, but also to take into account the different properties of the materials e.g. densities and temperatures, since MCNP cannot take into account continuous distributions of physical properties.

New MCNP input decks have then been run with different geometrical detail performing a rather extensive sensitivity analysis, using new cross section data files, and including the different files options as extensively described in Chapter 4.2

---

[20] A "universe" in MCNP is a macro-region with fixed determined geometry and physical properties, which can be reproduced to describe a uniform lattice.

(delayed neutrons, probability tables, and different models for hydrogen scattering). In addition to the nuclear data supplied with MCNP and based on the previous releases of the ENDF/B-VI, last year three additional data libraries were processed into the MCNP format, the libraries being ENDF/B-VI, release 7 (ENDF/B-VI.7), JEF-2.2, and JENDL-3.2. Recently the newest releases of these libraries were also processed and compared: ENDF/B-VI.8, JEFF-3.0, and JENDL-3.3.

Description of the calculations and results

The first set of calculations investigated the effect of the introduction of an additional radial cell that would represent the radial reflector[21]. In the calculations performed so far only the active core and a thin fill up region was considered.

Table 4.12 shows the results relative to a region restricted only to the active core and relative to a full radial reflector. The spacing among the sub-assemblies is neglected (gap=0). The introduction of the reflector does not improve our void effect because of the expectable flatter power distribution and the consequent reduction of radial leakage and the inclusion of fast fission from the external blanket ring, which is not properly considered with boundary conditions set on the periphery of the blanket assemblies themselves. On the other hand the difference between the two full void k-effectives is equal to 96 pcm, which is within the overall uncertainty range (for the nominal condition case the difference is of only 40 pcm).

R = 1.75m (no reflector)		**H2O ☒N P D ZrH**	
gap=0 mm	*k-eff*	*[pcm]*	*[$]*
Nominal	0.98057±50pcm	0	0
Total Void	0.96980±48pcm	-1133	-3.1

R=2.2m (includes reflector)		**H2O ☒N P D ZrH**	
gap=0 mm	*k-eff*	*[pcm]*	*[$]*
Nominal	0.98017±62pcm	0	0
Total Void	0.97076±76pcm	-989	-2.7

Table 4.12: Effect of radial reflector[22]

This geometry, which includes the reflector, was taken as a reference since it corresponds more closely to the real geometry of the system and starting from it a second more extended sensitivity analysis was performed.

In order to improve the accuracy of the model, the effect of the introduction of coolant axial profiles was carefully investigated. Since at this stage of the work the coupled

---

[21] Cold coolant was used to describe the reflector simulating the core baffle (see Figure 1.2). The average water density is therefore ~ 720 kg m^{-3} and the thickness is ~ 0.45 m.

[22] All calculations, unless otherwise specified, relative to a fuel average temperature of 1200K, a blanket average temperature of 800K, axial and radial fuel enrichment profiles, but no temperature or density profiles, and ENDF/B-VI.7 data library.

fluid dynamic/Monte-Carlo-based-neutronics system was not available, a cosinusoidal axial power shape was assumed and hence the relative coolant density profile was calculated. These results are relevant beyond the accuracy of the power profile since they provide a basis for the choice of the number of cells to be used in the coupled model.

In fact, one of the main well known drawbacks of MCNP is the so called cell approximation; because of the mentioned absence of continuous temperature treatment and density feedbacks, the functions describing these parameters need to be defined step wise introducing an obvious error that can be observed in the following figures (Figure 4.12 ÷ Figure 4.15).

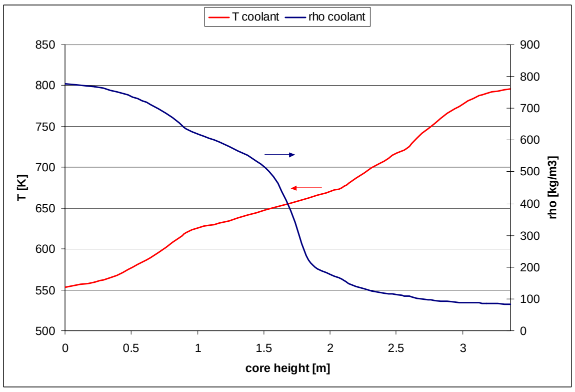

Figure 4.12: Coolant profile continuous distribution

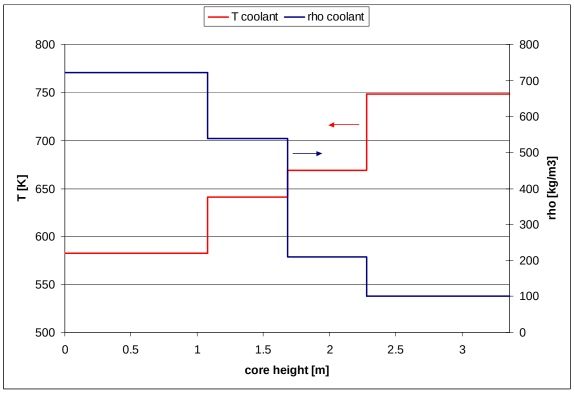

Figure 4.13: 4 axial cell coolant profile distribution

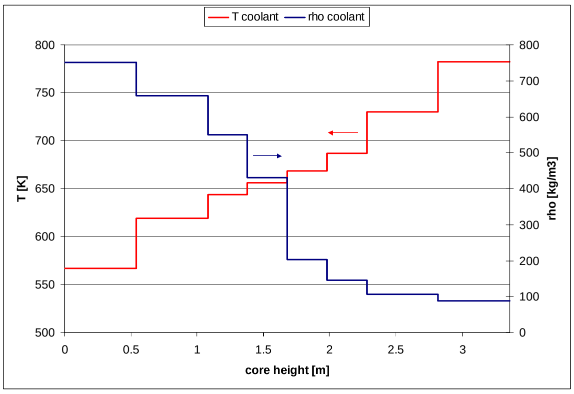

Figure 4.14: 8 axial cell coolant profile distribution

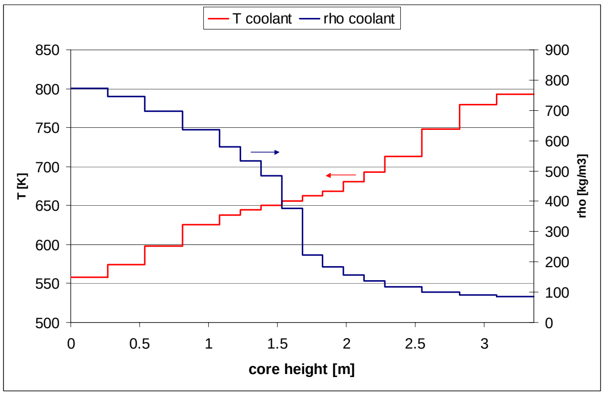

Figure 4.15: 16 axial cell coolant profile distribution

Given the difficulty to decide a priori the ideal number of cells, 5 calculations were performed considering 1, 4, 8, 16, and 20 axial cells, with the shown distributions. The results are summarized in Table 4.13.

4 meshes		**H2O ☒**	**P D ZrH**
gap=0 mm	*k-eff*	*[pcm]*	*[$]*
Nominal	0.98276±57pcm	0	0
Total Void	0.97039±56pcm	-1297	-3.5

8 meshes		**H2O ☒**	**P D ZrH**
gap=0 mm	*k-eff*	*[pcm]*	*[$]*
Nominal	0.98281±58pcm	0	0
Total Void	0.97105±51pcm	-1232	-3.3

16 meshes		**H2O ☒**	**P D ZrH**
gap=0 mm	*k-eff*	*[pcm]*	*[$]*
Nominal	0.98240±64pcm	0	0
Total Void	0.96998±49pcm	-1303	-3.5

20 meshes		**H2O ☒**	**P D ZrH**
gap=0 mm	*k-eff*	*[pcm]*	*[$]*
Nominal	0.98339±48pcm	0	0
Total Void	0.97145±49pcm	-1250	-3.4

Table 4.13: Effect coolant axial meshing

The 16 mesh input deck was taken as a reference for the following calculations, since k-effective is not changing significantly once any number of axial profiles is introduced. A few calculations with 20 meshes were also performed since the SIMMER (TWODANT) model is based on a 20 axial mesh profile and therefore comparisons and data transfer from model to model could be performed more easily.

The analyses showed that a 1 single axial mesh description introduces an error of at least 0.4$, indicating a better behavior of the core during void transients and the importance of the fluid-dynamics/neutronics coupling work that is being performed.

Another important geometrical detail that was neglected in the model adopted so far is the spacing among the subassemblies. The gap distance indicated in the original design is of 1mm; in view of the fact that the mechanical tolerance required to achieve this value could result being too strict, calculations were also performed for a 2mm gap[23]. The differences in the geometrical detail and the proportion between gap and subassembly dimensions can be appreciated in Figure 4.16, Figure 4.17, and Figure 4.18, while Figure 4.19 shows the details of the lower blanket and lower reflector region. The axial blankets configuration was reproduced in detail pin-wise and not as a blanket material slab, as it was done in the geometrical model adopted at the beginning.

The results relative to the different gap dimension are shown in Table 4.14.

Gap = 1 mm		**H2O ☒**	**P D ZrH**
16 meshes	*k-eff*	*[pcm]*	*[$]*
Nominal	0.98100±51pcm	0	0
Total Void	0.97064±47pcm	-1088	-2.9

Gap = 2 mm		**H2O ☒**	**P D ZrH**
16 meshes	*k-eff*	*[pcm]*	*[$]*
Nominal	0.97894±59pcm	0	0
Total Void	0.96937±53pcm	-1008	-2.7

Table 4.14: Effect of subassembly spacing

---

[23] The gap was filled with coolant with the same properties of the reflector.

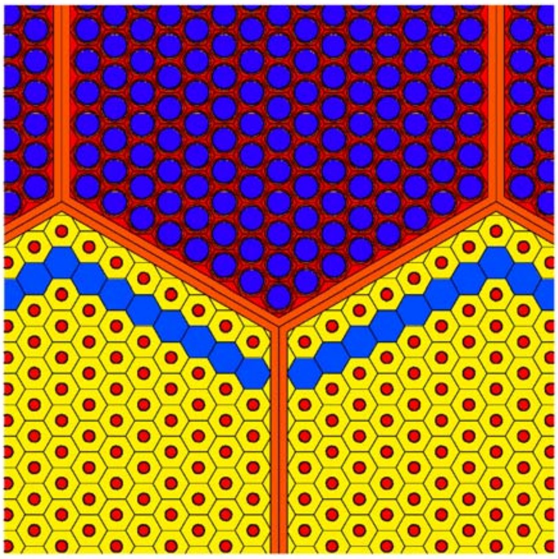

Figure 4.16: Detail of the seed/blanket boundary (0 mm gap spacing)

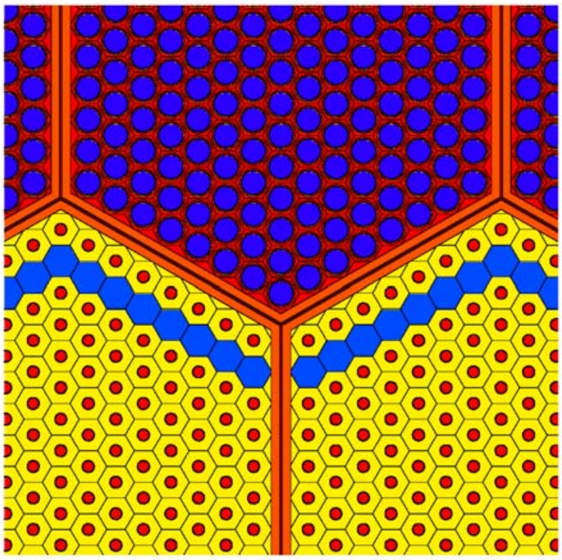

Figure 4.17: Detail of the seed/blanket boundary (1 mm gap spacing)

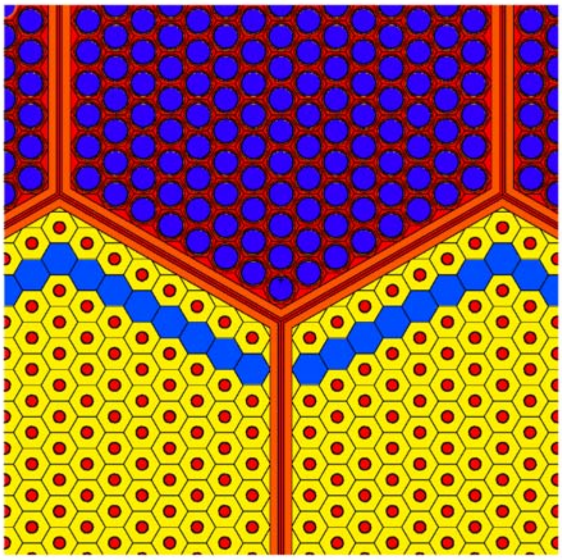

Figure 4.18: Detail of the seed/blanket boundary (2 mm gap spacing)

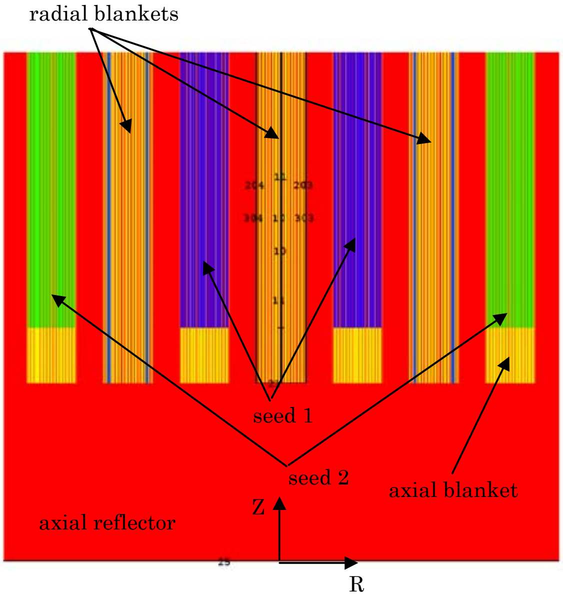

Figure 4.19: Detail of the lower blanket and lower reflector region

Different concurring phenomena contribute to the higher or lower efficiency of the analyzed geometries. The introduction of a gap is expected to affect negatively the k-effective because of the introduction of more water which acts more as an absorber rather than a moderator, and this is what actually happens, on the other hand, the void effect changes without a specific trend. The k-effective of the SCFR core under voided conditions decreases with increasing gap spacing, because of a higher leakage fraction. However, this effect is counteracted by a greater reduction of the nominal k-effective, which therefore, worsens the void effect for the 2mm gap case. The 1mm geometry gives a better void positively combining the two mentioned effects.

The effect of the introduction of these modeling details varies significantly once the new details are considered at once as described in the following paragraphs.

New, improved void effect blanket

The results obtained with a new model including: reflector, subassembly spacing, coolant density axial profiles, and detailed axial blanket description, prove that the SCFR core has a potentially negative void coefficient. Nevertheless, it was argued before that, all uncertainties taken into account, a negative void of –5$ should be calculated in order to guarantee a negative void in all conditions, although still assuming a Beginning Of Cycle fuel composition. With the aim of improving the void reactivity coefficient further, a new blanket geometry was then devised.

Having this in mind, a tight blanket configuration that could increase the number of captures shielding the seed areas from the neutrons was tested.

The introduction of a reasonable subassembly gap spacing did not improve the void effect, and it pointed out that in a voided reactor fast neutrons that stream through the spacing contribute significantly to the reactivity level of the reactor "seeing" more seed zones, that is the relative number of neutrons inducing fission is higher than the leakages.

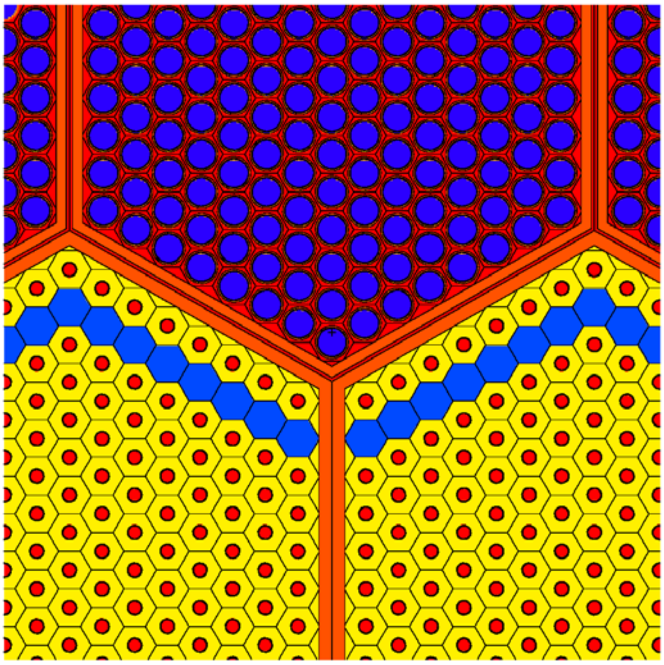
Figure 4.20: Improved void blanket configuration

In Figure 4.20 this concept is shown in detail; it is here possible to observe the configuration of the tight lattice arrangement: the spacing among the seed sub-assemblies and among the seed and the blanket sub-assemblies is kept at the design value (1 mm or 2 mm), while the blanket sub-assemblies are tightly arranged adopting a thicker can wall (in this case the gap spacing among blanket subassemblies is 0 mm).

This solution should prove feasible from the construction point of view since it allows thermal expansions in the radial and in the axial directions, however, the effect of longitudinal expansion, which could jeopardize this specific core configuration, should be investigated further.

The estimate of this effect was not performed, as it is beyond the contractual work and it would require the support of a designer.

The results relative to this core arrangement are discussed in the following paragraphs together and compared to the void effect reactivity worth calculated for the original core design.

Void effect calculations with tight blanket geometry

ORIGINAL DESIGN				*TIGHT BLANKET DESIGN*			
Gap = 0 mm		**H2O ☒N P D ZrH**		**Gap = 0 mm**		**H2O ☒N P D ZrH**	
16 meshes	*k-eff*	*[pcm]*	*[$]*	*16 meshes*	*k-eff*	*[pcm]*	*[$]*
Nominal	0.98240±64pcm	0	0	Nominal	0.98212±57pcm	0	0
Total Void	0.96998±49pcm	-1303	-3.5	Total Void	0.97113±44pcm	-1152	-3.1
Gap = 1 mm		**H2O ☒N P D ZrH**		**Gap = 1 mm**		**H2O ☒N P D ZrH**	
16 meshes	*k-eff*	*[pcm]*	*[$]*	*16 meshes*	*k-eff*	*[pcm]*	*[$]*
Nominal	0.98100±51pcm	0	0	Nominal	0.98036±64pcm	0	0
Total Void	0.97064±47pcm	-1088	-2.9	Total Void	0.96582±47pcm	-1536	-4.2
Gap = 2 mm		**H2O ☒N P D ZrH**		**Gap = 2 mm**		**H2O ☒N P D ZrH**	
16 meshes	*k-eff*	*[pcm]*	*[$]*	*16 meshes*	*k-eff*	*[pcm]*	*[$]*
Nominal	0.97894±59pcm	0	0	Nominal	0.97808±53pcm	0	0
Total Void	0.96937±53pcm	-1008	-2.7	Total Void	0.96149±54pcm	-1764	-4.8

Table 4.15: Void effect calculations for tight blanket lattice design

All the results shown in Table 4.15 were obtained with the same calculation option indicated in Table 4.12 (16 coolant density axial profiles in the seed regions, ENDF/B-VI.7 and so on). The effect of gap spacing for the original arrangement has already been discussed. In the case of the improved void blanket configuration the effect of subassembly gap spacing is the opposite, actually improving the void coefficient.

For the basic arrangement, with no subassembly spacing, the void effect does not change significantly, as expected. The difference of 0.4$ can be attributed mostly to statistical uncertainties. The situation changes significantly with larger gap sizes. The void reactivity worth improves by –1.3$ with a 1mm gap and by –2.1$ with a 2 mm gap. Nominal k-effectives are lower for the tight lattice configurations because of the high capture cross section of nickel that is replacing water around the blankets. Voided condition k-effective values are also lower because of the combined effect of captures in the can wall, and more captures in the blankets due to a reduction of radial streaming.

The void effect then, for a tight blanket configuration and a 2mm subassembly gap spacing, is for ENDF/B-VI.7 –4.8$, close to the –5$ that is the target value of this study.

Effect of the adoption of the new cross section libraries

The ongoing evaluation process and the development of new theoretical models for the estimation of cross sections recently resulted in the release of new versions of the cross section libraries mentioned in Chapter 4.2.

Version 8 of ENDF/B-VI was released in 2002 by RSICC providing reviewed data for several nuclides and replacing ENDF/B-VI.7, JENDL-3.3 was also released in 2002 by JAERI replacing JENDL-3.2, and JEFF-3.0 (Joint Evaluated Fission and Fusion General Purpose File) was released by the NEA data bank in April 2002 and supersedes JEF-2.2, JEF-1 and EFF-2.4.

Taking as a reference the MCNP model that was described in the previous paragraphs the calculations were repeated applying the new and the older releases of the available data files; the results, relative to the tight blanket configuration, are reported in Table 4.16.

As outlined earlier in Chapter 4.2, data in nuclear data libraries may differ significantly. Each evaluation may have advantages and disadvantages, the differences reflecting evaluator's strategies in attributing priorities to different experimental results and employing different fitting techniques. Therefore, results obtained with different libraries may reflect to a certain degree the existing uncertainties in nuclear data. However, the uncertainty of the void effect cannot be derived in a straightforward manner from the computations with ENDF, JEF, JENDL: in many cases the latest sophisticated experiments have the highest level of credibility. On the other hand the nuclear data libraries may contain similar errors that may increase (e.g. by a factor of 2) the level of uncertainties that could be estimated by considering deviations between the computed figures.

The adoption of newer data libraries should decrease the uncertainties inherent with the evaluation of the library itself (e.g.: improvement of the experimental techniques, of the fitting techniques, availability of new data), but does not cancel the differences among the different strategies followed by different groups of evaluators.

ENDF/B-VI.7		**H2O ~~N~~ P D ZrH**		**ENDF/B-VI.8**		**H2O ~~N~~ P D ZrH**	
16 meshes	*k-eff*	*[pcm]*	*[$]*	*16 meshes*	*k-eff*	*[pcm]*	*[$]*
Nominal	0.97808±53pcm	0	0	Nominal	0.97783±55pcm	0	0
Total Void	0.96149±54pcm	-1764	-4.8	Total Void	0.96195±52pcm	-1688	-4.6
JENDL-3.2		**H2O ~~N~~ P D ZrH**		**JENDL-3.3**		**H2O ~~N~~ P D ZrH**	
16 meshes	*k-eff*	*[pcm]*	*[$]*	*16 meshes*	*k-eff*	*[pcm]*	*[$]*
Nominal	0.97151±54pcm	0	0	Nominal	0.97529±51pcm	0	0
Total Void	0.95250±52pcm	-2054	-5.6	Total Void	0.95357±48pcm	-2335	-6.3
JEF-2.2		**H2O ~~N~~ P D ZrH**		**JEFF-3.0**		**H2O ~~N~~ P D ZrH**	
16 meshes	*k-eff*	*[pcm]*	*[$]*	*16 meshes*	*k-eff*	*[pcm]*	*[$]*
Nominal	0.96778±48pcm	0	0	Nominal	0.97354±55pcm	0	0
Total Void	0.94726±44pcm	-2238	-6.0	Total Void	0.95167±47pcm	-2361	-6.4

Table 4.16: ENDF/B-VI.7 vs. 8 - JENDL-3.2 vs. 3.3 - JEF-2.2 vs. JEFF-3.0

The results shown in Table 4.16 give a good example of what was just discussed. The difference of the void reactivity coefficient between the older and the newer cross section file for the same library evaluation group are approximately in the range of the statistical uncertainty of the Monte-Carlo calculations, although certainly the application of newer data has a significant effect on the results that will be discussed in the following paragraphs (the biggest difference can be appreciated for JENDL and can be attributed partially to the water data that was not available for JENDL-3.2 for the average coolant density and had to be substituted with JENDL-3.3 data and 1000K thermal scattering file).

Table 4.17 summarizes the differences in pcm among k-effectives relative to the old and the new data files. It is worth outlining the fact that for the application here of interest the new release of ENDF/B does not seem to have a significant influence on the absolute results, while more appreciable discrepancies can be noticed for both JEF and JENDL.

Δ k-effective [pcm]	Nominal	Voided
ENDFB-6.7 vs. ENDFB-6.8	25	-46
JEF-2.2 vs. JEFF-3.0	-378	-107
JENDL-3.2 vs. JENDL-3.3	-576	-441

Table 4.17: K-effective comparison among the adopted data files (old vs. new versions)

The following figures (Figure 4.21 ÷ Figure 4.25) compare the new libraries with their older version, ^{239}Pu absorption, fission and total cross section were considered, since this isotope is the main fissile element of the SCFR core. The scales of these figures may vary, since different evaluations may cover different energy ranges.

As it could be expected, there are no noticeable differences between ENDF/B-VI.7 and ENDF/B-VI.8, Figure 4.21. Total, absorption, elastic, fission cross sections were examined carefully in different energy ranges and no differences could be noticed, here the total cross section is shown for both versions of the library.

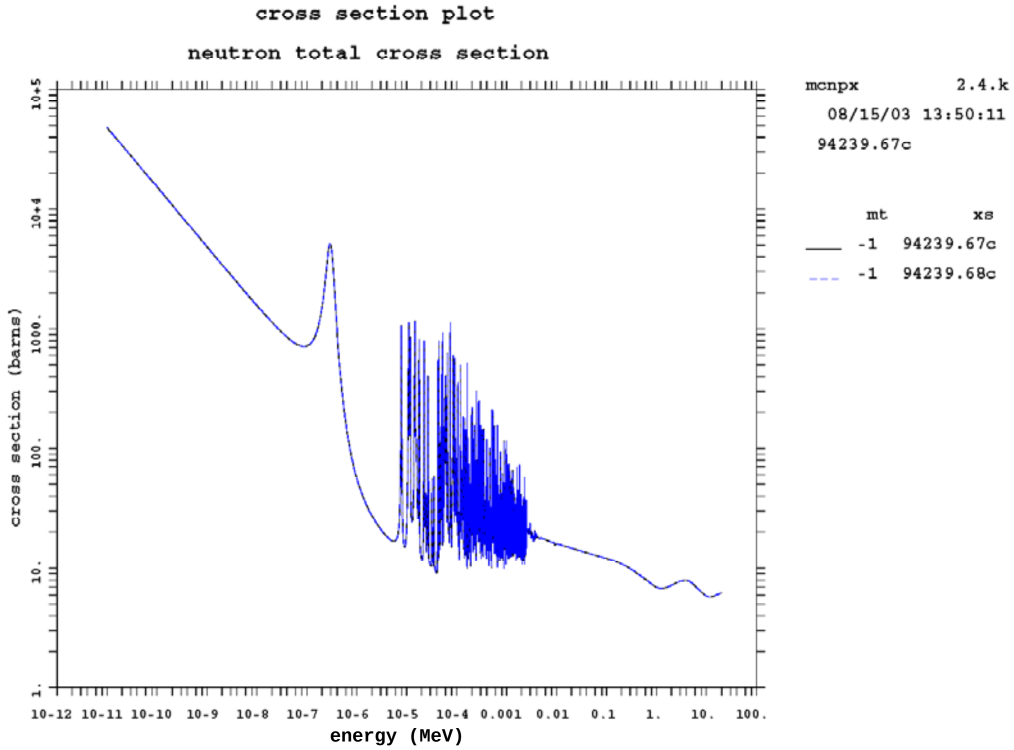

Figure 4.21: ^{239}Pu total cross section ENDF/B-VI.7 (67c) vs. ENDF/B-VI.8 (68c)

Figure 4.22 illustrates the difference for the absorption cross section between JENDL-3.2 and JENDL-3.3. This specific cross section was chosen because it showed the biggest deviations between the two files, especially for the high-energy range. The shown discrepancies however are not enough to account for the observed variations of k-effective, a more accurate study for all the isotopes involved in the calculation should hence be performed for all the relative cross sections, in order to understand which were the main improvements in JENDL-3.3 with respect to JENDL-3.2.

Finally, Figure 4.23 depicts the difference for the total cross section between JEF-2.2 and JEFF-3.0. This specific cross section is the one that shows the greatest variation from one file to another. Figure 4.24 and Figure 4.25 show the absorption and the fission cross section comparison for these files respectively. Besides the differences in the absorption cross section file, what strikes most is the lower setting of the fission cross section file, which helps to explain the lower k-effective estimated for both nominal and voided reactor conditions.

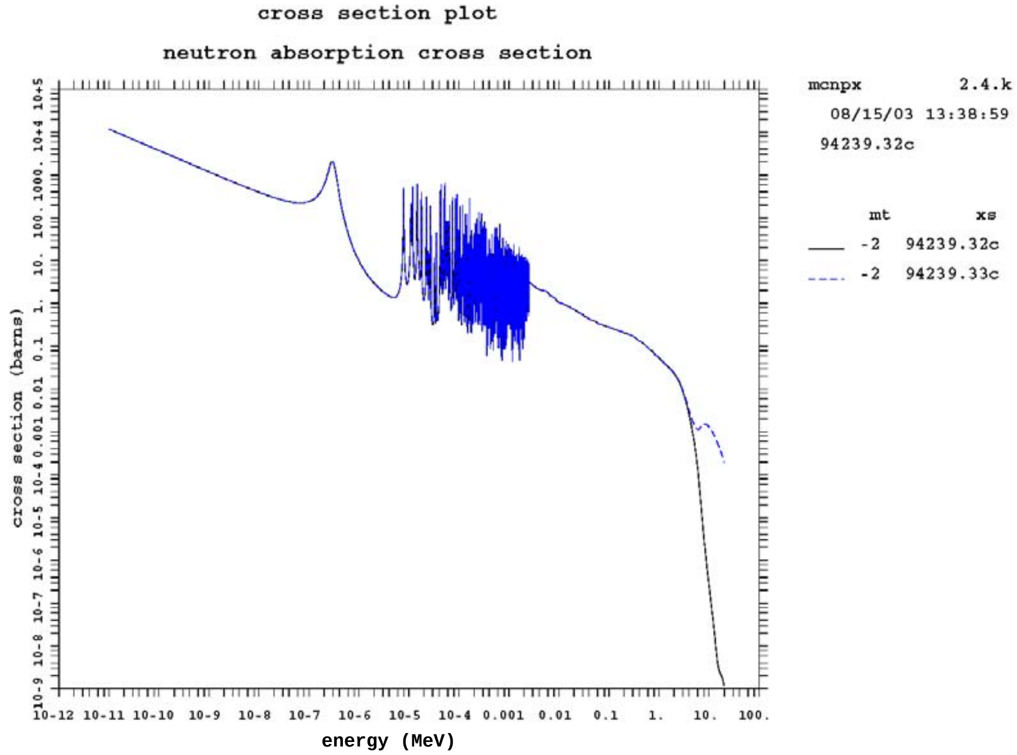

Figure 4.22: ^{239}Pu absorption cross section JENDL-3.2 (32c) vs. JENDL-3.3 (33c)

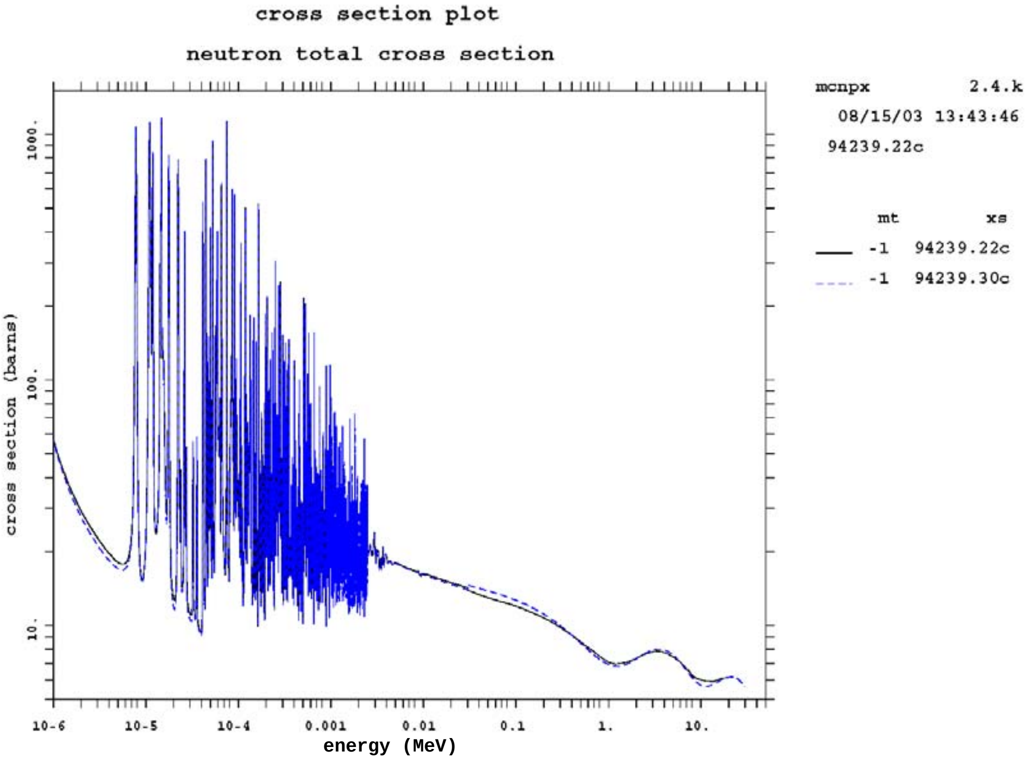

Figure 4.23: ^{239}Pu total cross section JEF-2.2 (22c) vs. JEFF-3.0 (30c)

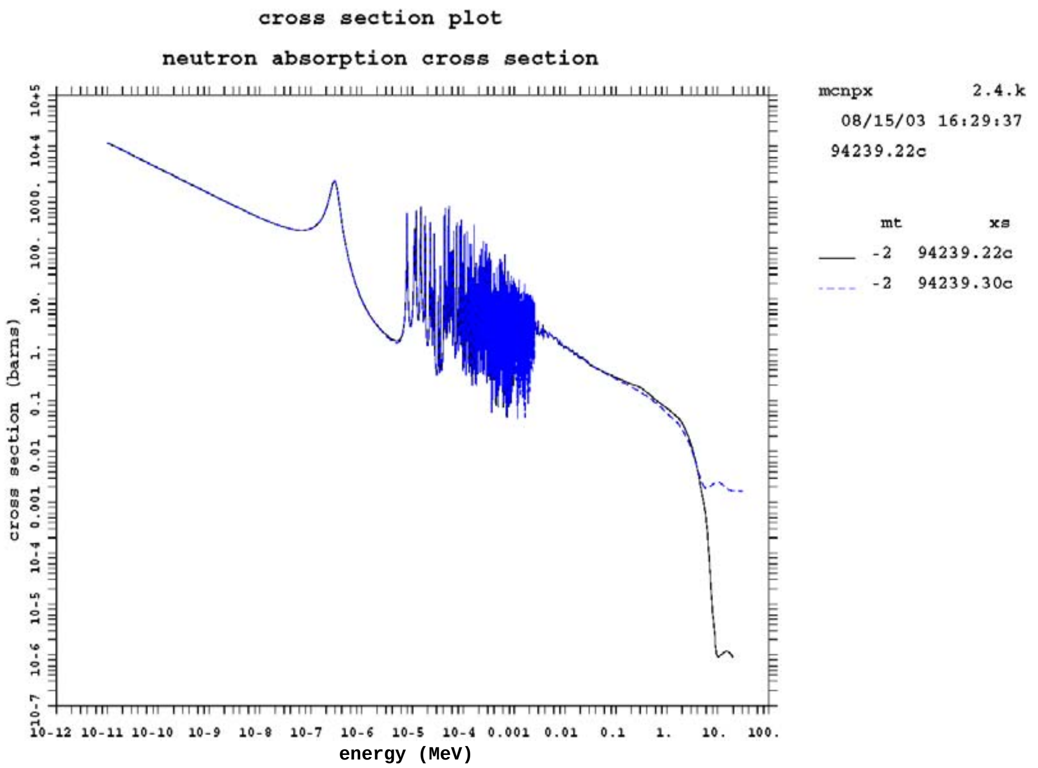

Figure 4.24: ^{239}Pu absorption cross section JEF-2.2 (22c) vs. JEFF-3.0 (30c)

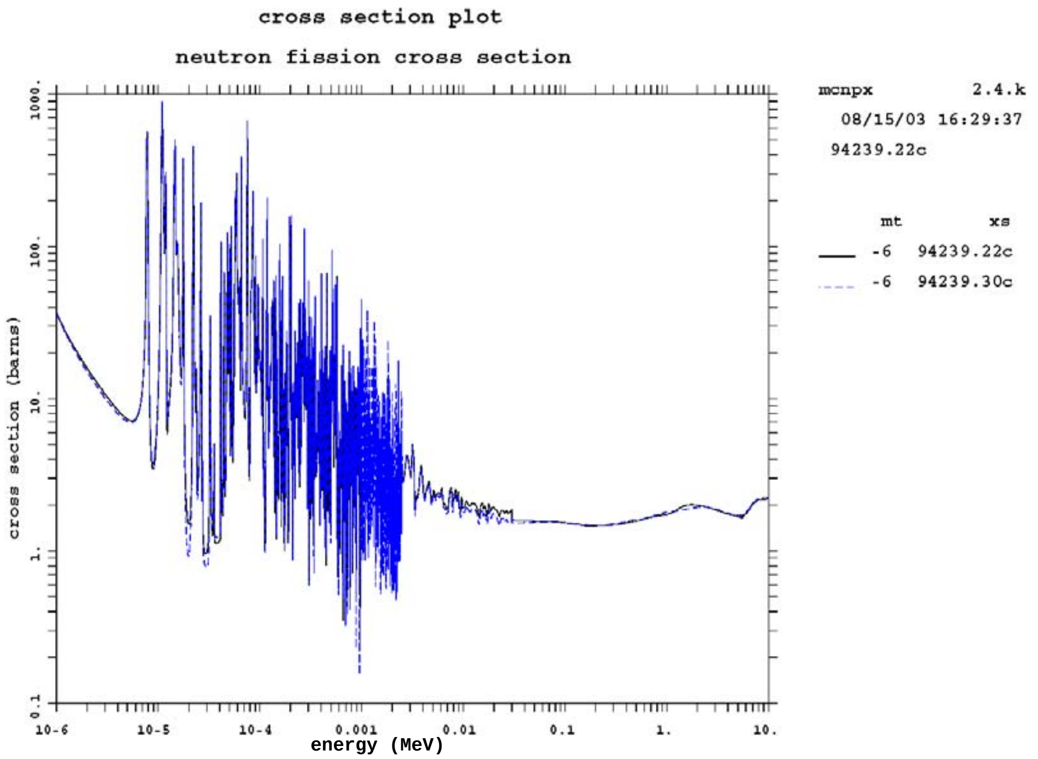

Figure 4.25: ^{239}Pu fission cross section JEF-2.2 (22c) vs. JEFF-3.0 (30c)

Effect on void effect of the adoption of the new cross section libraries

As discussed, JEFF and JENDL give a very close estimate of the void reactivity effect and of the k-effective for the examined reactor conditions. The biggest differences, in the order of ~2$, can be observed between JEF and ENDF/B, and consequently between JENDL and ENDF/B.

Taking a close look at the evaluated k-effectives, it is worth noting the coherence in the evaluation of the nominal k-effective for the new cross section files. Table 4.18 summarizes the differences among the calculated k-effectives for nominal and voided conditions, and for all the adopted data files.

Nominal Voided	k-effective difference [pcm]	Nominal Voided	k-effective difference [pcm]
ENDFB-6.7 vs. JENDL-3.2	657 899	ENDFB-6.8 vs. JENDL-3.3	254 838
ENDFB-6.7 vs. JEF-2.2	1030 1423	ENDFB-6.8 vs. JEFF-3.0	429 1028
JEF-2.2 vs. JENDL-3.2	373 524	JEFF-3.0 vs. JENDL-3.3	175 190

Table 4.18: K-effective comparison among the adopted data files (cross differences)

For nominal conditions, the calculated difference for the new cross section libraries among the estimated k-effectives is approximately half of the value calculated with the old files (in the range of 0.5÷1.2$). For voided conditions, the difference is comparable to the old values except for JEFF-3.0 vs. JENDL-3.3, for which the difference is about 5 times smaller and comparable to the one relative to the nominal conditions (~0.5$). In conclusion, as observed in the course of the work performed with the previous versions of the mentioned libraries, ENDF/B-VI gives the most conservative results for the specific composition and spectrum of interest of the SCFR.

As discussed introducing the model improvements and the new design features, a void worth of about –5$ was achieved, overcoming the estimated uncertainty effect. The adoption of new libraries and of a more sophisticated MCNP geometry, have the outcome of improving the confidence interval of the estimates. However, the only way to reduce the uncertainty would be to take into account a representative set of experimental results relevant for the considered reactor design and physical parameters. These analyses could be eventually foreseen for the next stage of the work. In particular, a specific evaluation of the thermal scattering matrices for supercritical water should be performed. The scattering model used in this study is relative to “liquid” water at the average temperature of 800K. The effect of the density distribution is taken into account adopting the solution illustrated in the previous paragraphs. On the other hand, the effect of the different aggregation status of the coolant on the scattering kernel cannot be solved via input options, but needs a dedicated cross section file evaluation. The material that defines the water coolant in the MCNP model uses then a free gas treatment corrected by the thermal data S(α,β).

Investigation of the adoption of new core configurations and materials

The adoption of the tight blanket configuration illustrated in Figure 3.8 significantly improved the void effect achieving a value of –4.8$ for ENDF/B-VI.7. This result is very close to the target value that was set to overcome the discussed uncertainties, however, more analyses were conducted in order to investigate the possibility to further increase the safety margin, having in mind the possible introduction of minor actinides in the core.

Effect of lower blanket removal and denser solid moderator

One of the solutions that are often recommended to prevent recriticalities in fast reactors in case of core melting and reconfiguration of the fissile material is the removal of the lower blanket. Given the possible improvement of neutron axial streaming, the void effect was estimated for this core configuration also.

The model used is equivalent to the one described in Table 4.15 for the improved void calculations, the lower blanket portion of the pins was replaced by a fission gas lower plenum filled with helium and steel representing the positioning spring coil. The results are shown in Table 4.19.

NO lower blanket, gap =2mm		**H2O** **~~N~~**	**P** **D** **ZrH**
16 meshes	*k-eff*	*[pcm]*	*[$]*
Nominal	0.98034±62pcm	0	0
Total Void	0.96133±55pcm	-2017	-5.5

Table 4.19: Lower blanket removal

The removal of the lower blanket improves further our void coefficient. The nominal k-effective increases by about 200pcm because of the lower number of captures and the better reflective property of water. In the lower part of the SCFR core the neutron spectrum is well thermalized therefore the contribution of the blanket to fast fissions is very low if compared to the number of captures. In case of a fully voided reactor, k-effective decreases again for the configuration without lower blanket, but not significantly. It is possible to conclude then that the effect of the lower blanket is mainly to absorb neutrons both in nominal and in voided conditions, therefore breeding plutonium through captures in ^{238}U. The void effect reactivity worth for this core arrangement calculated with ENDF/B-VI.8, which proved to be the most conservative library for this reactor, is then of –5.5$ therefore well beyond the goal of –5$.

Advanced heterogeneous models ("flower models")

The effect of zirconium hydride, as explained before, is to ensure the presence of a moderating material in the event of a coolant loss. Neutrons that are moderated close to the blanket regions are then more easily captured by ^{238}U. Different core configurations were therefore examined in order to increase the number of captures in the event of a loss of coolant. The strategy adopted for these new core designs is based on the introduction of more heterogeneity and more solid moderator ($ZrH_{1.7}$). The overall number of blanket/seed sub-assemblies and their ratio was kept constant in order to maintain approximately the same core inventory and the same breeding/burning capabilities, accordingly to the contract restrictions.

Three configurations were studied (see Figure 4.26, Figure 4.27, and Figure 4.28). Several calculations were performed applying the available MCNP models: the original 3D model, and the newest model described and analyzed in these last paragraphs.

The first trial calculation performed for the geometry illustrated in Figure 4.26 showed that, quite surprisingly at first, this core design actually makes the void coefficient strongly positive.

This behavior is to be attributed to the overall homogeneity of this arrangement. The driver and blanket areas are more uniformly distributed and do not perform the desired function. Neutrons can travel freely in the core and the shielding role of the radial blankets is lost, furthermore, the allocation of the zirconium hydride layers, almost uniformly spread, throughout the core weakens the neutron energy spectrum altering the unique design characteristics of the SCFR.

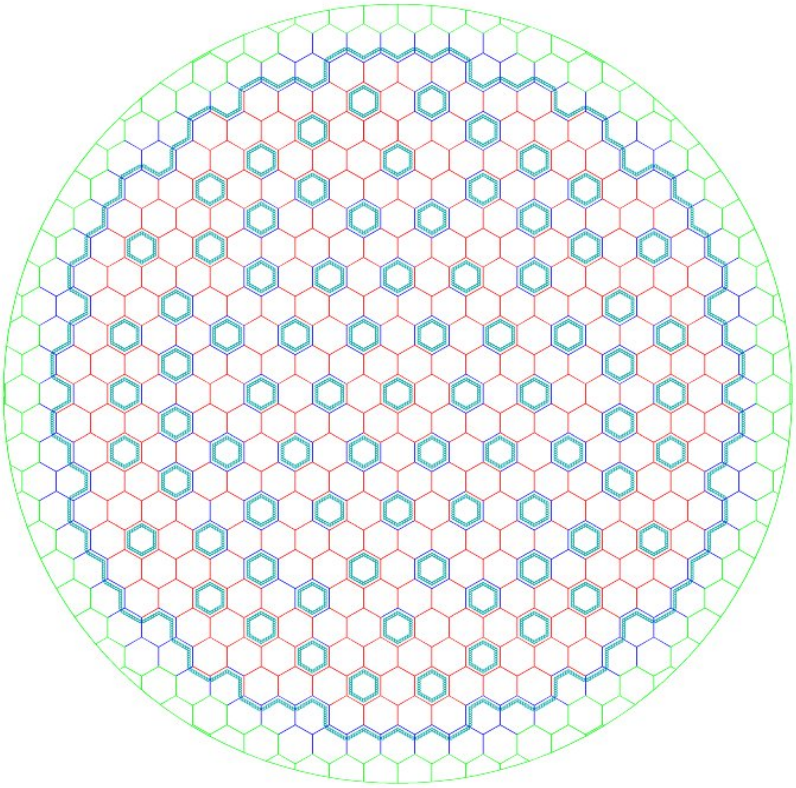

Figure 4.26: Enhanced zirconium hydride model

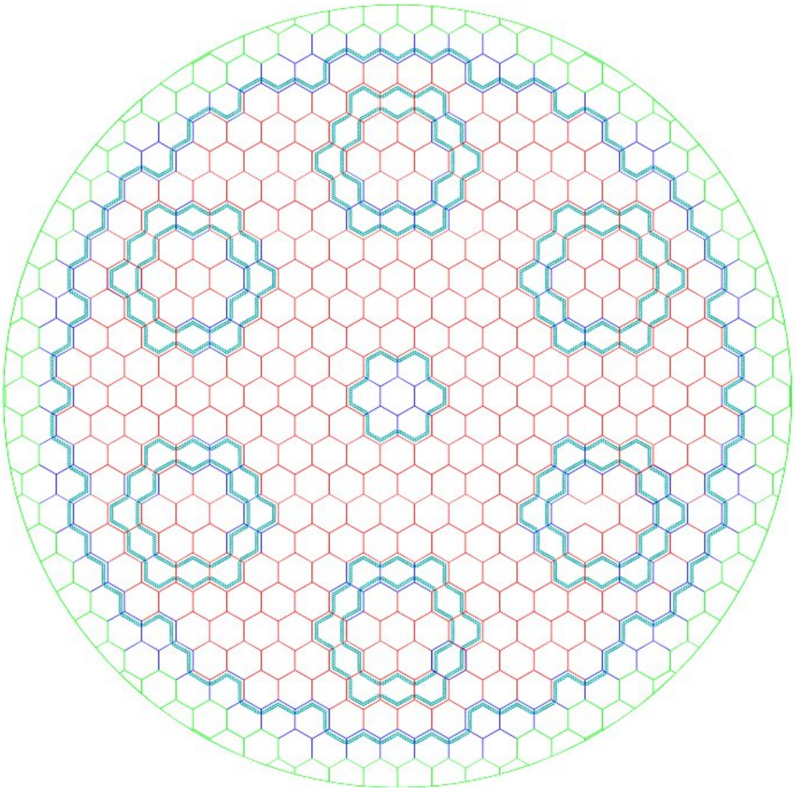

Figure 4.27: Advanced heterogeneous model (peripheral clusters)

Given the result of the configuration shown in Figure 4.26, the designs shown in Figure 4.27 and Figure 4.28 were developed in an attempt to create separate regions in the core and to redistribute the neutron flux more conveniently in order to increase the number of captures and the leakage in voided reactor conditions. These two new core configurations should achieve this effect increasing the heterogeneity effects and therefore improving the void worth, because of their characteristics shape they were denominated "flower models".

As in the case described in Figure 4.26, the design reported in Figure 4.27 did not give the expected results. The arrangement of the blanket "petals" is such that a strongly peaked center flux distribution results in this core. At the same time the shielding effect of the blanket regions is reduced because of their peripheral positioning and therefore the leakages from the seed to the blanket regions and to the outside are not augmented as initially desired.

Taking these considerations into account the blanket "petals" were then moved towards the center of the core (see Figure 4.28). This pattern increases the importance of neutrons at the core periphery, which in case of voided conditions enhances the radial leakage towards the outer core and towards the shielded blanket areas, therefore increasing the number of captures and neutron losses.

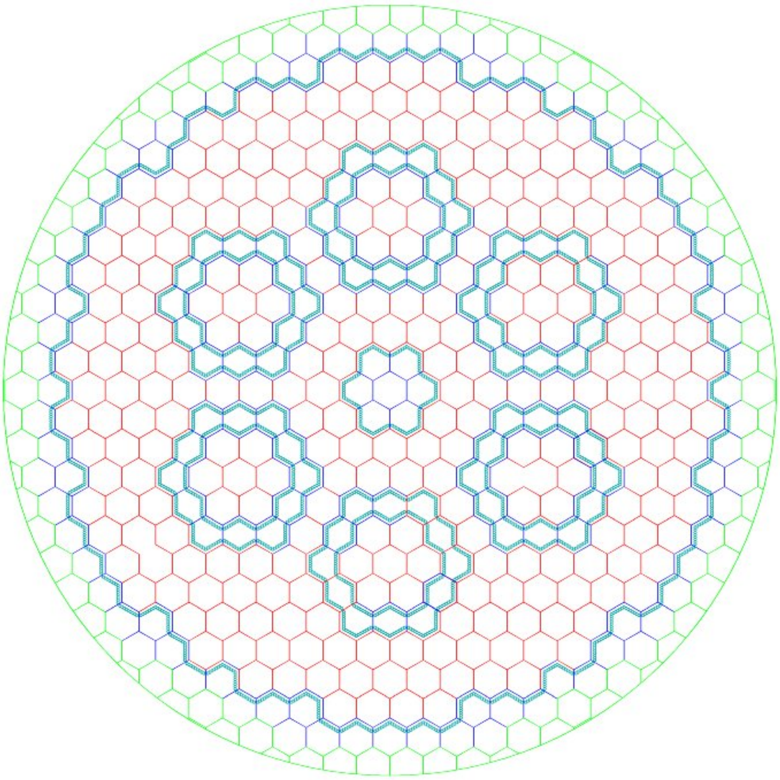

Figure 4.28: Advanced heterogeneous model (central clusters)

The results of the calculations relative to this geometry are given in Table 4.20. K-effective was determined using the options specified in the table itself, and the firstly developed 3D MCNP model. The introduction of this peculiar core configuration enhanced indeed the void effect for the SCFR by about 370 pcm, therefore improving the void effect from –0.5$ to –1.5$. On the other hand, this result was obtained with a model that although comprehensive and sufficiently accurate lacked a truly detailed description of geometrical and physical characteristics that proved to affect the void reactivity worth significantly.

<table>
<tr><th colspan="2">3D MODEL</th><th>H2O</th><th>~~N~~</th><th>P</th><th>D</th><th>ZrH</th></tr>
<tr><td><i>ENDFB6.7</i></td><td><i>k-eff</i></td><td><i>[pcm]</i></td><td colspan="4"><i>[$]</i></td></tr>
<tr><td>Nominal</td><td>0.99936±62pcm</td><td>0</td><td colspan="4">0</td></tr>
<tr><td>Total Void</td><td>0.99761±60pcm</td><td>-176</td><td colspan="4">-0.5</td></tr>
<tr><th colspan="2">3D “FLOWER” MODEL</th><th>H2O</th><th>~~N~~</th><th>P</th><th>D</th><th>ZrH</th></tr>
<tr><td><i>ENDFB6.7</i></td><td><i>k-eff</i></td><td><i>[pcm]</i></td><td colspan="4"><i>[$]</i></td></tr>
<tr><td>Nominal</td><td>1.01779±68pcm</td><td>0</td><td colspan="4">0</td></tr>
<tr><td>Total Void</td><td>1.01214±65pcm</td><td>-548</td><td colspan="4">-1.5</td></tr>
</table>

Table 4.20: Advanced heterogeneous model: results for the original model

The calculations were then repeated adopting an average 16 axial coolant density profiles, radial reflector and sub-assembly gap spacing, the results are shown in Table 4.21, where void effect was calculated for the three examined sub-assembly gap spacing.

The combined effect of the core rearrangement and of the introduction of more precise details in the model did not improve the void effect as it occurred with the old model. Then again, as observed in the calculations relative to the other two enhanced heterogeneity cores and in the previously illustrated analyses, the introduction of a sub-assembly gap worsens the void effect of this reactor.

<table>
<tr><th colspan="2">3D⁺ flower model, gap=0mm</th><th>H2O</th><th>~~N~~</th><th>P</th><th>D</th><th>ZrH</th></tr>
<tr><td><i>16 meshes</i></td><td><i>k-eff</i></td><td><i>[pcm]</i></td><td colspan="4"><i>[$]</i></td></tr>
<tr><td>Nominal</td><td>1.025553±57pcm</td><td>0</td><td colspan="4">0</td></tr>
<tr><td>Total Void</td><td>1.02072±51pcm</td><td>-460</td><td colspan="4">-1.2</td></tr>
<tr><th colspan="2">3D⁺ flower model, gap=1mm</th><th>H2O</th><th>~~N~~</th><th>P</th><th>D</th><th>ZrH</th></tr>
<tr><td><i>16 meshes</i></td><td><i>k-eff</i></td><td><i>[pcm]</i></td><td colspan="4"><i>[$]</i></td></tr>
<tr><td>Nominal</td><td>1.02530±47pcm</td><td>0</td><td colspan="4">0</td></tr>
<tr><td>Total Void</td><td>1.01883±55pcm</td><td>-619</td><td colspan="4">-1.7</td></tr>
<tr><th colspan="2">3D⁺ flower model, gap=2mm</th><th>H2O</th><th>~~N~~</th><th>P</th><th>D</th><th>ZrH</th></tr>
<tr><td><i>16 meshes</i></td><td><i>k-eff</i></td><td><i>[pcm]</i></td><td colspan="4"><i>[$]</i></td></tr>
<tr><td>Nominal</td><td>1.02356±56pcm</td><td>0</td><td colspan="4">0</td></tr>
<tr><td>Total Void</td><td>1.01813±53pcm</td><td>-521</td><td colspan="4">-1.4</td></tr>
</table>

Table 4.21: Advanced heterogeneous model: results for the new advanced model

A second set of calculations was then performed applying the tight blanket concept to the just illustrated “flower” model. The results are shown in Table 4.22 and prove once more the importance of the shielding/capturing effect of the blankets for the behavior under voided conditions of this core. Consequently, introducing a 2 mm sub-assembly gap spacing together with the central blanket advanced heterogeneous model, a void reactivity worth of –5.8$ was calculated with ENDF/B-VI.7, even maintaining the presence of a lower blanket. Another advantage of this configuration would be the higher k-effective level that would allow keeping the originally designed fuel composition and would introduce excess reactivity to compensate for fuel burn-up. A trend that could be observed in the new advanced 3D model was in fact a lower k-effective level for reactor nominal conditions that should be compensated, were this fuel composition to be used in the SCFR, with a higher enrichment or a different core design.

3D$^+$ flower model, gap=1mm		**H2O ~~N~~ P D ZrH**	
16z,Tight Bl.	*k-eff*	*[pcm]*	*[$]*
Nominal	1.02218±56pcm	0	0
Total Void	1.00369±48pcm	-1802	-4.9

3D$^+$ flower model, gap=2mm		**H2O ~~N~~ P D ZrH**	
16z,Tight Bl.	*k-eff*	*[pcm]*	*[$]*
Nominal	1.02350±59pcm	0	0
Total Void	1.00134±54pcm	-2162	-5.8

Table 4.22: Advanced heterogeneous model: advanced model with tight blankets

One drawback relative to this suggested core layout would the difficulty of implementing the model in a standard R/Z geometry simulation tool to perform fluid-dynamics calculations or deterministic based neutronics analyses.

Effect of the introduction of high hydrogen content zirconium hydride

The effect of the introduction of solid moderators in fast reactors to improve the void effect was discussed and analyzed in detail in several publications and will not be treated again here. However, one calculation was performed adopting ZrH_2 instead of $ZrH_{1.7}$. The results are shown in Table 4.23 where the new standard 3D model (without the application of the tight blankets) was used (16 cell axial coolant density profile and ENDF/B-VI.8).

$ZrH_{1.7}$, gap=2mm		**H2O ~~N~~ P D ZrH**	
16 meshes	*k-eff*	*[pcm]*	*[$]*
Nominal	0.97917±49pcm	0	0
Total Void	0.96941±45pcm	-1028	-2.8

ZrH_2, gap=2mm		**H2O ~~N~~ P D ZrH**	
16 meshes	*k-eff*	*[pcm]*	*[$]*
Nominal	0.97976±54pcm	0	0
Total Void	0.96875±55pcm	-1160	-3.1

Table 4.23: Effect of the introduction of ZrH_2

Comparing the two tables it is possible to state that the introduction of ZrH_2 improves the void effect by ~0.3$ increasing the nominal condition k-effective by about 60pcm, while the full void k-effective decreases by ~70pcm. The adoption of a solid moderator with a higher content of hydrogen therefore, improves not only the void coefficient, but also the overall behavior of the SCFR core.

The main drawback of the application of zirconium hydride in a metallic form is the susceptibility to hydrogen migration from the solid matrix, and therefore, the weakening of moderating potential in case of severe transients that might affect the solid moderator matrix and consequently induce the release of a even higher amount of reactivity (see [Majert (1994) /90/]).

Effect of the introduction of cooled blankets

One last comment regards again another characteristic of the radial blankets. The blankets proved to play a fundamental role for the safety coefficients of this reactor and their shielding effect was therefore widely discussed. Another important feature of the blanket assemblies that were used for this study, was their compactness and their solid arrangement, meaning that no coolant between the can walls and the uranium hexagonal pin was present, since it was substituted with more depleted uranium, hence creating a solid uranium matrix cooled only by internal clad channels (see Figure 4.29: Original blanket configuration and Figure 4.30: Cooled blanket configuration).

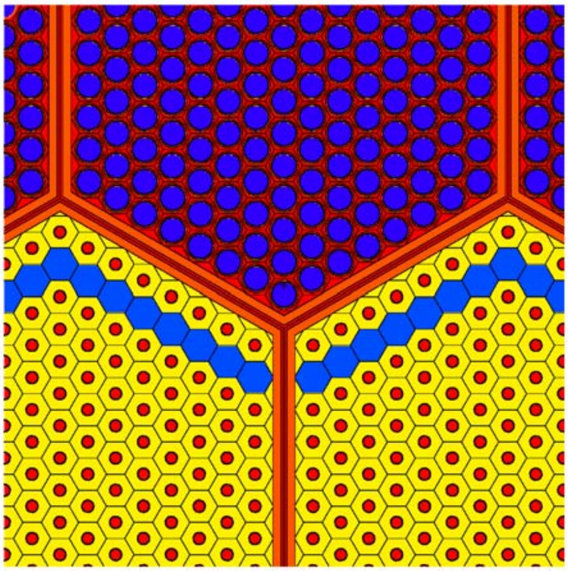

Figure 4.29: Original blanket configuration

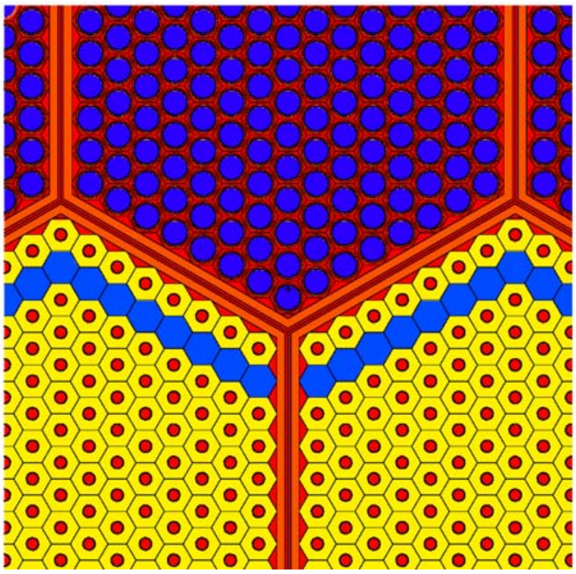

Figure 4.30: Cooled blanket configuration

The classical pin layout would account for a coolant gap between the hexagonal pins and the can walls as represented in Figure 4.30 (in both figures the coolant is represented in red). Some calculations were performed for this geometry as well, although it is not considered feasible. Assuming the original core design, where the blanket hexagonal pins do not present any external cladding, a structure that would allow for the coolant to be directly in touch with the depleted uranium cannot be seen as a feasible option, especially from a safety point of view. At any rate, a few calculations were performed for this geometry and the results are reported in Table 4.24 and Table 4.25.

As it could be expected, the introduction of this additional coolant deteriorates the reactor void coefficient consistently of about 1.6$ and reduces the nominal condition k-effective by at least 100 pcm increasing the full void k-effective by about 340 pcm, therefore worsening the overall core performance.

ORIGINAL DESIGN[24]

ENDF/B-VI.8, gap=0mm			**H2O ☒N P D ZrH**
20 meshes	*k-eff*	*[pcm]*	*[$]*
Nominal	0.98469±60pcm	0	0
Total Void	0.97077±45pcm	-1456	-3.9
ENDF/B-VI.8, gap=1mm			**H2O ☒N P D ZrH**
20 meshes	*k-eff*	*[pcm]*	*[$]*
Nominal	0.98139±55pcm	0	0
Total Void	0.96879±44pcm	-1325	-3.6
ENDF/B-VI.8, gap=2mm			**H2O ☒N P D ZrH**
20 meshes	*k-eff*	*[pcm]*	*[$]*
Nominal	0.98178±51pcm	0	0
Total Void	0.96851±50pcm	-1396	-3.8

Table 4.24: Reference calculations

COOLED BLANKETS DESIGN

ENDF/B-VI.8, gap=0mm			**H2O ☒N P D ZrH**
20 meshes	*k-eff*	*[pcm]*	*[$]*
Nominal	0.98250±62pcm	0	0
Total Void	0.97470±45pcm	-814	-2.2
ENDF/B-VI.8, gap=1mm			**H2O ☒N P D ZrH**
20 meshes	*k-eff*	*[pcm]*	*[$]*
Nominal	0.98038±61pcm	0	0
Total Void	0.97319±48pcm	-754	-2.0
ENDF/B-VI.8, gap=2mm			**H2O ☒N P D ZrH**
20 meshes	*k-eff*	*[pcm]*	*[$]*
Nominal	0.98250±60pcm	0	0
Total Void	0.97187±45pcm	-790	-2.1

Table 4.25: Effect of the cooled blankets

Influence of core height on the void worth and remarks on the tight lattice configuration

Following the same line of approach adopted until now, that is to maintain the current basic design and introduce only minor changes that would not affect the overall layout of the vessel and its internals, another set of calculations was performed with the aim of improving the void worth and understanding better how the reactor would behave should a few changes be introduced.

It has been shown how the introduction of the tight blanket solution would improve significantly the void reactivity coefficient for the SCFR. On the other hand, a 0 mm gap spacing, although applied only to a few subassemblies, is not seen as a viable engineering solution. Therefore, a new core configuration was implemented using a 0.8mm gap spacing.

This new configuration, is based on a 2 mm subassembly gap spacing for the seed areas and 0.8 mm for the blankets, compensating the difference in the lattice dimension adopting the solution described before (using a thicker can wall).

This solution is considered to be more realistic from the design and construction point of view, although a detailed mechanical analysis would still be necessary to assess its

---

[24] These calculations were performed with an average fuel temperature of 1600K instead of 1200K; hence the smaller void effect (see Table 4.1 and Table 4.10).

actual feasibility. Based on the same geometry, another calculation was performed reducing the core height. It is a commonly adopted solution to improve void worth that moves in the direction of the so-called “pancake” cores. In order to preserve the general configuration the examined core is only 0.6 m shorter that the original design (3.36 m excluding axial blankets). This was achieved shortening of 15 cm each one of the 4 axial seed areas, therefore maintaining the original axial and radial enrichment distribution. The results relative to these two cases are shown in Table 4.26.

As to be expected the introduction of gap spacing in the blankets worsens the performance of the tight blanket configuration and the void worth absolute value decreases by 1.3$ (from –4.8 to –3.5$). The introduction of a shorter core on the other hand, improved the void reactivity coefficient by 0.8$, eventually compensating for the margin lost using a spaced subassembly configuration. However, the adoption of a shorter core will probably affect the thermal efficiency of the reactor, not to mention the lower initial k-effective that should probably balanced by a higher initial enrichment. In conclusion, should this solution be adopted, further investigations will be needed taking into account balance of plant design, core fluid dynamics and neutronics.

Blanket spacing = 0.0mm		H2O	☒N	P	D	ZrH	
H=3.36m	*k-eff*	*[pcm]*			*[$]*		
Nominal	0.98178±51pcm	0			0		
Total Void	0.96851±50pcm	-1396			-3.8		
Blanket spacing = 0.8mm		H2O	☒N	P	D	ZrH	
H= 3.36m	*k-eff*	*[pcm]*			*[$]*		
Nominal	0.98029±62pcm	0			0		
Total Void	0.96804±52pcm	-1291			-3.5		
Blanket spacing = 0.8mm		H2O	☒N	P	D	ZrH	
H= 2.76m	*k-eff*	*[pcm]*			*[$]*		
Nominal	0.97780±52pcm	0			0		
Total Void	0.96282±54pcm	-1591			-4.3		

Table 4.26: Effect of the tightly spaced blankets and of the shorter core (gap = 2mm)

4.4 Coupled calculations for the SCFR

The results and the remarks that were discussed in the last chapters outline many of the SCFR specific characteristics. Whether they are inherent to its neutron physics behavior, or to its mechanical design, they require detailed and dedicated tools of analysis to be studied. Hence, MCNP was chosen for the assessment of the void reactivity worth for this reactor, because of its flexibility and the design independent cross section treatment.

On the other hand, the sensitivity studies showed that, due to the strong susceptibility of this design to the initial/boundary conditions of the calculations, the application of MCNP alone would not be enough to achieve an accurate description of the behavior of the reactor. As a matter of fact, it was shown how the fuel temperature distribution, which is strictly related to the power profile, and of the coolant density distribution, can significantly affect the results.

Therefore, in order to take these effects into account, a full three-dimensional core model was developed and implemented in MCNP and successively coupled with a fluid-dynamics code: MXN (see Chapter 3.2).

Before describing the coupled system and its results, it is worth giving a review of the development stages of the MCNP SCFR core model. At first a typical two-dimensional geometry was used (infinite height core), unfortunately this approximation proved extremely rough, neglecting the strong axial neutron streaming, which characterizes this reactor. A three-dimensional model was hence implemented, and refined with time, as long as new details of the design proved to be important for the correct description of the peculiarities of the reactor (see Chapter 4.2 and 4.3).

The last improvement of the model focused on the introduction of the capability of using axial temperature profiles in the seed/driver regions of the core, that is in the areas where most of the power is generated and therefore, where the fuel might show high temperature gradients. The introduction of this additional detail is of extreme importance for a correct description of the system, moreover, given the discussed strong mutual dependence of the void reactivity coefficient and the Doppler coefficient.

In order to choose the number of axial cells to be introduced in the model and to assess whether the chosen discretization detail would be sufficiently accurate, a typical sensitivity analysis was conducted. A lot of literature suggests that a good number of axial core meshes for BWR stability analyses is 15 (see for instance /91/, /92/, and /93/), and given the strong coolant density profile some of the neutronics characteristics of the SCFR resemble a BWR. Furthermore the SIMMER-III model that was used for the first core melt analyses of the system was based on a 20 mesh axial nodalization, therefore for the sensitivity analysis the active fuel pins were subdivided in 2, 4, 10, and 20 axial cells.

K-effective in both nominal and voided conditions was calculated as a function of mesh number, together with the estimation of the void effect, a cosinusoidal axial temperature profile was assumed with a constant average value of 1500K. The results of this study are shown in Figure 4.31, where it can be noticed that the results relative to 10 and 20 cells are very close (the difference equals to 31pcm, less than the average standard deviation ~40 pcm), therefore proving the adequateness of the 20-cell model to describe the problem.

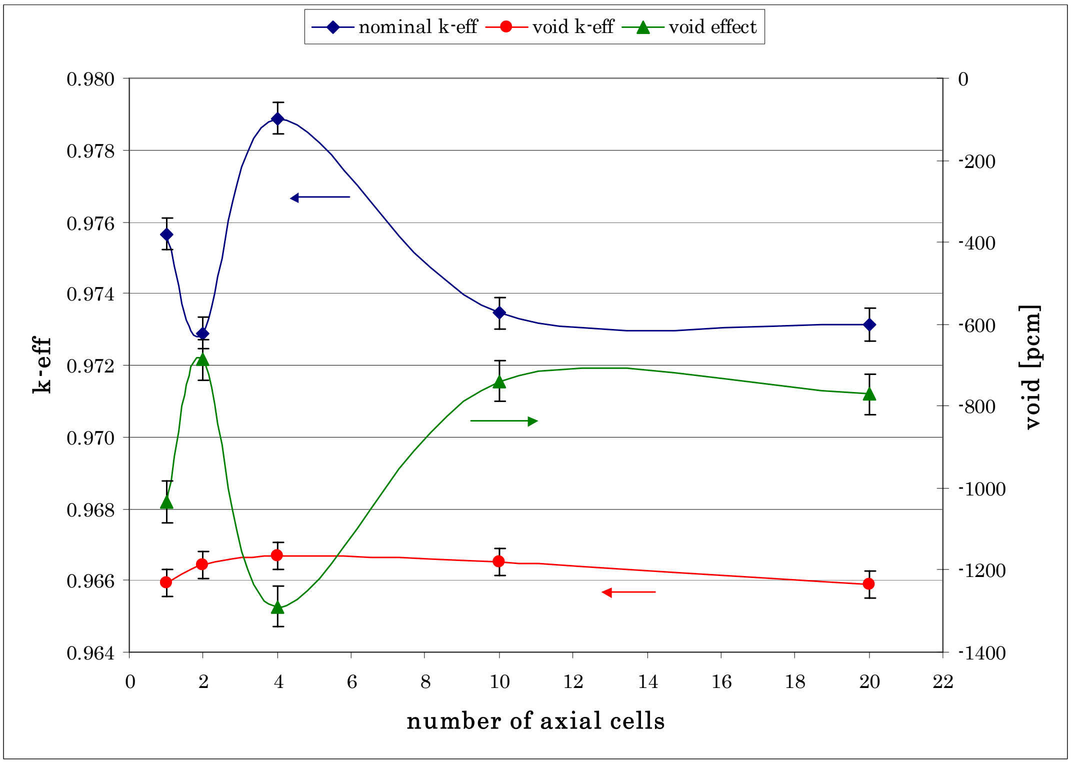

Figure 4.31: Fuel temperature profiles sensitivity analysis

Another interesting conclusion that can be drawn from Figure 4.31 is that the voided condition k-effective does not show a significant dependence on the number of axial cells. The faster neutron flux (~10^3 ÷10^6 eV), which differentiates the voided from the nominal condition core, implies that the effect of the thermal fission cross section is less important in the overall economy of the reactor, and therefore the Doppler broadening, or narrowing, of both the fission and the absorption cross section resonances does not play a strong role.

The 20-mesh model was then chosen as the standard model for the coupled neutronics/fluid-dynamics calculations.

The flow diagram of the coupling of the two codes is described in Figure 3.5., while the channels in which the core was subdivided are shown in Figure 3.6 (see Chapter 3.2 for the details of the models approximations).

Analysis of the iterations

With the aim of obtaining first guess values, a first calculation was performed using SIMMER-III. The profiles of the coolant density, of the fuel average temperature (which are used for the MCNP input), and of the power (which is used for the MXN input) that were obtained, are shown in the following Figure 4.32 and Figure 4.33[25].

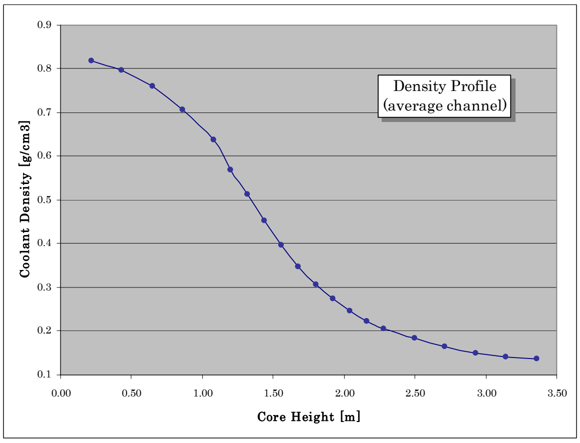

Figure 4.32: S-III coolant density profile

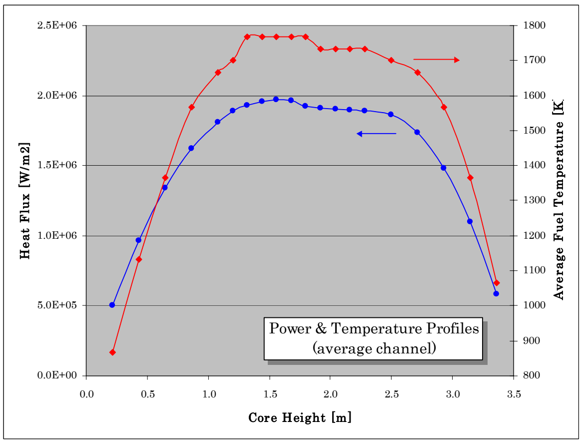

Figure 4.33: S-III power, temperature profiles

The fuel temperature profile follows rather closely the power profile, since the local fuel temperature is proportional to the locally released fission power.

The following iterations were then performed using MCNP and MXN, as described in the flowchart (see Figure 3.5). The results, relative to the first four steps, are shown in Figure 4.34. After the first iteration the profile changes rather significantly showing a peak in the lower part of the core, where the coolant density is higher: before the pseudo-liquid, pseudo-vapor transition point. The temperature/density feedbacks from iteration to iteration drive the solution towards the searched steady-state profiles.

A very important remark regarding the iteration procedure regards the fact that MXN does not calculate coolant velocity but rather requires it as an input; a simple calculation routine was developed to adjust the channel coolant velocity proportionally to the power produced in the channel itself and respecting the design constraints.

---

[25] In these and in the following figures two-dimensional curves relative to channel averaged values will be shown. It should be kept in mind that the MXN calculations were performed in R/Z geometrical approximation, and that the MCNP tally were therefore designed to provide R/Z power data.

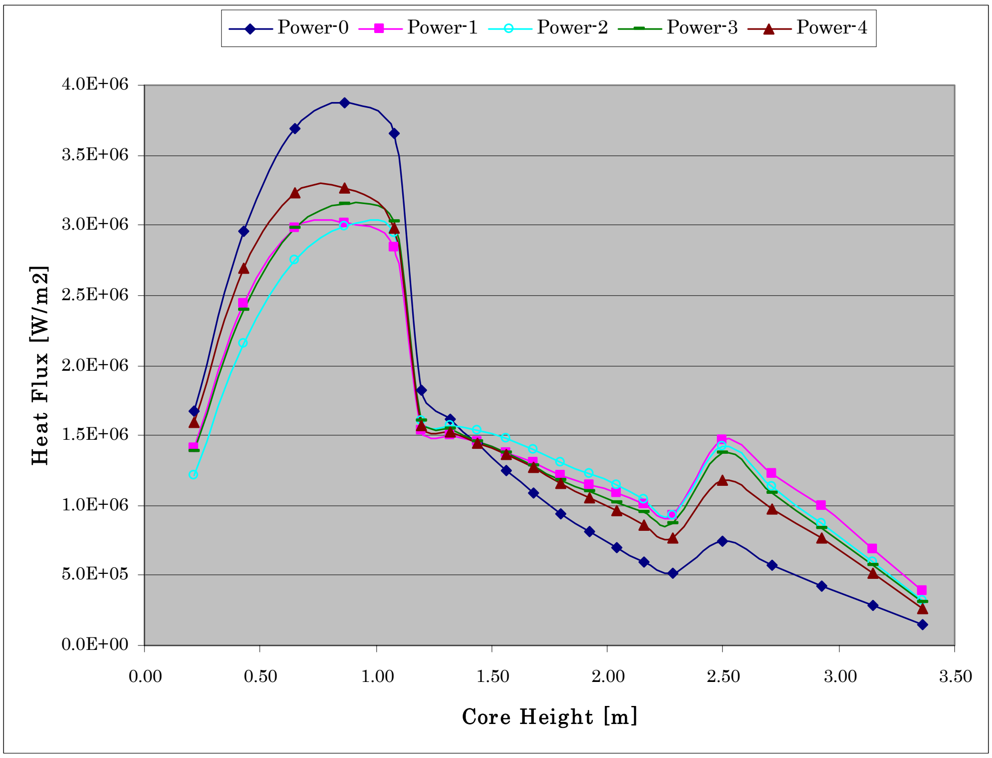

Figure 4.34: Power profiles (1st four iterations)

The importance of this procedure can be recognized in Figure 4.35, where the coolant density profile is plotted together with the power profile to appreciate in detail how the power peak is located precisely in the pseudo-liquid phase.

The profile of "4a" is relative to the recalculated velocity profiles and the fitted outlet temperature, and it is worth noting that this procedure shifts the curve from the curves described by "4" to a position between "2" and "3" approaching the converged steady state profile.

The steady state profiles are shown in Figure 4.36. It is important to point out that the profiles are not strictly coincident. This can be explained taking into account the approximations that are inherent to the methods and the models e.g. the comparatively large mesh size around the transition point.

The average MCNP statistical error relative to the power calculation is of about 1.5%, to which the error due to the average 25K approximation on the temperature of fuel should be added. However, the results shown in Figure 4.36 can be considered to be the steady state solution that was looked for.

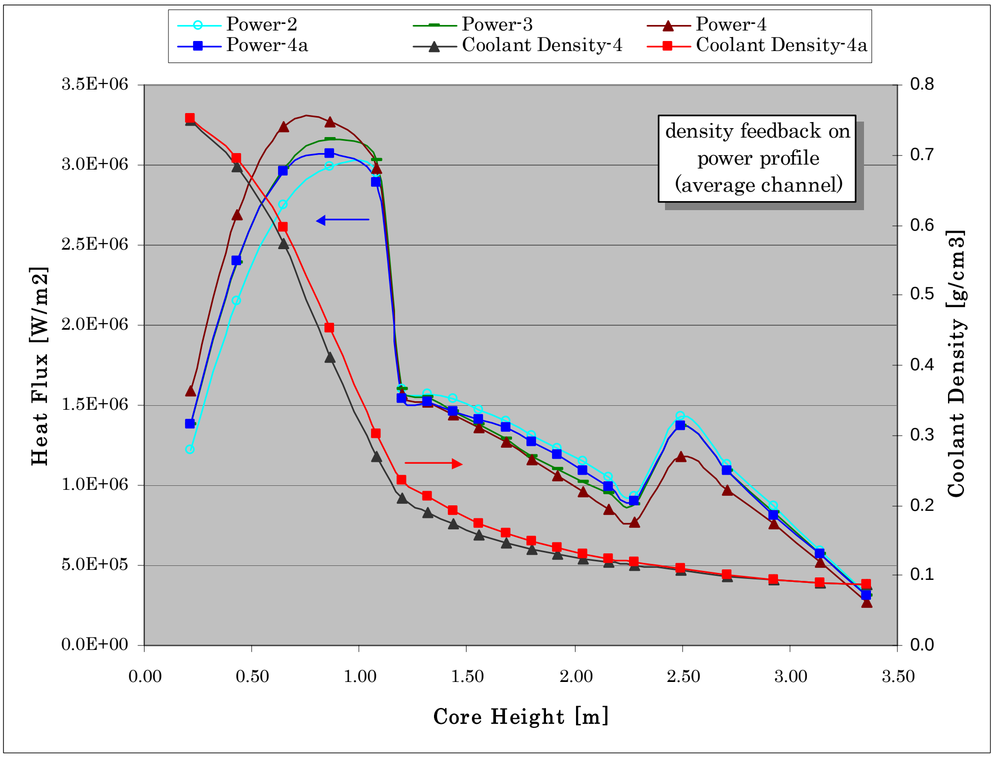

Figure 4.35: Coolant density feedback

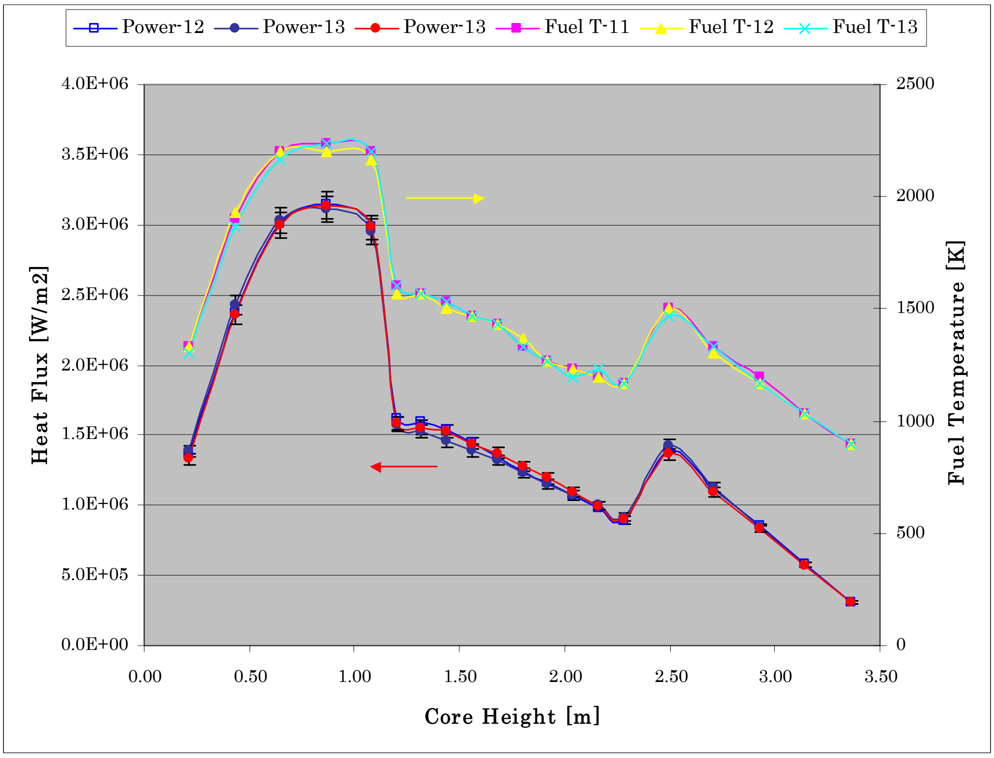

Figure 4.36: Steady state power and fuel temperature profiles

In order to verify that there is only one solution to this problem, a second series of calculations was performed changing the initial conditions. This second set of iterations converged to the same solution of the first one (well within the statistical uncertainty) as shown in Table 4.27.

Set	k-effective	Uncertainty [pcm]	Difference [pcm]
1	0.96557	39	0
2	0.96562	35	+5

Table 4.27: k-effective of the converged solutions

Other interesting and important aspects that were observed during the iterations procedure were the sensitivity of the SCFR to the fuel temperature profile and to the coolant density profile. One test iteration was in fact executed without updating the fuel temperature; this resulted in an overshooting of the power profile peak caused by the mild shift of the density profile not followed by the corresponding fuel temperature adjustment. A second test iteration instead was executed without updating the coolant density profile. Once again it was appreciated how, being the lower part of the core the region with the highest importance, neglecting any of the local feedbacks, although apparently very small, drives big changes in the local reactivity, which has an immediate effect on the power distribution profile. Hence, another important aspect of this reactor is the compensating effect that fuel temperature and coolant density feedbacks have on reactivity.

These simple calculations outline the extreme sensitivity of this design to the coolant density profile that is the parameter that mostly affects the reactivity of the system and its power distribution.

Void effect calculations

Having finally reached a steady state, and consequently having calculated in detail fuel temperature distributions and coolant density profiles, the void effect can be now estimated with higher accuracy.

Two cases were examined: the first one using the original design (see for instance Figure 4.29), the second one using the improved void design (see Figure 4.20). The physical parameters distribution that was calculated specifically for the improved void design was successively used for an evaluation of the void effect for the original design. This procedure is not strictly accurate, since a new iteration should be performed in order to reach the steady state relative to the original design. However, given the minor differences between the two layouts and given the fact that these differences regard exclusively the configuration of the blankets, which are the less important regions of this core, the effect of this approximation is considered to be negligible. Furthermore, it gives a coherent basis of comparison to the previously shown results. The outcome of these new calculations is shown in Table 4.28.

Original design		H2O ~~N~~ P D ZrH	
coupled	*k-eff*	Δρ *[pcm]*	Δρ *[$]*
Nominal	0.96562±35pcm	0	0
Total Void	0.96573±35pcm	+12	+0

Improved void design		H2O ~~N~~ P D ZrH	
coupled	*k-eff*	Δρ *[pcm]*	Δρ *[$]*
Nominal	0.96818±38pcm	0	0
Total Void	0.96682±33pcm	-145	-0.4

Table 4.28: MCNP/MXN void effect calculations

As discussed earlier, the use of a tight blanket configuration improved the void effect, on the other hand, the coupled calculation shows a great discrepancy with the previously coupled MCNP/SIMMER-III estimation [Mori (2003) /54/], giving an estimation of the void effect, which is worryingly close to zero. However, this result cannot be considered too surprising, the MCNP/SIMMER-III sensitivity analysis showed that a small change of the temperature of the fuel in the lower part of the core affected dramatically the void worth of this core and the local temperatures predicted by MXN in the lower part of the core are very high and this has an immediate effect on the void coefficient as shown in Table 4.1 and Table 4.10.

These results prove that, even if the tools of analysis are extremely accurate, the approximations that are made “a priori”, sometimes considerably affect the final results. The SIMMER-III calculations cannot be considered wrong, but only merely approximate, since a sound steady state was not reached, a uniform power distribution was assumed, and furthermore the TWODANT neutronics calculation was based on a rather rough definition of the parameters, not to mention the inevitable approximations in the cross sections. Furthermore, the coolant density distribution that was assumed for the TWODANT power distribution calculation presents relevant discrepancies with the one used for the MCNP void effect calculations.

Effect of fuel composition on void effect

The predicted void effect for the SCFR, assuming that the core is completely loaded with fresh fuel, is then ~–0.4$. Taking into account the uncertainties that are inherent with the cross section treatment and with the implemented models, although the latter were decisively reduced by the introduction of the coupled calculations, this value cannot guarantee a safe operation of the reactor through its complete fuel cycle. For this very reason, another set of calculations was performed changing the fuel enrichment with the aim of reducing the height of the peak at the bottom of the core, and thereto the average fuel temperature, hopefully achieving a better void coefficient.

The original design, and the new fuel enrichment distribution are shown in Figure 4.37 and Figure 4.38, respectively. The new tested distribution is equal to the original one save for the lower seed, where it was decreased by one per cent. The fuel elements were then originally divided in four axial enrichment zones, each of which had the same average fuel temperature.

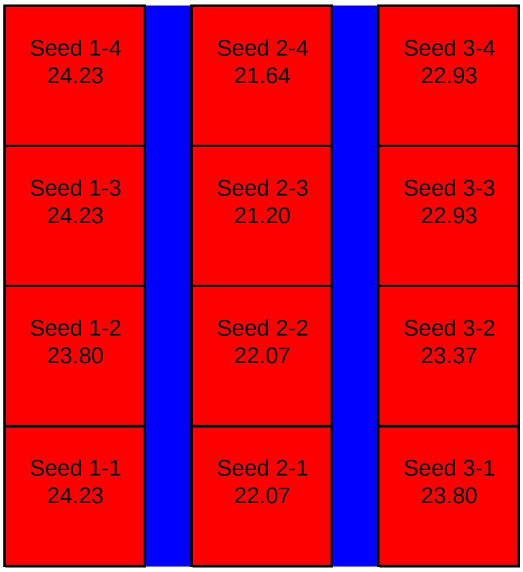

Seed 1-4 24.23	Seed 2-4 21.64	Seed 3-4 22.93
Seed 1-3 24.23	Seed 2-3 21.20	Seed 3-3 22.93
Seed 1-2 23.80	Seed 2-2 22.07	Seed 3-2 23.37
Seed 1-1 24.23	Seed 2-1 22.07	Seed 3-1 23.80

Figure 4.37: Original plutonium enrichment distribution

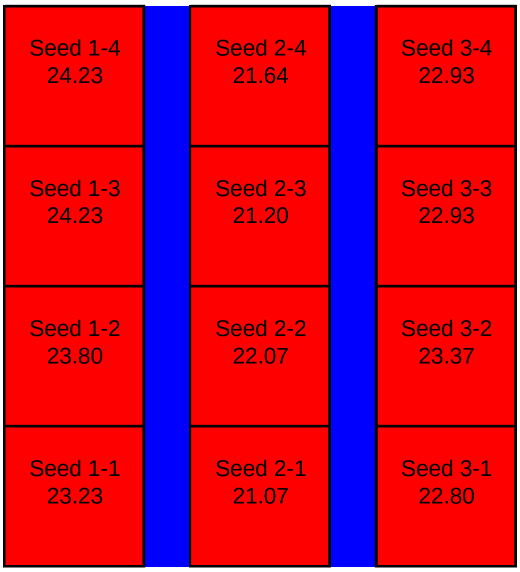

Seed 1-4 24.23	Seed 2-4 21.64	Seed 3-4 22.93
Seed 1-3 24.23	Seed 2-3 21.20	Seed 3-3 22.93
Seed 1-2 23.80	Seed 2-2 22.07	Seed 3-2 23.37
Seed 1-1 23.23	Seed 2-1 21.07	Seed 3-1 22.80

Figure 4.38: New tested plutonium enrichment distribution

It was considered reasonable and convenient to maintain this arrangement and run again MXN/MCNP until a new steady state was reached. Figure 4.39 shows the final results relative to this new case and also illustrates the shift of the power profile due to the voiding of the core. It is interesting to note how the lack of moderation in the lower part of the core, due to the voided conditions, only mildly depresses the lower power peak, at the same time the faster spectrum enhances the peak at the top of the core, which can be explained by the relatively higher enrichment in the second seed, which is a region of high neutron importance and where the radial peak occurs (see Figure 4.40).

As to be expected, both the power and therefore the temperature profiles are lower at the bottom of the core now, and, having kept the total power constant, the peak in the upper part of the pin is now more accentuated.

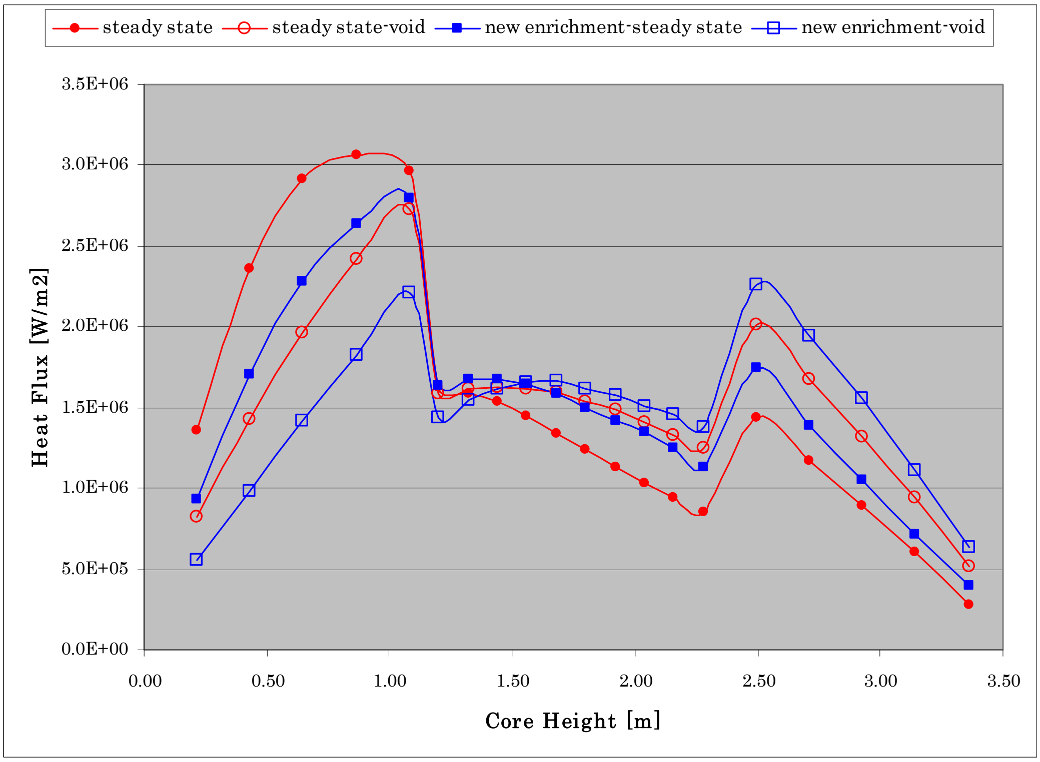

Figure 4.39: Power profile nominal and voided conditions (original vs. new enrichment)

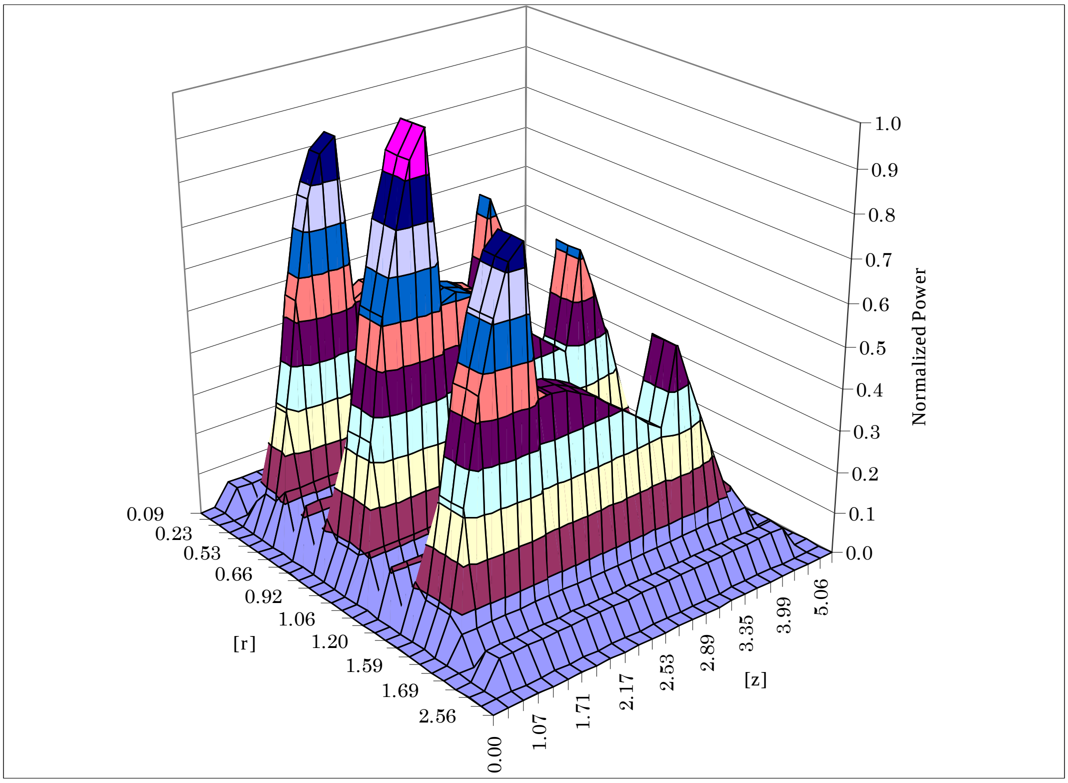

Figure 4.40: MXN/MCNP 3D power profile

From an operational point of view this highly peaked power distribution causes several concerns: both from the safety perspective, because of possible instabilities driven by the top peak [D'Auria (1996) /94/], and from the economics perspective, because of the uneven fuel consumption during irradiation. However, the analysis of these phenomena goes beyond the scope of this work, although it definitely represents an interesting and important challenge. Nonetheless, a proper tuning of the enrichment distribution and the introduction of burnable poisons can be a viable, although expensive, solution to this problem, were it proven necessary.

<table>
<tr><th>New enrichment distribution</th><th>H2O</th><th>~~N~~</th><th>P</th><th>D</th><th>ZrH</th></tr>
<tr><td><i>coupled</i></td><td colspan="3"><i>k-eff</i></td><td>Δρ <i>[pcm]</i></td><td>Δρ <i>[$]</i></td></tr>
<tr><td>Nominal</td><td colspan="3">0.96350±37pcm</td><td>0</td><td>0</td></tr>
<tr><td>Total Void</td><td colspan="3">0.96136±35pcm</td><td>-231</td><td>-0.6</td></tr>
</table>

Table 4.29: Void effect calculations: improved void design (new fuel enrichment)

As a matter of fact, the void effect calculations performed starting from the new "low" enrichment fuel steady state seem rather promising. Table 4.29 reports the results relative to this last case. The void effect improves by 0.2$ becoming more negative and proving the efficacy of the new fuel composition. On the other hand, the nominal condition k-effective is even lower than it was before therefore requiring a more comprehensive reassessment of the plutonium enrichment magnitude and distribution.

Effect of the improved void configurations

In Chapter 4.3 new core configurations and a different moderator density were recommended to significantly improve the void effect. The effect of the introduction of ZrH_2, instead of $ZrH_{1.7}$, for the coupled calculation steady state conditions relative to the new fuel enrichment distribution, is shown in Table 4.30.

<table>
<tr><th>New enrichment distribution</th><th>H2O</th><th>~~N~~</th><th>P</th><th>D</th><th>ZrH_2</th></tr>
<tr><td><i>coupled</i></td><td colspan="3"><i>k-eff</i></td><td>Δρ</td><td>Δρ <i>[$]</i></td></tr>
<tr><td>Nominal</td><td colspan="3">0.96252±41pcm</td><td>0</td><td>0</td></tr>
<tr><td>Total Void</td><td colspan="3">0.96001±36pcm</td><td>-272</td><td>-0.7</td></tr>
</table>

Table 4.30: MCNP/MXN void effect calculations (ZrH_2)

The improvement of the void worth is not large, but definitely appreciable, especially given the low absolute value of the void effect for the estimated steady state nominal conditions of the reactor.

The effect of the application of the "flower model" to the new conditions cannot be assessed easily. The core layout reported in Figure 4.28 in fact does not present the radial symmetry, which would be needed to apply MXN to the new core design. A three-dimensional geometry capability would be necessary to simulate correctly this particular configuration.

However, assuming that the coolant density and fuel temperature axial profiles in the seed areas would not change significantly along the radial and the angular direction a calculation introducing their average values in every seed subassembly was performed. The results are shown in Table 4.31.

New enrichment + AHM[26]		**H2O**	~~**N**~~ **P** **D** **ZrH_2**
coupled	*k-eff*	Δρ	Δρ *[$]*
Nominal	1.01509±36pcm	0	0
Total Void	1.01218±37pcm	-284	-0.8

Table 4.31: MCNP/MXN void effect calculations (flower model)

Once more, the void reactivity worth improves, although only by 0.1$, but what is relevant to underline here is the effect on the absolute value of k-effective. Indeed, the k-effective for the AHM configuration, in comparison to the one reported in Table 4.30 for equivalent conditions, is larger by more than 5000 pcm, and therefore, for a comparable fuel composition, it would imply an easier fuel enrichment distribution rearrangement keeping the plutonium inventory at a reasonable level and comparable to current LMFR designs (~10 tons).

---

[26] Advanced Heterogeneous Model (flower model).

CONCLUSIONS

The supercritical water fast reactor is an interesting alternative and innovative reactor system, which has been under discussion and investigation for several years, with a great contribution from the Nuclear Engineering Research Laboratory of the University of Tokyo.

The SCFR, which is also part of the selected reactor concepts within the framework of the Generation IV roadmap, is of interest especially because of design simplification and thermal efficiency improvement.

In 2001 FZK has undertaken contract work for preliminary studies of severe accident phenomena in the SCFR. The scope of the contract was to provide a first general assessment of the behavior of the SCFR under core disruptive accident conditions and specifically the following issues had to be investigated:

1) Identification and analysis of major initiators that lead to severe core damage,
2) Evaluation of core damage scenarios and their effects, and
3) Study of measures for mitigating core damage effect.

These first studies showed the high susceptibility of transient evolution patterns to the boundary conditions and pointed out peculiar behaviors in the core dynamics. Hence, it was decided to start a comprehensive assessment of the neutronics safety performance of the SCFR with the aim to improve and optimize its safety parameters.

The SCFR is a reactor demonstrating both ‘thermal’ light water and ‘fast’ reactor features. During normal operation and up to actual core damage the reactor behaves similarly to a classic light water reactor, showing comparable dominating scenarios, as for instance Loss Of Coolant Accidents. Then, once a core damage scenario is initiated, the reactor starts to behave more like an ordinary fast reactor. One of the differences is that in sodium-cooled reactors the reactor core (even in voided state) is always surrounded by sodium and therefore in the low-pressure system of sodium-cooled reactors, LOCAs are not a major concern. Moreover, any fuel, discharged from the core upwards or downwards, will get in contact with the coolant and hence will be quenched (heat removal in post accident conditions can be successfully demonstrated for these designs). Quite the opposite happens in a SCFR.

Loss Of Coolant Accidents are a Design Basis Accident for SuperCritical Water cooled Reactors, since the system is cooled by water at very high pressure (25 MPa). This implies that in case of a Large-Break-LOCA all the coolant inventory is lost very rapidly and therefore, core melt can occur undisturbed if the Emergency Core Cooling System is not activated. Furthermore, a loss of coolant drives a reactivity feedback, which becomes then a major safety concern for this design, even more so if the transmutation capabilities are to be exploited and therefore the core is loaded with MOX or transmuter fuel.

The optimization of the void reactivity effect was therefore the main goal of this thesis.

Several analyses were thus conducted, which showed that due to the heterogeneous core design (internal blankets and zirconium hydride “rings” around the seeds) a strong positive void effect could be avoided. On the other hand, because of its heterogeneity, the neither thermal nor fast spectrum, and the strong gradients of the physical parameters, significant uncertainties must be accounted for in the evaluation of the void worth. In order to improve the accuracy of the calculations and eventually overcome the uncertainty range, more and more detailed models were developed and more and more refined tools were implemented.

The first analyses were conducted with a simple diffusion code, RHEIN, and crosschecked with the S_n code TWODANT, which was used within the SIMMER-III code system. These analyses predicted a slightly negative void coefficient and an overall uncertainty that was roughly estimated to be around 10$. Successively, in order to improve the accuracy, 2D and 3D Monte-Carlo models were developed and implemented in MCNP4C, making use of the great flexibility of Monte-Carlo geometry and cross section set-up. These new calculations confirmed the previous results, but reduced the estimated uncertainty to about 5$.

It was not until coolant density profiles, improved void blankets, and advanced heterogeneous models were introduced in the Monte-Carlo calculations that a definitely negative void could be predicted. A summary of the effect on the void worth of the different design improvements that were introduced is shown in Figure 5.1.

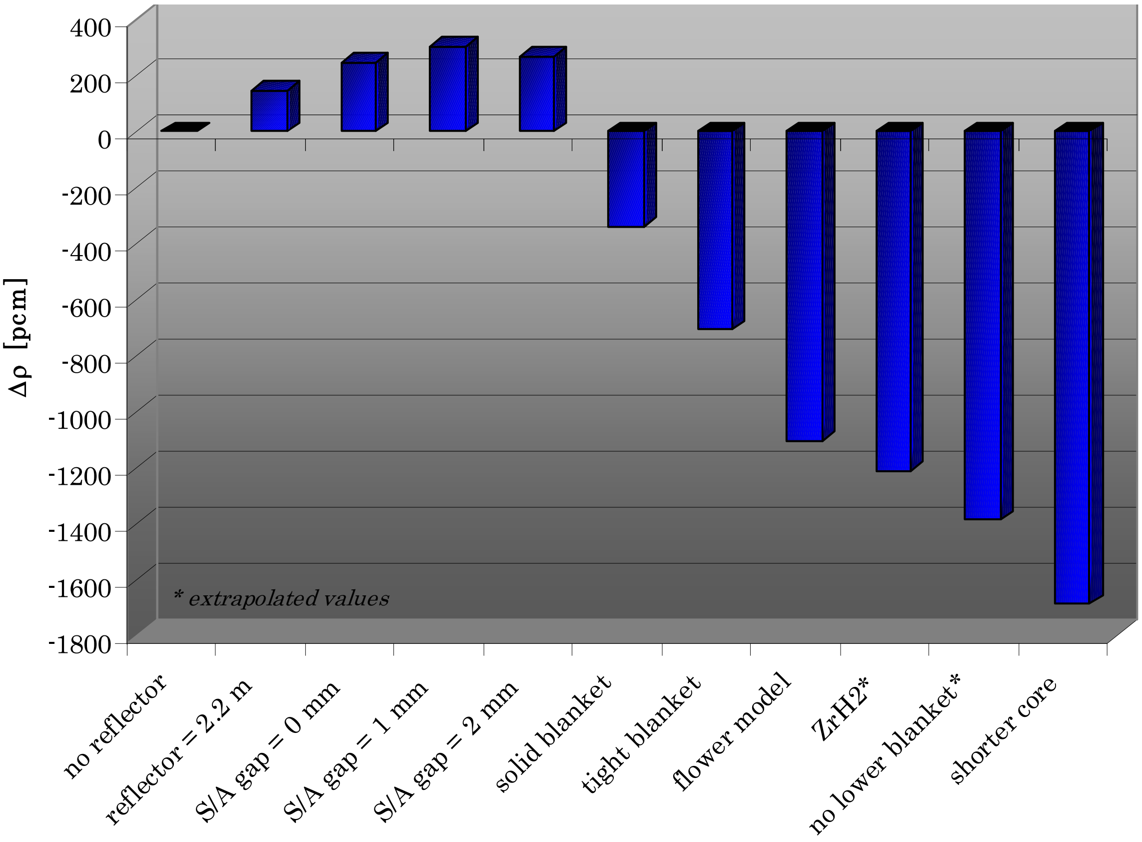

Figure 5.1: Dependence of the void worth on different design configurations[27]

---

[27] All cases are relative to a 20 mesh axial coolant density profile, a single average fuel temperature of 1200K, and ENDF/B-VI.8 as the reference cross section data set.

The introduction of the radial reflector and of the subassembly gaps did not affect considerably the void effect ($\Delta\rho < 1\$$), and are to be considered as refinements of the model, rather than design solutions. The application of the solid blanket is a fuel fabrication and safety requirement (see "Effect of the introduction of cooled blankets", p. 113). The most significant design alterations therefore, were the introduction of the tight blankets and of the "flower" core configurations, which together account for an improvement of the void worth of about –3$. The great advantage of these suggested design modifications is that they do not require a new mechanical outline of the vessel and/or of its internals, therefore simplifying their eventual application. The same argument applies to the introduction of a solid moderator with a higher hydrogen/metal ratio like ZrH_2 instead of $ZrH_{1.7}$, which would improve the void worth by about –0.5$.

The last two modifications, although very promising, would require an extensive redesigning effort, requiring at least a new pin configuration to account for the removal of the lower blanket, and a completely new reassessment of the core/reactor design, from both the nuclear and the thermal-hydraulics point of view, were a shorter core introduced.

The application of these features required an appreciable sophistication of the calculation models used to assess their performance and, the more accurate the detail of the model, the more important became the correct evaluation of the physical parameters describing the different reactor conditions. Moreover, the estimation of the Doppler reactivity worth showed a very strong dependence of this parameter on the density of the coolant, which denoted the importance of a precise evaluation of the fuel temperature and of the fuel temperature radial and especially axial profiles. The last stage of the work therefore, concerned the development of a fast running fluid-dynamics code (MXN) that could be coupled with MCNP to increase the accuracy of the results.

The coupled calculations that were performed using the MCNP/MXN routine showed that the void coefficient becomes negative (about –0.8$) only using the design improvements that were proposed. This result, which seems to contradict the previous considerations, can be explained by the strong neutronics decoupling of the lower and the upper regions of the SCFR, as outlined by the studies on the control rods. In fact, although the average core temperature (1500K) is not too different from the one used for the single fuel temperature calculations (1200K and 1600K), its profile affects the final results significantly (the void effect is in absolute values about 3$ smaller), because of the very high fuel temperatures in the region of highest neutronics importance: the core bottom.

In spite of this, the adoption of a better-devised core enrichment distribution, in addition to the new core design features that were specifically developed for this purpose, shows that there is the potential to reach a sufficient margin to guarantee a safe operation of the SCFR.

Recommendations for additional studies

Additional investigations and eventually experimental work would be needed to improve the reliability of the results of the performed simulations. To reduce the uncertainties a set of relevant experimental results should in fact be selected and benchmarked for the considered computer codes and nuclear data libraries simulating the complicated material arrangement, including the evaluation of the thermal scattering matrices for supercritical water.

At low energies in fact, the hydrogen of water (the main moderator in LWR) cannot be treated as a free atom while modeling a collision with a neutron, but one must take into account the excitation of the dynamical modes of H_2O molecules. The accuracy of employed neutron scattering law data (or $S(\alpha,\beta)$ data) for water in the thermal and epithermal energy region, affects significantly the accuracy of criticality calculations for conventional LWRs.

The scattering law data used for LWR analyses are obtained by fitting parameters of certain nuclear models (for the motions of the hydrogen and oxygen atoms in the water molecule) to experimental data. Although the models can be fairly simple (at the moment, a completely accurate quantum mechanics theoretical treatment does not exist, this being similar to many other problems of neutron physics), their accuracy may be sufficient for cases similar to those for which the experimental data are available (and taken into account while fitting the model parameters).

In the SCFR and other types of supercritical water-cooled reactors, the water state (temperature, power) is quite different compared to the conventional thermal LWR reactors. If experimental data (for the influence of this chemical binding) are missing for a certain case or range (e.g. high pressure and temperature of water), a thorough re-evaluation, validation, and selection of the available models should be done to provide best estimate $S(\alpha,\beta)$ scattering parameters (which can be applied in the neutronics calculations) for these cases. Therefore, the validity of data available in nuclear data libraries (for which the models and their parameters were developed having in mind LWR application) should be reassessed. Probably, more refined experiments and/or theoretical evaluations are needed to make sure that the water cross-section data are acceptable for adequately modeling neutron scattering in supercritical water-cooled reactors.

Due to a relatively fast neutron spectrum, this problem seems of less importance for the SCFR, but more relevant for thermal supercritical water-cooled reactor options. However, using more accurate neutron scattering models for water may also have an influence on the coolant density and void effect computation results for the SCFR.

Finally, another additional set of studies should focus on the correlations between the safety parameters and the fuel cycle strategies (see Appendix B). In this context, possible deviations to the employed plutonium vector and margins for the content of minor actinides might be determined and their influence on the reactor parameters evaluated. Other investigations that are connected to the void reactivity effect are the burn-up effects on this parameter. Preliminary evaluations, based on deterministic models, indicate a lower absolute value of the void effect at EOC conditions, as one may expect for a fast reactor core initially loaded with LWR MOX fuel. However, this result should be confirmed by more refined tools e.g. Monte-Burns /95/, or MCB /96/. Moreover, one should also check that the effect decreases monotonously with burn-up, i.e. that no local maximum may occur, and finally further studies could focus on the effect of the introduction of different classes of solid moderators that could have higher hydrogen densities and/or better thermal stability (e.g.: $PrH_{2.8}$, $LaH_{2.76}$, CaH_2).

References

/1/ J. A. Lake, R. G. Bennett, J. F. Kotek
Next Generation of Nuclear Power
Scientific American, January (2002), 74

/2/ Y. Oka
Physics of Supercritical-Pressure Light Water Cooled Reactors
Frederic Joliot Summer School (FJSS' 98), CEA, Cadarache, Aug. 17-26, France (1998).

/3/ Y. Oka
Toward 'Nuclear Renaissance', a Perspective of Nuclear Energy and its Research
International Conference "Enrico Fermi and Nuclear Energy", October 15-16, Pisa, Italy (2001).

/4/ Y. Oka
Review of High Temperature Water and Steam Cooled Reactor Concepts
The First International Symposium on Supercritical Water-cooled Reactors, Design and Technology [SCR-2000], November 6 - 9, Tokyo, Japan (2000).

/5/ T. Jevremovic, Y. Oka
Nuclear Design of Fast Reactors Cooled by Supercritical Water
GLOBAL 95, Sep. 11-14, Versailles, France (1995), pp. 1300-1307.

/6/ Y. Oka and S. Koshizuka
Design Concept of Once-Through Cycle Supercritical-Pressure Light Water Cooled Reactors
The First International Symposium on Supercritical Water-cooled Reactors, Design and Technology [SCR-2000], November 6 - 9, Tokyo, Japan (2000).

/7/ K. Dobashi, et al.
Conceptual Design of a High Temperature Power Reactor Cooled and Moderated by Supercritical Light Water
6th Int. Conf. on Nuclear Engineering (ICONE-6), San Diego, USA (1998).

/8/ Y. Oka and S. Koshizuka
Supercritical-pressure Once-through Cycle Light Water Cooled Reactor Concept
Journal of Nuclear Science and Technology, Vol. 38, (2001), pp. 1081-1089.

/9/ Y. Oka et al.
Systems Design of Direct-Cycle Supercritical-Water-Cooled Fast Reactors
Nuclear Technology, Vol. 109, (1995), pp. 1-10.

/10/ T. Jevremovic, Y. Oka, S. Koshizuka
Design of an Indirect–Cycle Fast Breeder Reactor Cooled by Supercritical Steam
Nucl. Eng. and Design, 144, (1993), p. 337.

/11/ R. B. Duffey, J. Hopwood, I. Love
The new ACR: optimizing the CANDU design
Proc. of 11th Int. Conf. on Nuclear Engineering (ICONE-11), Tokyo, Japan (2003), 36221.

/12/ H. Kang, Y. Bae
Conceptual Design of a Supercritical Water-Cooled Reactor with an Internal Recirculating Flow
Proc. of GENES4/ANP2003, Sep. 15-19, Kyoto, Japan (2003), Paper 1023.

/13/ G. Heusener, U. Müller, T. Schulenberg, D. Squarer
A European development program for a high performance light water reactor (HPLWR)
The First International Symposium on Supercritical Water-cooled Reactors, Design and Technology [SCR-2000], November 6 - 9, Tokyo, Japan (2000).

/14/ Y. Oka et al.
Supercritical-pressure Light Water Cooled Fast Reactors, a competitive way of FR over LWR
Proc. of 8th Int. Conf. on Nuclear Engineering (ICONE-8), Baltimore, USA (2000), 8216.

/15/ B. A. Gabaraev et al.
The Three-Target Channel-Type Uranium-Water Fast Reactor with Direct Flow of Supercritical Water to Solve the Problems of Weapon-Plutonium and Power Generation at High Efficiency
Proc. of 11th Int. Conf. on Nuclear Engineering (ICONE-11), Tokyo, Japan (2003), 36021.

/16/ B. Culbreth, E. Bakker, J. Viggato
The Fission Properties of Curium Separated from Spent Nuclear Fuel
Report of the UNLV, Department of Mechanical Engineering, USA April (2002).

/17/ A. Vasile, G. Vambenèpe, J. C. Lefèvre, K. Hesketh, W. Maschek, Ch. De Raedt, D. Haas
The CAPRA-CADRA Program
8th Int. Conf. on Nuclear Engineering (ICONE-8), Baltimore, USA (2000).

/18/ A. S. Gerasimov, G. V. Kiselev, L. A. Myrtsymova, T. S. Zaritskaya
Cyclic Mode of Neptunium, Americium and Curium Transmutation in Heavy-Water Reactor
11th Int. Conf. on Nuclear Engineering (ICONE-11), Tokyo, Japan (2003).

/19/ Y. Ishiwatari, Y. Oka, S. Koshizuka
Breeding Ratio Analysis of a Fast Reactor Cooled by Supercritical Light Water
Journal of Nuclear Science and Technology, Vol. 38, No. 9, September (2001), p. 703-710.

/20/ T. Iwasaki, T. Sugawara
A Study of Transmutation of Long-Lived Nuclides in Fast Reactor Using New Hydride Material with High Dissociation Temperature
GLOBAL 2001, Paris, France (2001).

/21/ D. T. Aase et al.
Economic Evaluation of a 300MWe Fast Supercritical Pressure Power Reactor
Engineering Development Reactor and Fuels Laboratory Hanford Laboratories, contract of the General Electric Company HW-78953, UC-80 Reactor Technology (TID-4500, 27th Ed), December 9 (1963).

/22/ Keyfitz et al.
1000 MWe supercritical pressure nuclear power plant design study
Westinghouse Electric Corporation, WCAP 2240, (1964).

/23/ U.S. Department of Energy, Office of Fossil Energy, DOE/FE-0400,
Market-Based Advanced Coal Power Systems, Final Report
Washington, DC, USA (1999).

/24/ W. Wagner, A. Kruse
Properties of Water and Steam, The Industrial Standard IAPWS-IF97 for the Thermodynamic Properties and Supplementary Equations for Other Properties
Springer-Verlag Berlin Heidelberg, Germany (1998).

/25/ V. A. Kurganov, A.G. Kaptilnyi
Flow Structure and turbulent transport of a supercritical pressure fluid in a vertical heated tube under the conditions of mixed convection. Experimental data
Int. J. Heat Mass Transfer, Vol.36, (1993), pp. 3383-3392.

/26/ B. S. Shiralkar, P. Griffith
Deterioration in heat transfer to fluids at supercritical pressure and high heat fluxes
Journal of heat transfer, February, (1969), pp. 27-36.

/27/ S. Koshizuka, N. Takano, Y. Oka
Numerical analysis of deterioration phenomena in heat transfer to supercritical water
Int. J. Heat Mass Transfer, Vol.38, No.16, (1995), pp. 3077-3084.

/28/ I. L. Pioro, H. F. Khartabil, R. B. Duffey
Heat Transfer at Supercritical Pressures (Survey)
Proc. of 11th Int. Conf. on Nuclear Engineering (ICONE-11), Tokyo, Japan (2003), 36454.

/29/ J. H. Lee, Y. Oka, S. Koshizuka
Safety system consideration of a Supercritical Water Cooled Fast Reactor with simplified PSA
Reliability Engineering and System Safety, (1999).

/30/ Y. Oka, S. Koshizuka, J.H. Lee, Y. Okano, K. Kitoh, T. Nakatsuka, K. Dobashi, and T. Mukohara
Safety of a Light Water Cooled Reactor Operating at Supercritical Pressure
5th Int. Conf. on Nuclear Engineering (ICONE-5), Nice, France (1997).

/31/ Y. Okano, S. Koshizuka, Y. Oka
Safety Analysis of a Supercritical Pressure Light Water Cooled and Moderated Reactor with Double Tube Water Rods
Annals of Nuclear Energy, Vol. 24, No. 17. Elsevier Science Ltd. (1997), p. 1447-1456.

/32/ Y. Okano, S. Koshizuka, Y. Oka
Flow and Pressure-Induced Transient Analysis of the Supercritical-Pressure, light-water-cooled and moderated Reactor
6th Int. Conf. on Nuclear Engineering (ICONE-6), San Diego, USA (1998).

/33/ K. Kitoh, S. Koshizuka, Y. Oka
Control-rod, Pressure and Flow-Induced Accident and Transient Analyses of a Direct-Cycle, Supercritical-Pressure, Light-Water-Cooled Fast Breeder Reactor
7th Int. Conf. on Nuclear Engineering (ICONE-7), Tokyo, Japan (1999).

/34/ Y. Okano, S. Koshizuka, K. Kitoh, Y. Oka
Flow-Induced Accident and Transient Analyses of a Direct-Cycle, Light-Water-Cooled, Fast Breeder Reactor Operating at Supercritical Pressure
Journal of Nuclear Science and Technology, Vol. 33, No. 4, April (1996), pp. 307-315.

/35/ K. Kitoh, S. Koshizuka, Y. Oka
Pressure and Flow-Induced Accident and Transient Analyses of a Direct-Cycle, Supercritical-Pressure, Light-Water-Cooled Fast Reactor
Nuclear Technology, Vol. 123, (1998), pp. 233-244.

/36/ K. Kitoh, S. Koshizuka, Y. Oka
Refinement of Transient Criteria and Safety Analysis for a High-Temperature Reactor Cooled by Supercritical Water
Nuclear Technology, Vol. 135, (2001), pp. 252-264.

/37/ J. H. Lee, S. Koshizuka, Y. Oka
Development of a LOCA analysis code for the supercritical-pressure Light Water Cooled Reactors
Annals of Nuclear Energy, Vol. 25, No. 16, (1998), pp. 1341-1361.

/38/ T. Mukohara, et al.
Core Design of a High-Temperature Fast Reactor Cooled by Supercritical Light Water
Annals of Nuclear Energy 26, (1999), pp. 123-1436.

/39/ T. Jevremovic, Y. Oka, S. Koshizuka
Core Design of a Direct–Cycle Supercritical-Water-Cooled Fast Breeder Reactor
Nuclear Technology, Vol. 108, October (1994).

/40/ S. Tanaka, et al.
Core Design of Supercritical-Pressure Light Water Reactor
4th Int. Conf. on Nuclear Engineering (ICONE-4), March 10-15, New Orleans, USA (1996).

/41/ T. Jevremovic et al.
Effect of Zirconium-Hydride Layers on reducing coolant void reactivity of steam cooled fast breeder reactors
Journal of Nuclear Science and Technology, 30 (6), June (1993), pp. 497-504.

/42/ Y. Oka, T. Jevremovic
Negative coolant void reactivity in large fast breeder reactors with hydrogenous moderator layer
Annals of Nuclear Energy 23, (1996), p. 1105.

/43/ Magnus Mori, V. Sinitsa, A. Rineiski
Uncertainties in Void Effect Estimations for a SuperCritical Water Fast Reactor with Transmutation Capabilities
Proceedings of the Annual Meeting on Nuclear Technology [JK2003], May 20-22, Berlin, Germany, Inforum GmbH (2003), p. 29.

/44/ R. E. Alcouffe, R. S. Baker, F. W. Brinkley, D. R. Marr, R. D. O'Dell, and W. F. Walters
DANTSYS: A Diffusion Accelerated Neutral Particle Transport Code System
LA-12969-M, Los Alamos (NM), USA, June (1995).

/45/ C. Reiche, H. Barz, B. Kunzmann, E. Seifert, H. Wand
Reactor-Code-System RHEIN für ESER Computer
Akademie der Wissenschaften der DDR, ZfK ISSN 0138-2950, April (1989).

/46/ J. F. Briesmeister
MCNPTM – A General Monte-Carlo N-Particle Transport Code, Version 4C
LA-13709-M, March (2000).

/47/ R. E. MacFarlane, D. W. Muir
The NJOY Nuclear Data Processing System, Version 91
LA-12740-M, Los Alamos National Laboratory (1994).

/48/ Sa. Kondo, K. Morita, Y. Tobita, N. Shirakawa
SIMMER-III : An Advanced Computer Program for LMFBR Severe Accident Analysis
ANP'92, Tokyo, Japan (1992).

/49/ Y. Tobita, Sa. Kondo, H. Yamano, S. Fujita, K. Morita, W. Maschek, J. Louvet, P. Coste, S. Pigny
Current Status and Application of SIMMER-III, an Advanced Computer Program for LMFR Safety Analysis
NTHAS2: Second Japan-Korea Symposium on Nuclear Thermal Hydraulics and Safety, October 15-18, Fukuoka, Japan (2000).

/50/ K. O. Ott and R. J. Neuhold
Nuclear Reactor Dynamics
ANS, La Grange Park, USA (1986).

/51/ G. Buckel, E. Hesselschwerdt, E. Kiefhaber, S. Kleinheins, W. Maschek
A New SIMMER-III Version with improved Neutronics Solution Algorithms
FZKA 6290, Forschungszentrum Karlsruhe, Germany (1999).

/52/ K. Morita, E.A. Fischer, K. Thurnay
Thermodynamic Properties and Equations of State for Fast Reactor Safety Analysis, Part II: Properties of Fast Reactor Materials
Nuclear Engineering and Design, 183 (1998).

/53/ M. Mori, A. Rineiski, V. Sinitsa, W. Maschek
Monte-Carlo and Deterministic Models for Void Effect Calculations in the SuperCritical Water Fast Reactor
Proc. of GENES4/ANP2003, September 15-19, Kyoto, Japan, CD-ROM, Paper 1135 (2003).

/54/ M. Mori, W. Maschek, E. Laurien, K. Morita
Monte-Carlo/Simmer-III Reactivity Coefficients Calculations for the SuperCritical Water Fast Reactor
Proceedings of the ANS/ENS Topical Meeting GLOBAL 2003, November 16-20, New Orleans (LA), USA, CD-ROM S.1754-62 (2003).

/55/ T. Jevremovic, Y. Oka, S. Koshizuka
Conceptual Design of an Indirect–Cycle Supercritical-Steam-Cooled Fast Breeder Reactor with Negative Coolant Void Reactivity Characteristics
Annals of Nuclear Energy, Vol. 20, No. 5, (1993), pp. 305-313.

/56/ G. I. Bell, S. Glasstone
Nuclear Reactor Theory
Robert E. Krieger Publishing Company, Huntington, NY USA (1979).

/57/ N. E. Todreas, M. S. Kazimi
Nuclear Systems I, Thermal Hydraulic Fundamentals
Taylor & Francis, USA (1993).

/58/ N. E. Todreas, M. S. Kazimi
Nuclear Systems II, Elements of Thermal Hydraulic Design
Hemisphere Publishing Corporation, USA (1990).

/59/ K. Wark, Jr.
Advanced Thermodynamics for Engineers
McGraw-Hill, Inc., USA, (1995).

/60/ O. Antoni, P. Dumaz
Preliminary Calculation of a Supercritical Light Water Reactor Concept using the CATHARE Code
ICAPP'03, May 4-7, Cordoba, Spain (2003).

/61/ K. Kataoka et al.
Progress of Development Project of Supercritical-water Cooled Power Reactor, 2003
ICAPP'03, May 4-7, Cordoba, Spain (2003).

/62/ V. H. Sánchez-Espinoza, W. Hering
Investigations of the Appropriateness of RELAP5/MOD3 for the Safety Evaluation of an Innovative Reactor Operating at Thermodynamically Supercritical Conditions
Wissenschaftliche Berichte FZKA 6749; Forschungszentrum Karlsruhe, March (2003).

/63/ A. A. Bishop, R. O. Sandberg, L. S. Tong
Forced Convection Heat Transfer to Water at near Critical Temperatures and Supercritical Pressures
WCAP-2056-P, Part-III-B, February (1964).

/64/ X. Cheng, T. Schulenberg
Heat Transfer at Supercritical Pressures – Literature Review and Application to an HPLWR
Wissenschaftliche Berichte FZKA 6609; Forschungszentrum Karlsruhe, May (2001).

/65/ L. J. Siefken, C. B. Davis, E. A. Harvego
Modeling of Supercritical Pressurized Water Reactors with SCDAP/RELAP5-3D
INEEL, 01-GA50038-11, Idaho Falls, ID USA (2003).

/66/ A. E. Waltar, A. B. Reynolds
Fast Breeder Reactors
Pergamon Press, New York, USA (1981).

/67/ A. M. Weinberg, E. P. Wigner
The Physical Theory of Neutron Chain Reactors
The University of Chicago Press, Chicago (IL), USA (1958).

/68/ E. E. Lewis, W. F. Miller, Jr.
Computational Methods of Neutron Transport
John Wiley & Sons, New York, NY USA (1984).

/69/ R. A. Johnson, G. K. Battacharyya
Statistics - principles and methods
2nd ed. John Wiley & Sons, USA (1992).

/70/ T. J. Urbatsch, R. A. Forster, R. E. Prael, R. J. Beckman
Estimation and Interpretation of Keff Confidence Intervals in MCNP
Nuclear Technology, Vol. 111, (1995), pp. 169-182.

/71/ F. B. Brown, R. D. Mosteller
MCNP5 Workshop
LA-UR-04-2647, Physor-2004, Chicago, IL USA (2004).

/72/ W. R. Bohl, L. B. Luck
SIMMER-II: A Computer Program for LMFBR Disrupted Core Analyses
LA-11415-MS, USA (1990).

/73/ The MCNPX Team
MCNPX™ User's Manual, Version 2.4.0
LA-CP-02-408, Los Alamos, NM USA (2002).

/74/ M. Abramowitz, I. A. Stegun
Handbook of Mathematical Functions with Formulas, Graphs, and Mathematical Tables
Dover, NY USA (1972).

/75/ T. M. MacRobert, I. N. Sneddon
Spherical Harmonics: An Elementary Treatise on Harmonic Functions, with Applications
3rd ed. rev. Oxford, England: Pergamon Press, (1967).

/76/ R. A. Knief
Nuclear Energy Technology: Theory and Practice of Commercial Nuclear Power
McGraw-Hill, New York, NY USA (1981).

/77/ S. Glasstone, A. Sesonske
Nuclear Reactor Engineering: reactor design basics
4th Ed. Vol. 2, Chapman & Hall, New York, USA (1994).

/78/ JNC TN9400 2000-105
Phase 2 Code Assessment of SIMMER-III, a Computer Program for LMFR Core Disruptive Accident Analysis
Japan Nuclear Cycle Development Institute, O-Arai, Japan, September (2000).

/79/ NEA/NSC/DOC(2003)16
Benchmark on Deterministic Transport Calculations Without Spatial Homogenization: A 2-D/3-D MOX Fuel Assembly Benchmark
NEA/OECD, ISBN 92-64-021139-6, Paris, France (2003).

/80/ S. B. Turner, R. E. Pevey, R. S. Baker, K. D. Lewis
Use of PARTISN 2.64 on the Y-12 National Security Complex SGI High-Performance Computer (Manhattan)
ANS Transactions, TANSAO 87 1-586, Vol. 87, ISSN 0003-018X, Washington, DC, USA (2002).

/81/ A. Languille et al.
Capra core studies - the oxide reference option
Proceedings of the Int. Conf. on Evaluation of Emerging Nuclear Fuel Cycle Systems (GLOBAL'95), Versailles, France (1995).

/82/ E. Kiefhaber et al.
The KFKINR-set of Group Constants; Nuclear Data basis and First Results of its Application

for the Recalculation of Fast Zero-Power Reactors
KFK-1572, Karlsruhe, Germany (1972).

/83/ P. F. Rose, C. L. Dunford
ENDF-102, Data Formats and Procedures for the Evaluated Nuclear Data File, ENDF-6
Brookhaven National Laboratory report BNL-NCS-44945, USA, July (1990).

/84/ S. Glasstone, A. Sesonske
Nuclear Reactor Engineering: reactor design basics
4th Ed. Vol. 1, Chapman & Hall, New York, USA (1994).

/85/ E. Kiefhaber
Influence of Delayed Neutron Spectra on Fast Reactor Criticality
Nuclear Science and Engineering: 111, 197-204 (1992).

/86/ Boron Carbide Powder
http://www.reade.com/Products/Carbides/boron_carbide.html

/87/ Properties of Boron Carbide
http://www.peakpeak.com/~jdavis/boron/B4C.html

/88/ “The Boron Report”; Eagle-Pitcher Industries, Inc. Boron Department.
http://www.tech.epcorp.com/Boron/Reactor%20Chemicals/Product%20data%20sheets/Product%20Data%20Sheets%20pdf/EP-SSGC-NAPB.pdf

/89/ W. Maschek, A. Rineiski, K. Morita, M. Flad
Inherent and Passive Safety Measures in Accelerator Driven Systems: A Safety Strategy for ADS
Global 2001, Paris, September (2001).

/90/ G. Majert, W. Renz, R. G. Barnes
The mechanism of hydrogen diffusion in zirconium dihydrides
J. Phys. Condensed Matter 6, 2935 (1994).

/91/ T. Lefvert
Ringhals 1 stability benchmark
NEA/NSC/DOC(96)22, Nuclear Science Committee, Paris, France, November (1996).

/92/ M. Mori
Benchmarking and Qualification of RETRAN-03 for BWR Stability Analysis by Comparison with Frequency-Domain Stability Analysis Code
Nuclear Technology, Vol. 121, (1998), pp. 260-273.

/93/ M. Mori, F. D’Auria, W. J. M. de Kruijif, T. H. J. J. van der Hagen
Determination of BWR Stability Characteristics from Numerically Obtained System Responses
3rd International Conference on “Nuclear Option in Countries with small and medium Electricity Grids”, Dubrovnik, Croatia, June (2000).

/94/ F. D’Auria, W. Ambrosini, T. Anegawa, J. Blomstrand, J. In de Betou, S. Langenbuch, T. Lefvert, K. Valtonen
State Of the Art Report on Boiling Water Reactor stability
NEA, Committee on the Safety of Nuclear Installations, Paris, France, September (1996).

/95/ D. I. Poston, H. R. Trellue
User’s Manual, Version 2.0 for MONTEBURNS, Version 1.0
LA-UR-99-4999, Los Alamos National Laboratory, Los Alamos, NM USA (1999).

/96/ J. Cetnar, J. Wallenius, W. Gudowski
MCB: a Continuous Energy Monte-Carlo Burnup Simulation Code
Fifth OECD/NEA Information Exchange Meeting on Actinide and Fission Product Partitioning and Transmutation; SCK/CEN, Mol, Belgium, 25-27 November (1998).

Appendix A

Description of the nuclear data libraries used in this work

ENDF-6.7

The ENDF/B data library, released by the National Nuclear Data Center (NNDC) at Brookhaven National Laboratory, was recently updated to ENDF/B-VI, Release 7 (August 2000). As the other libraries mentioned above, the original evaluated data include cross sections represented in the form of a combination of resonance parameters, average resonance parameters (in the unresolved resonance energy region), and tabulated energy dependent cross sections, nominally at 0 Kelvin temperature. For use in applications, this ENDF/B-VI, Release 7 contains evaluations for 324 materials (isotopes or naturally occurring elemental mixtures of isotopes). The majority of these evaluations are complete, in the sense that they include all cross sections over the energy range 1.E-5 eV to at least 20 MeV.

JEF-2.2:

JEF–2.2 (Joint Evaluated File) is the standard nuclear data library for Europe. The current version of this general-purpose library was released in January 1992. The library contains evaluations of neutron reaction data for 313 elements or isotopes from 1-H-1 to 99-Es-253 in the neutron energy range from 1.E-5 eV to 20 MeV, in ENDF-6 format. A 172-group cross-section file based mainly on this library was used for the previous stage of the work while evaluating data-related uncertainties of the void effect (by comparing 172-group results and 26-group results based on another cross-section basis).

JENDL-3.2

JENDL-3.2 (Japanese Evaluated Nuclear Data Library) was developed by the nuclear data center of Japanese Atomic Energy Research Institute (JAERI) and Japanese Nuclear Data Committee (JNDC). It was released in June 1994 and developed to provide a Japanese standard library for fast breeder reactors, thermal reactors, fusion neutronics and shielding calculations. The library contains evaluations of neutron reaction data for 340 isotopes in the neutron energy range from 1.E-5 eV to 20 MeV, in ENDF-6 format. This library is also a general-purpose cross-section data library.

Appendix B

Analysis of core performance

In the SCFR, there are blankets of two types: (1) internal/external radial blankets and (2) axial blankets. The axial (upper and lower) blankets are the upper- and lowermost parts of the seed pins. Compared to the conventional LMFRs, their contribution (of the upper and lower blankets) to the reactor fuel balance is significantly reduced, as their relative (with respect to the total reactor) volume is small compared to the axial blankets of LMFRs. Therefore, one may consider the elimination of the lower blanket, in particular if it may help to improve the safety behavior of the SCFR.

To confirm the small impact of the lower blanket elimination on variation of the isotopic inventory of the reactor during its operation at nominal power level, burn-up simulations were performed. A 2D RZ deterministic model was employed, similar to that one applied earlier for deterministic calculations of the void effect (see Chapter 4.1). Due to the approximate treatment of geometry and heterogeneity effects and a relatively small number of energy groups, this modeling cannot be considered as a reference (with respect to burn-up simulation) and should eventually be compared with more detailed Monte-Carlo analyses. However, the relatively good agreement, which was demonstrated in the past, between the 2D model and the 3D Monte-Carlo model with respect to the void effect calculations shows that the main components of the neutron balance can be estimated reasonably well by employing the 2D option. Therefore, this model was considered sufficiently accurate to calculate the effect of the lower blanket elimination.

Two models were prepared for burn-up simulations: one including, the other excluding the lower blanket. In this second option, the smeared nuclear densities below the seed were taken similar to those of the lower axial reflector. Above the lower seed boundary, the neutronics models corresponded.

We compared the number of plutonium nuclei (computed on the total reactor volume) at different burn-up levels up to 360 effective power days and assuming no variation of nuclear density of non-fuel materials and no effect of control rod movement on the burn-up (the control rods are ignored in this model).

In Fig. A and Fig. B the relative content of ^{239}Pu and ^{241}Pu (% of heavy atoms, including pairs of fission products) during the simulation is shown. The corresponding curves for ^{238}Pu, ^{240}Pu and ^{242}Pu are not shown, as their variation and influence on the core criticality and conversion ratio is quite small.

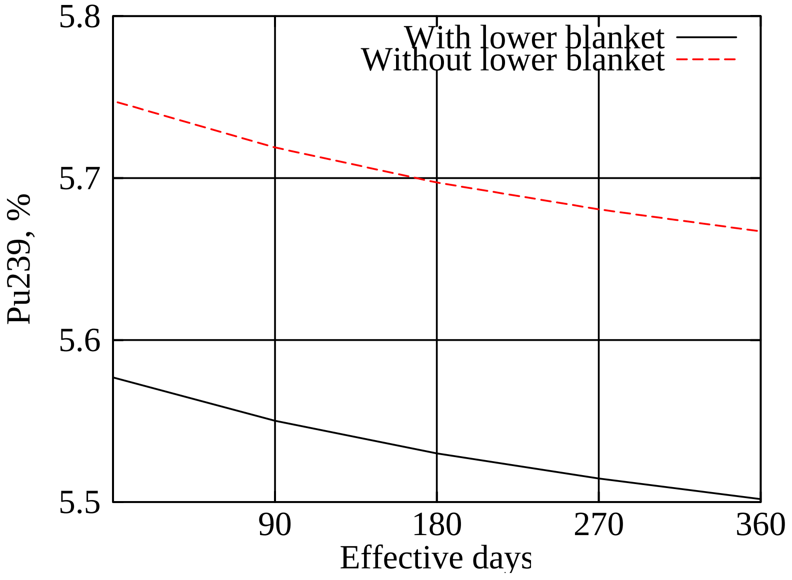

Fig. A: Variation of ^{239}Pu content in the SCFR (% heavy atoms), operation nominal power

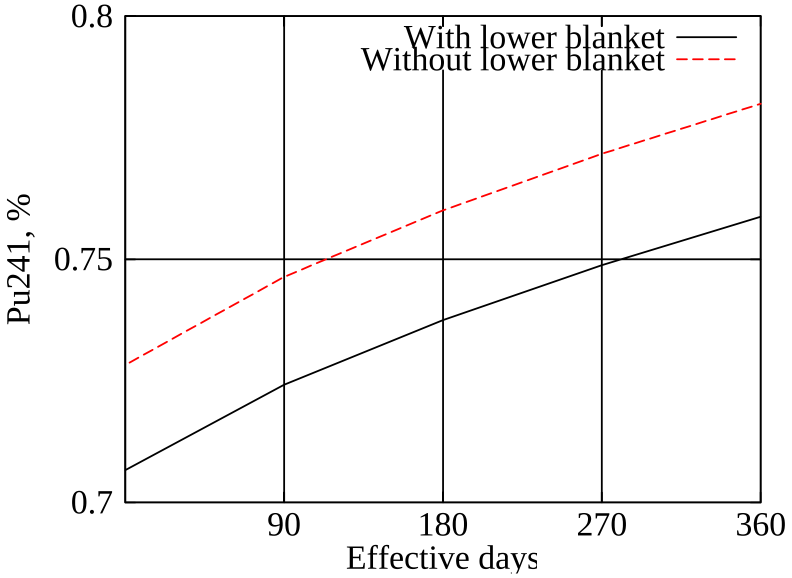

Fig. B: Variation of ^{241}Pu content in the SCFR (% heavy atoms), operation at nominal power

For the 'removed lower blanket' option, the relative amount of plutonium is higher as the reactor uranium inventory is smaller. During reactor operation, the number of ^{239}Pu nuclei is decreasing, while the number of ^{241}Pu nuclei is increasing. Taking into account a higher (by about 50%) "efficiency" of ^{241}Pu nuclei to maintain the neutron balance, the overall conversion ratio (CR) is close to 1 for this reactor (in agreement with the valued reported in Table 2.1). A more accurate CR value could be obtained by coupled Monte-Carlo and burn-up codes. For this study, however, we are interested in the effect of the lower blanket removal on the CR (rather than in the absolute CR value) and Fig. A and Fig. B show that this effect is almost negligible.

In Tab. A and Tab. B the fuel compositions (at the beginning of cycle (BOC) and after 360 days of operation) of the Seed, Blanket, and whole Reactor (numbers of heavy atoms in %, including pairs of fission products) are given for the 2 design options considered: with and without lower blanket below the seed (only data for uranium and plutonium isotopes are presented excluding data for the other produced heavy isotopes and fission products). The results are in qualitative agreement with previous studies /19/.

	*With lower blanket, **BOC***			*With lower blanket, after **360 days***		
Isotope	**Seed**	**Blanket**	**Reactor**	**Seed**	**Blanket**	**Reactor**
^{235}U	**0.07698**	**0.10128**	**0.17826**	**0.06755**	**0.07766**	**0.14521**
^{238}U	**38.4138**	**50.5369**	**88.9506**	**37.9358**	**50.2043**	**88.14**
^{238}Pu	**0.04348**	**0**	**0.04348**	**0.04026**	**0.0001**	**0.04037**
^{239}Pu	**5.57689**	**0**	**5.57689**	**5.27697**	**0.22482**	**5.5018**
^{240}Pu	**4.10929**	**0**	**4.10929**	**4.06737**	**0.01601**	**4.08338**
^{241}Pu	**0.70662**	**0**	**0.70662**	**0.75073**	**0.00799**	**0.75872**
^{242}Pu	**0.43485**	**0**	**0.43485**	**0.43098**	**0.00049**	**0.43147**
TOTAL	**49.3619**	**50.6381**	**100**	**49.3619**	**50.6381**	**100**

Tab. A: : Isotopic composition (% of heavy atoms in the reactor) at the beginning of cycle (BOC) and after 360 days of operation for the with lower blanket options

	*Without lower blanket, **BOC***			*Without lower blanket, after **360 days***		
Isotope	**Seed**	**Blanket**	**Reactor**	**Seed**	**Blanket**	**Reactor**
^{235}U	**0.07934**	**0.09825**	**0.17759**	**0.06961**	**0.07418**	**0.14379**
^{238}U	**39.5899**	**49.0285**	**88.6184**	**39.0971**	**48.6888**	**87.7859**
^{238}Pu	**0.04482**	**0**	**0.04482**	**0.0415**	**0.00011**	**0.0416**
^{239}Pu	**5.74765**	**0**	**5.74765**	**5.43839**	**0.22869**	**5.66708**
^{240}Pu	**4.23511**	**0**	**4.23511**	**4.1919**	**0.01651**	**4.20841**
^{241}Pu	**0.72826**	**0**	**0.72826**	**0.7737**	**0.00827**	**0.78196**
^{242}Pu	**0.44816**	**0**	**0.44816**	**0.44419**	**0.0005**	**0.44469**
TOTAL	**50.8733**	**49.1267**	**100**	**50.8733**	**49.1267**	**100**

Tab. B: Isotopic composition (% of heavy atoms in the reactor) at the beginning of cycle (BOC) and after 360 days of operation for the without lower blanket options

In /19/, the breeding ratio is defined as the fissile plutonium surviving ratio (FPSR): the ratio of amounts of ^{239}Pu and ^{241}Pu at the EOC and BOC conditions. For a cycle length of 390 days, and a fuel volume fraction of 49.8%, /19/ reports that the FPSR is 0.981. In this study (for a similar volume fraction of about 49.7%), for the considered design options (with/without lower blanket) one may obtain from Tab. A and Tab. B the FPSR values of 0.9963/0.9959 (after 360 days). If, however, a higher " fission efficiency" of ^{241}Pu were taken into account, e.g. by assigning a weight of 1.5 to ^{241}Pu (which has, if compared to ^{239}Pu, a higher fission, but similar capture cross-sections), the FPSR value would be of 1.0005/1.0000 for the with/without lower blanket options. The observed deviations (0.981 of /19/ vs. 0.9963 of this study) may relate to different plutonium compositions (in /19/ ^{238}Pu was not taken into account at the BOC), design details, nuclear data, and modeling options.